Brigham Young University
BYU ScholarsArchive

All Theses and Dissertations

2011-03-09

Surface Modification, Fabrication, and Characterization of Silicon, Polymer, and Nanotube Composite Materials

Lei Pei
Brigham Young University - Provo

Follow this and additional works at: https://scholarsarchive.byu.edu/etd

Part of the Biochemistry Commons, and the Chemistry Commons

BYU ScholarsArchive Citation

Pei, Lei, "Surface Modification, Fabrication, and Characterization of Silicon, Polymer, and Nanotube Composite Materials" (2011). *All Theses and Dissertations*. 2925.
https://scholarsarchive.byu.edu/etd/2925

This Dissertation is brought to you for free and open access by BYU ScholarsArchive. It has been accepted for inclusion in All Theses and Dissertations by an authorized administrator of BYU ScholarsArchive. For more information, please contact scholarsarchive@byu.edu, ellen_amatangelo@byu.edu.

Surface Modification, Fabrication, and Characterization of Silicon, Polymer, and Nanotube Composite Materials

Lei Pei

A dissertation submitted to the faculty of
Brigham Young University
in partial fulfillment of the requirements for the degree of

Doctor of Philosophy

Matthew R. Linford, chair
Milton L. Lee
Steven R. Goates
Matthew C. Asplund
Robert C. Davis

Department of Chemistry and Biochemistry

Brigham Young University

April 2011

Copyright © 2011 Lei Pei

All Rights Reserved

ABSTRACT

Surface Modification, Fabrication, and Characterization of Silicon, Polymer, and Nanotube Composite Materials

Lei Pei
Department of Chemistry and Biochemistry, BYU

Doctor of Philosophy

In my research, I have performed many characterization and fabrication experiments that are based on tools of analytical chemistry, materials chemistry, and surface science. My research projects are as follows. (1) Fabrication of transparent polymer templates for nanostructured amorphous silicon photovoltaics was done using low-cost nanoimprint lithography of polydimethylsiloxane. This approach provides a test bed for absorption studies in nanostructured film geometries and should result in improved light capturing designs in thin-film solar cells. Nanopatterned polymer films were characterized by scanning electron microscopy and optical measurements. (2) A straightforward method for fabricating freely suspended, thin, carbon nanotube (CNT) membranes infiltrated with polymers was developed. This process is a new approach for making thin, reinforced, smooth films or membranes with high concentrations of CNTs, which may lead to higher performance materials. Characterization of the film and membrane was performed via scanning electron microscopy and atomic force microscopy. (3) Laser activation-modification of semiconductor surfaces (LAMSS) was carried out on silicon with a series of 1-alkenes. A key finding from this study is that the degree of surface functionalization in a LAMSS spot appears to decrease radially from the center of the spot. These laser spots were studied by time of flight secondary ion mass spectrometry (ToF-SIMS), and the resulting spectra were analyzed using a series of chemometrics methods. (4) A large ToF-SIMS data set from multiple coal samples spanning a wide range of coal properties was subjected to a chemometrics analysis. This analysis separates the spectra into clusters that correspond to measurements from classical combustion analyses. Thus ToF-SIMS appears to be a promising technique for analysis of this important fuel. (5) Several experiments on carbon nanotube processing were performed in my research, including carbon nanotube sheet formation, carbon nanotube purification, carbon nanotube dispersion, and carbon nanotube functionalization. X-ray photoelectron spectroscopy was a key characterization tool for many of these experiments.

Keywords: surface modification, fabrication, characterization, carbon nanotube, silicon, polymer composite

ACKNOWLEDGEMENTS

My dissertation and research were under the guidance of Dr. Linford, with the active involvement of my committee members, and with the support of my family. In particular, I would like to acknowledge the contributions of the following people:

I express my sincere gratitude to my advisor, Dr. Linford, who gave me valuable guidance, support, and encouragement for the successful completion of my dissertation and research work. I am very grateful to have had the opportunity to work under his supervision.

I also deeply appreciate Dr. Davis, who played a key advisory role throughout most of my research. With his suggestions and critical comments, the research work has moved forward well.

I wish to express my gratitude to my committee members, Dr. Lee, Dr. Goates, Dr. Asplund, Dr. Davis, and Dr. Linford for their kindness in helping me revise my dissertation.

I would also like to thank all members of the Linford and Davis/Vanfleet groups. I am very pleased to have been able to work with them on different research projects. I am also grateful to them for their friendship and help in my life while I have been at BYU.

Last but not least, I would like to give a very special thanks to Yang Liu, my wife, for supporting and encouraging me all these years.

TABLE OF CONTENTS

ABSTRACT ... ii

ACKNOWLEDGEMENTS ... iii

TABLE OF CONTENTS ... iv

LIST OF FIGURES ... xi

LIST OF ABBREVIATIONS ... xix

Chapter 1 Introduction ... 1

1.1 Materials Characterization Techniques ... 1

1.1.1 X-ray photoelectron spectroscopy (XPS) ... 1

1.1.2 Time-of-flight secondary ion mass spectrometry (ToF-SIMS) ... 8

1.1.3 Atomic force microscopy (AFM) ... 12

1.1.4 Scanning electron microscopy (SEM) ... 18

1.1.5 Transmission electron microscopy (TEM) ... 21

1.1.6 Ellipsometry ... 23

1.1.7 Water contact angle goniometry ... 25

1.1.8 Optical measurements ... 27

1.1.9 Electrical conductivity measurements ... 29

1.2 Materials Fabrication Techniques 31
1.2.1 Spin coating 31
1.2.2 Thermal evaporation 33
1.2.3 Electron-beam evaporation 33
1.2.4 Sputtering 33
1.2.5 Chemical vapor deposition (CVD) 34
1.2.6 Photolithography 36
1.2.7 Electron beam lithography (EBL) 38
1.2.8 Nanoimprint lithography (NIL) 38
1.2.9 Wet etching 39
1.2.10 Plasma etching 40
1.2.11 Silicon deep etching 40
1.3 Experimental materials 41
1.3.1 Carbon nanotubes 41
1.3.2 Silicon wafers 42
1.4 Chemometrics 43
1.4.1 Principal components analysis (PCA) 43

1.4.2 Cluster analysis 44

1.4.3 Partial least-squares (PLS) 45

1.4.4 Multivariate curve resolution (MCR) 45

1.5 Contents of This Dissertation 46

1.6 References 48

Chapter 2 Polymer Molded Templates for Nanostructured Amorphous Silicon Photovoltaics........ 59

2.1 Abstract 59

2.2 Introduction 59

2.3 Experimental 61

2.3.1 Electron-beam lithography 61

2.3.2 Silicon master etching 62

2.3.3 Anti-adhesion coating deposition 62

2.3.4 Nanoimprint patterning of the polymer 65

2.3.5 Photovoltaic material deposition 67

2.3.6 Optical measurement setup 69

2.4 Optical Results and Discussion 70

2.5 Conclusions 73

2.6 Acknowledgements 73

2.7 References 74

Chapter 3 Processing of Thin, Composite Carbon Nanotube-Polyimide Composite Membranes........ 78

3.1 Abstract 78

3.2 Introduction 78

3.3 Experimental Procedures........ 79

3.4 Results and Discussion........ 86

3.5 Conclusions 95

3.6 Acknowledgements 95

3.7 References and Notes 96

Chapter 4 Laser Activation-Modification of Semiconductor Surfaces (LAMSS) of 1-Alkenes on Silicon: A ToF-SIMS, Chemometrics, and AFM Analysis 99

4.1 Abstract 99

4.2 Introduction 100

4.3 Brief Overview of PCA and MCR 103

4.4 Experimental Section 104

4.4.1 Materials 104

4.4.2 Sample preparation 105

4.4.3 ToF-SIMS imaging 105

4.4.4 AXSIA-based MCR analysis of ToF-SIMS imaging 106

4.4.5 PCA analysis of AXSIA components 106

4.4.6 PCA, MCR, and cluster analysis 107

4.5 Results and Discussion 107

4.5.1 AXSIA analysis of ToF-SIMS images of LAMSS spots 107

4.5.2 Comparison of AXSIA MCR and PLS_Toolbox MCR analyses, and cluster analysis… 118

4.5.3 AFM 130

4.6 Conclusions 131

4.7 References 132

Chapter 5 Time-of-Flight Secondary Ion Mass Spectrometry of a Range of Coal Samples: A Chemometrics (PCA, Cluster, and PLS) Analysis 136

5.1 Abstract 136

5.2 Introduction 136

5.3 Experimental 144

5.3.1 Materials 144

5.3.2 ToF-SIMS 144

5.3.3 Sample Preparation 144

5.3.4 Chemometrics 144

5.4 Results and Discussion 147

5.5 Conclusions 171

5.6 Acknowledgment 171

5.7 References 172

Chapter 6 Carbon Nanotube Functionalization with Peroxides 177

6.1 Abstract 177

6.2 Introduction 177

6.3 Experimental 180

6.3.1 CNT purification 180

6.3.2 CNT functionalization 180

6.3.3 X-ray photoelectron spectroscopy (XPS) analysis 182

6.4 Results and Discussion 182

6.4.1 CNT bucky paper formation 182

6.4.2 CNT purification 184

6.4.3 CNT functionalization 186

6.5 Conclusions 187

6.6 References 191

Chapter 7 Future work 195

7.1 Polymer Molded Templates for Nanostructured Amorphous Silicon Photovoltaics 195

7.2 Processing of Thin, Composite Carbon Nanotube-Polyimide Composite Membranes 196

7.3 Time-of-Flight Secondary Ion Mass Spectrometry of a Range of Coal Samples: A Chemometrics (PCA, Cluster, and PLS) Analysis 197

7.4 Laser Activation-Modification of Semiconductor Surfaces (LAMSS) of 1-Alkenes on Silicon: A ToF-SIMS, Chemometrics, and AFM Analysis 197

Appendix 1 Angled Thermal Evaporation 199

Appendix 2 NIL Processes on PI, PEN, and PDMS 201

Appendix 3 Plasma Etching 206

LIST OF FIGURES

Figure 1.1. Schematic of the X-ray photoelectron spectroscopy (XPS) process, and a photograph of the Surface Science SSX-100 XPS system at BYU. 4

Figure 1.2. X-ray photoelectron spectra of 87% hydrolyzed poly(vinyl alcohol). The peaks in the XPS survey spectrum (a) are labeled by the element and orbital from which the emitted electrons originate. (The Auger signal at ca. 1000 eV from oxygen is not labeled.) The peaks in an XPS narrow scan of carbon (C1s) (b) are labeled according to the chemical states of each carbon atom in the sample. 7

Figure 1.3. Schematic drawing of time of flight secondary ion mass spectrometry (ToF-SIMS) and a photograph of the ION-TOF IV system at BYU. 10

Figure 1.4. Schematic of atomic force microscopy (AFM) and a photograph of the Veeco Dimension V system at BYU... 14

Figure 1.5. Schematic and specifications of a Veeco TESP silicon probe. 15

Figure 1.6. AFM measurements on a patterned polymer composite structure. 16

Figure 1.7. SEM images of a vertically aligned carbon nanotube forest and the FEI Philips XL30 S-FEG SEM system at BYU. 20

Figure 1.8. TEM images of carbon nanotubes and bundles. The TEM sample was prepared by placing droplets of a dispersion of carbon nanotubes in dichloroethane on a TEM grid and then vaporizing the solvent. 22

Figure 1.9. Schematic drawing of an ellipsometer and a photograph of the J. A. Woollam M-2000D spectroscopic ellipsometer system at BYU. 24

Figure 1.10. Schematic of the contact angle measurement and a photograph of the Ramé-Hart 100 water contact angle goniometer at BYU. A liquid droplet rests on a solid surface. The contact angle, θ, is the angle between the tangent line of the drop and the solid surface. 26

Figure 1.11. Schematic of optical measurements with an integrating sphere. 28

Figure 1.12. Schematic of the four point probe measurement for electrical sheet resistivity measurements. 30

Figure 1.13. Photograph of the Laurell spin coater at BYU. 32

Figure 1.14. Reaction of a perfluorosilane onto silicion dioxide by CVD. 35

Figure 1.15. (a) Mask design for photolithography, (b) schematic of the photolithography process, and (c) optical image of a photoresist layer patterned by photolithography. Images (a) and (c) were obtained as part of my research. 37

Figure 2.1. Schematic of the nanoimprint process: (a) silicon master coated with a perfluorosilane; (b) spin coating hard PDMS; (c) pouring soft PDMS on top of the hard PDMS; (d) placement of a glass slide; (e) curing the PDMS stack; and (f) releasing the silicon master. 63

Figure 2.2. SEM image of the patterned silicon wafer with nanopillar array. 64

Figure 2.3. (a) Optical and (b) SEM images of embossed nano-holes. 66

Figure 2.4. (a) SEM top view of an a-Si coated, patterned polymer template, and (b) cross-section view showing (starting from the top of a post and moving down) Pt (FIB deposited), a-Si (dark cap), and PDMS posts. 68

Figure 2.5. (a) transmittance spectra of patterned and planar areas, (b) reflectance spectra of patterned and planar areas, (c) absorbance spectra of patterned and planar areas, and (d) spectral irradiance of AM 1.5 and weighted absorbance of patterned and planar areas. 72

Figure 3.1. VACNT forest growth. A silicon substrate with Fe/Alumina layers was placed into a tube furnace and heated to 750 °C. Argon, hydrogen, and ethylene were used for MWNT growth. The ethylene flow was for 1 s for short VACNTs. 81

Figure 3.2. Rolling a MWNT forest into a thin film. A smooth glass tube was manually rolled over and pressed into the nitrile rubber sheet/aluminum foil/as-grown VACNT forest assembly.. 82

Figure 3.3. Polymer/CNT composite fabrication process. Polymer was spin coated onto a compressed CNT film. After baking in a furnace, a thin, smooth polymer/CNT composite film was produced. 84

Figure 3.4. Mesh frame attachment to and release with a composite film. For release, the assembly was dipped into a solution of HF. 85

Figure 3.5. SEM images of a VACNT forest. Top view (a, b) and tilted view (c, d) at different magnifications. The forest thickness was 2.4 µm. 88

Figure 3.6. SEM images of a compressed CNT film (600 nm thick). (a) Major area of the film surface showing a high CNT density, and (b) Example of a tearing defect in a film. 90

Figure 3.7. Cross-sectional SEM images of polymer CNT composite films at thicknesses of 400 nm (a, b) and 650 nm (c, d). A thin gold layer (5 nm) was sputtered on top of the sample surface to reduce charging. The samples were then frozen, cut into small pieces, and images were taken at sharp edges of the shards. 93

Figure 3.8. Photographs of released polymer-CNT composite membranes on mesh frames at thickness of 400 nm (a, b) and 650 nm (c, d). 94

Figure 4.1. AXSIA images and selected ToF-SIMS images from negative ion images of silicon surfaces modified by LAMSS with 1-decene (upper panel), and 1-tetradecene (lower panel). 110

Figure 4.2. AXSIA images and Si^+ ToF-SIMS images taken from positive ion ToF-SIMS images of silicon surfaces modified by LAMSS with 1-hexene, 1-octene, 1-decene, 1-dodecene, 1-tetradecene and 1-hexadecene, respectively (from up to down). 111

Figure 4.3. Negative-ion AXSIA component spectra of ToF-SIMS images of silicon surfaces modified with 1-hexene (left) and 1-hexadecene (right). 112

Figure 4.4. Positive-ion AXSIA component spectra of ToF-SIMS images of silicon surfaces modified with 1-octene (left) and 1-hexadecene (right). 113

Figure 4.5. PCA analysis of negative-ion AXSIA component spectra of ToF-SIMS images of silicon surfaces modified by LAMSS using 1-alkenes with 6, 8, 10, 12, 14 and 16 carbon atoms. 116

Figure 4.6. PCA analysis of positive ion AXSIA component spectra of ToF-SIMS images of silicon surfaces modified by LAMSS using 1-alkenes with 6, 8, 10, 12, 14 and 16 carbon atoms. 117

Figure 4.7. (a) Three AXSIA based single color MCR images and corresponding spectra, (b) an AFM image, and (c) the AXSIA C2 image on a different color scale. All data came from a single LAMSS spot made with 1-hexene. 119

Figure 4.8. PLS_Toolbox based MCR component spectra and loadings of the ToF-SIMS image of the spot shown in Figure 4.7. 120

Table 4.1. Total percent variance captured for a certain number of MCR components or principal components by PCA for the data shown in Figure 4.7a. 121

Figure 4.9. (a) Hotelling T^2 analysis/errors (95% confidence limit = 7.82) and (b) Q Residual analysis/errors (95% confidence limit = 105) of the PCA analysis of the data shown in Figure 4.7. (c) Q Residual analysis/errors of the MCR analysis shown in Figure 4.8 (95% confidence limit = 109). 124

Figure 4.10. (a) Image of the two-cluster analysis of the data shown in Figures 4.7 and 4.8, and average spectra corresponding to the (b) blue, and (c) red pixels. 126

Figure 4.11. (a) Image of the three-cluster analysis of the data shown in Figures 4.7 and 4.8, and average spectra corresponding to the (b) blue, (c) green, and (d) red pixels. 127

Figure 4.12. (a) Image of the four-cluster analysis of the data shown in Figures 4.7 and 4.8, and average spectra corresponding to the (b) dark blue, (c) light blue, (d) yellow, and (e) red pixels. 128

Figure 5.1. (a) Average of all of the ToF-SIMS spectra of the coal samples, and (b) superimposition of all of the ToF-SIMS spectra of the coal samples. 148

Figure 5.2. Plot of the scores of the coal spectra on the first and second principal components from a principal components analysis (PCA). 151

Figure 5.3. Average spectra of the spectra represented by the five points at the three vertices of the PC1 vs. PC2 plot. 152

Figure 5.4. (a) Rotated plot of PC1 vs. PC2 that shows the variation in PC1 along the vertical direction that corresponds to the variation in the loadings plot shown in (b). 154

Figure 5.5. (a) Plot of PC1 vs. PC2 that shows the variation in PC2 along the vertical direction that corresponds to the variation in the loadings plot shown in (b). 155

Figure 5.6. PC1 vs. PC2 score plots (left) that show the locations (numbering based on the vertical dashed line) on this PCA plot of the spectra in the seven clusters of the dendrogram from the cluster analysis (right). 159

Figure 5.7. (a) Cluster analysis and (b) PCA analysis of the properties of the coal samples, as measured by conventional methods. 164

Figure 5.8. (a) PC1 vs. PC2 plot showing the average heating value of the samples found in each of the seven clusters in the dendrogram, and (b) PC1 vs. PC2 plot showing the average percent Al_2O_3 composition of the samples found in each of the seven clusters in the dendrogram. The yellow arrows are guides to the eye. 165

Figure 5.9: PLS results for volatile matter and oxygen. (a) and (c) show the RMSECV plots that were used to determine the number of latent variables, and (b) and (d) show the CV predicted vs. measured properties. 168

Figure 6.1. (Left) photos of bucky paper, (a) free standing, thick bucky paper, and (b) transparent, thin bucky paper on filter paper; (middle) SEM images of thick bucky paper viewed horizontally, (c) with 500 mm scale bar, and (d) with 200 nm scale bar at high resolution; (right) SEM images of thick bucky paper viewed vertically, (e) with 200 µm scale bar, and (f) with 20 µm scale bar at high resolution. 183

Figure 6.2. XPS survey spectrum of purified single-walled carbon nanotubes produced by the HiPco process. 185

Figure 6.3. XPS survey and carbon 1s narrow scans for an s-SWNTs sample (a and b), and a control sample (c and d). For the control, all reaction conditions were identical to the sample run, with the exception that no peroxide was added. 188

Figure 6.4. XPS survey and carbon 1s narrow scans for a t-SWNTs sample (a and b), and a control sample (c and d). 189

Figure A1.1. Angled thermal evaporation setup for aluminum deposition on a patterned substrate. 200

Figure A2.1. (a) AFM image of a polyimide film patterned via NIL, (b) optical image of the NIL patterned polyimide film, and (c and d) SEM cross-sectional images of an NIL patterned polyimide film. The cross-sectional feature was milled by FIB and had a Pt coating. 203

Figure A2.2. SEM image of a PEN template embossed with nanostructures. Note that a small bump appears on the top edge of each nanohole (a), and undesired contamination appears on the surface (b). 204

LIST OF ABBREVIATIONS

AES	Auger electron spectroscopy
AFM	Atomic force microscopy
AM	Air mass
APCI	Atmospheric pressure chemical ionization
APTES	3-Aminopropyltriethoxysilane
a-Si:H	Hydrogenated amorphous silicon
AXSIA	Automated expert spectral image analysis
BE	Binding energy
BSE	Backscattered electrons
CLS	Classical least squares
CNT	Carbon nanotube
CNT-COOH	Carboxyl terminated carbon nanotube
CV	Cross-validation
CVD	Chemical vapor deposition
DI	Deionized
DMF	*N*,*N*-Dimethylformamide
E-beam	Electron beam
EBL	Electron beam lithography
EDX	Energy-dispersive X-ray spectroscopy
EELS	Electron energy loss spectroscopy

ESCA	Electron spectroscopy for chemical analysis
ESI-MS	Electrospray ionization mass spectrometry
EUV	Extreme UV lithography
FEG	Field emission gun
FIB	Focused ion beams
FTICR-MS	Fourier transform ion cyclotron resonance mass spectrometry
HF	Hydrofluoric acid
HiPco	High pressure CO disproportionation
h-PDMS	Hard PDMS
ICP	Inductively coupled plasma
ICP-RIE	Inductively coupled plasma reactive ion etching
iPLS	Interval PLS
IR	Infrared
KE	Kinetic energies
LAMSS	Laser activation-modification of semiconductor surfaces
LMIS	Liquid metal ion source
MCR	Multivariate curve resolution
MSE	Mean squared error
MWNT	Multi-walled nanotube
NGL	Next-generation lithography
NIL	Nanoimprint lithography
NMP	*N*-methyl-2-pyrrolidone

PC	Principal component
PCA	Principal components analysis
PDMS	Polydimethylsiloxane
PECVD	Plasma enhanced chemical vapor deposition
PEN	Polyethylene naphthalate
PI	Polyimide
PLS	Partial least-squares
PMMA	Poly(methylmethacrylate)
PTFE	Polytetrafluoroethylene
PV	Photovoltaic
PVA	Polyvinyl alcohol
PVD	Physical vapor deposition
RIE	Reactive ion etching
RMSECV	Root-mean-square error cross-validation
SAM	Self-assembled monolayer
SE	Secondary electrons
SEM	Scanning electron microscopy
SIMS	Secondary ion mass spectrometry
SPM	Scanning probe microscopy
s-SWNT	Succinic acid aryl peroxide functionalized single-walled nanotube
STM	Scanning tunneling microscopy
SWG	Sub-wavelength grating

SWNT	Single-walled nanotube
TEM	Transmission electron microscopy
THF	Tetrahydrofuran
TLD	Through-the-lens detector
ToF	Time of flight
ToF-SIMS	Time of flight secondary ion mass spectrometry
t-SWNT	Di-*tert*-amyl peroxide functionalized single-walled nanotube
UHR	Ultra high resolution
UHV	Ultra high vacuum
UPS	Ultraviolet photoelectron spectroscopy
UV	Ultraviolet
VACNT	Vertically aligned carbon nanotube
XPS	X-ray photoelectron spectroscopy

Chapter 1 Introduction

I have used many characterization and fabrication techniques in my research that are based on analytical chemistry, materials chemistry, and surface science. The fabrication processes employed a variety of materials, such as carbon nanotubes and silicon. Moreover, a series of chemometrics methods were applied to better understand the resulting data. This chapter is a general overview of these techniques, methods, and materials. Detailed research results, with accompanying reviews of the literature, will be described in the following chapters.

1.1 Materials Characterization Techniques

Throughout my research in the areas of materials science and nanotechnology, several characterization tools were employed to probe the chemical and physical properties of various samples. These analytical techniques include X-ray photoelectron spectroscopy (XPS),[1-3] time-of-flight secondary ion mass spectrometry (ToF-SIMS),[4-5] atomic force microscopy (AFM),[2, 6] scanning electron microscopy (SEM),[2, 7-8] transmission electron microscopy (TEM),[8] spectroscopic ellipsometry,[9-10] and contact angle goniometry.[11] Each technique will be introduced in the following pages. In addition, optical and electrical measurement tools will be briefly described.

1.1.1 X-ray photoelectron spectroscopy (XPS)

XPS was developed in the mid 1960s by Kai Siegbahn at Uppsala University in Sweden.[1] Siegbahn received the Nobel Prize in Physics in 1981 for his significant contributions to this field. XPS is also known as Electron Spectroscopy for Chemical Analysis (ESCA).[2-3] XPS provides valuable information regarding the atomic compositions and chemical (oxidation) states

of the elements at a material's surface. Figure 1.1 shows the physical processes involved in XPS. A solid sample, under vacuum in conventional instruments, is irradiated with a soft X-ray beam of known energy, hν. These X-ray photons interact with the atoms in the near surface region of a material (and deeper), causing photoelectrons to be ejected via the photoelectric effect.[12] However, only electrons from the upper few nanometers of a material can escape without attenuation, which makes XPS a surface sensitive technique. The kinetic energies (KE) of the emitted electrons are measured in an electron spectrometer, which often has a hemispherical geometry. Al Kα (1486.6 eV) (often monochromated with a quartz crystal) and Mg Kα (1253.6 eV) (usually not monochromated) X-rays are commonly used as the incident X-ray beams. The binding energy (BE) of a photoelectron is referenced to the Fermi level of the material, and can be found using the following equation, which is the fundamental equation of XPS:

$$\mathrm{BE} = h\nu - \mathrm{KE} - w \quad (1.1)$$

The work function, w, of a spectrometer i) is also referenced to the Fermi level of the sample, ii) can be viewed as a correction for the electrostatic environment in which the electron is ejected and measured, and iii) is typically 4 – 5 eV, which is generally much smaller than hν, BE, or KE.

XPS is different from the related techniques of Auger electron spectroscopy (AES)[2] and ultraviolet photoelectron spectroscopy (UPS).[2] Ejection of Auger electrons is a three electron process, where the energies of Auger electrons do not depend on the energies of the photons used to create the initial holes in the atoms, but are a function of the energy states within the atom itself. In an XPS experiment, the requirement for creation of an Auger electron is a photon with sufficient energy to eject a core electron in an atom. Another electron then drops down to fill the resulting hole. The energy released in this process can lead to ejection of another electron in the

atom, which is the Auger electron. UPS is similar to XPS except that it uses photons of much lower energy (ca. 40 eV) to probe materials. Hence, UPS is a useful probe of the energies of valence electrons/frontier orbitals in molecules. In general, UPS spectra are much more difficult to understand than XPS spectra, which in many cases are rather simple, often requiring first principle calculations for their interpretation.

An XPS spectrum typically consists of a plot of electron counts as a function of binding energy. Interestingly, it can be plotted with binding energy increasing to the right or to the left, i.e., there is no convention – both approaches are commonly seen in the literature. In addition, the number of counts is often arbitrary because, in general, more signal can typically be obtained by increasing the scan time. In other words, in most experiments, it is the ratios of intensities that matter, not the absolute magnitudes of the peaks. Figure 1.2 shows the X-ray photoelectron survey and C1s narrow scans of a film of 87% hydrolyzed polyvinyl alcohol (PVA). I took these spectra as part of my graduate work. The survey spectrum shows that the polymer is made of two elements: carbon and oxygen. This spectrum also shows the simplicity mentioned above for many XPS spectra. The elemental percentages of carbon and oxygen can be quantified using their peak areas and peak sensitivity factors.[13] For a certain spectrometer, a set of relative sensitivity factors can be developed for the elements. Accordingly, the elemental composition of the PVA sample was calculated from the survey spectrum in Figure 1.2 as 66% carbon and 34% oxygen, which is close to the 2:1 ratio expected from the chemical formula for PVA:

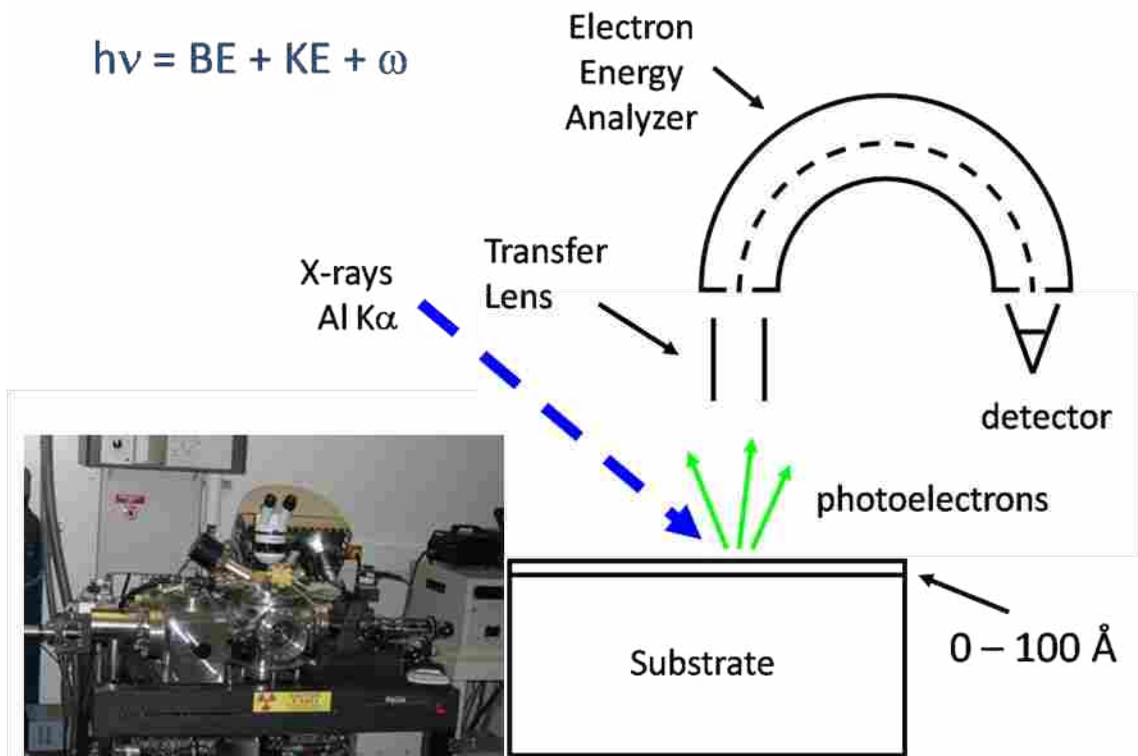

Figure 1.1. Schematic of the X-ray photoelectron spectroscopy (XPS) process, and a photograph of the Surface Science SSX-100 XPS system at BYU.

Several other details in this survey spectrum should also be noted, where these observations have general applicability to X-ray photoelectron spectroscopy. (1) The binding energy for oxygen 1s electrons is higher than that of carbon 1s electrons because of the increased positive charge in the nucleus, i.e., in a series of atoms, the binding energies of electrons from a given orbital increase with Z. (2) Survey scans typically range from 0 eV to 1000 eV (or sometimes 1100 eV), because all elements (except the two that cannot be detected, see below) show a photoelectron peak below 1000 eV. (3) The background rises after the C1s and O1s signals because ejected photoelectrons may lose a fraction of their kinetic energies through inelastic collisions within the solid material they traverse. Compared with their nonscattered counterparts, inelastically scattered electrons have lower kinetic energies and, therefore, present themselves at higher (apparent) binding energies in the spectrum (see Equation 1). (4) An oxygen Auger peak appears at around 1000 eV, which confirms identification of oxygen. Auger peaks are often seen in the XP spectra of the lighter elements. The Auger signal from carbon is not observed in a typical survey scan because its apparent binding energy is greater than 1100 eV.

The peaks in the XPS narrow scan of carbon (C1s) in Figure 1.2 (bottom) represent the different chemical states of the carbon atoms in the PVA sample. Because oxygen atoms are more electronegative than carbon atoms, carbon atoms connected to an oxygen atom in a hydroxyl group exhibit higher binding energy than carbon atoms bonded only to carbon or hydrogen. In addition, because poly(vinyl alcohol) is synthesized by partially or even completely hydrolyzing poly(vinyl acetate) (in our case it is 87% hydrolyzed), there are non-hydrolyzed parts of the PVA molecule, which consist of carboxyl groups from residual polyvinyl acetate moieties. The carbon atoms connected to two oxygen atoms in the carboxyl groups (three

carbon-oxygen bonds) are shifted to higher binding energy (ca. 4.5 eV above carbon bonded only to C or H). Note also the methyl group on the acetate group. The significant electron withdrawl from the carbon adjacent to this $–CH_3$ group results in the methyl carbon being secondarily shifted by ca. 0.7 eV.

Conventional XPS employs ultra high vacuum (UHV) conditions for analysis, although the requirement of UHV conditions has more to do with the need to keep certain samples clean, e.g., freshly etched metal samples, than it is a limitation imposed by the mean free paths of photoelectrons. In typical systems, an antechamber at moderate (or better) vacuum is connected to an analysis chamber at UHV; this antechamber can be seen as a protection to the analysis chamber. Samples are mounted on a sample holder and introduced into the antechamber for an initial pump down, and then into the analysis chamber. Samples can be conductive, e.g., metals or semiconducting materials, or nonconductive, e.g., polymers or ceramics. For nonconductive samples, an electron flood gun provides a steady flow of low-energy electrons for charge compensation. Even with the necessary charge compensation, spectra of insulators are usually shifted by a constant amount and are typically corrected to the unshifted C1s signal from a hydrocarbon (usually taken at 284.6 eV or 285.0 eV). As mentioned, XPS is a surface sensitive technique – only the upper ca. 3 to 10 nm of the surface of a material can be detected. The detection limits for most elements are relatively low – in the parts per thousand. One of the limitations of XPS is that hydrogen and helium cannot be detected. This stems from the low energies of their 1s orbitals (there is a large difference between these energies and the energy of the incident X-rays) and the fact that, for hydrogen, its electron is involved in bonding; therefore, the presence of hydrogen in a molecule is better probed by UPS.[2]

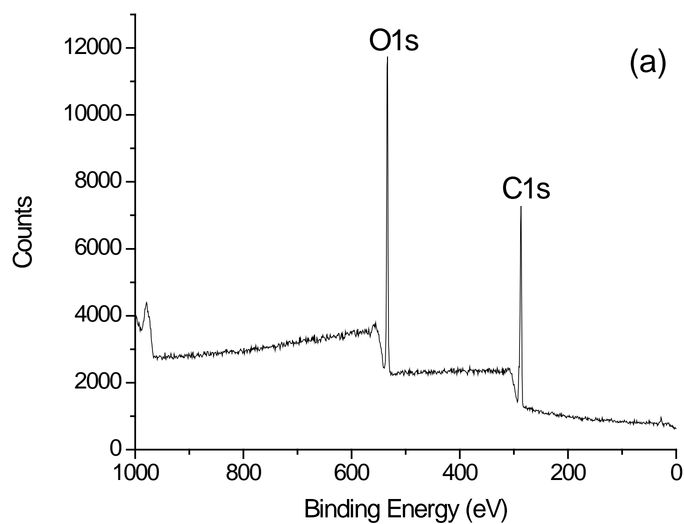

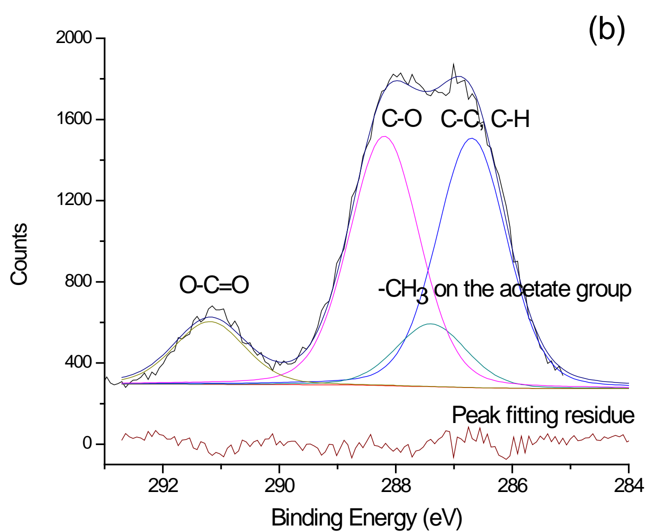

Figure 1.2. X-ray photoelectron spectra of 87% hydrolyzed poly(vinyl alcohol). The peaks in the XPS survey spectrum (a) are labeled by the element and orbital from which the emitted electrons originate. (The Auger signal at ca. 1000 eV from oxygen is not labeled.) The peaks in an XPS narrow scan of carbon (C1s) (b) are labeled according to the chemical states of each carbon atom in the sample.

Overall, XPS is a quantitative spectroscopic technique for surface analysis, which can be used to determine the elemental composition of surfaces, chemical (oxidation) states of elements, and material contamination, etc. Many subtleties of the technique have not been described here. Unlike SIMS, which is discussed next, it does not suffer from a significant matrix effect. Many universities and research centers have XPS instruments, which has facilitated its widespread acceptance and use.

1.1.2 Time-of-flight secondary ion mass spectrometry (ToF-SIMS)

ToF-SIMS[4-5] is a mass spectrometric technique that is even more surface sensitive than XPS. It uses accelerated primary ions to generate secondary ions through collisions of the primary ions with the surface. A time-of-flight device is used as the mass analyzer for these secondary ions (Figure 1.3). In ToF-SIMS ionization, a pulsed, high energy (1-30 keV), primary ion beam is fired at a surface under ultra high vacuum. Secondary neutrals and ions, along with electrons and photons, are emitted from the outermost layer of the sputtered region. Most, often ca. 99%, of the emitted species are neutral atoms and molecules, which is obviously a problem for the technique. Nevertheless, some of the secondary particles are emitted as positively or negatively charged ions. These ions are accelerated, introduced into the drift tube of a ToF analyzer, and then detected.[14] In theory, the ions have the same kinetic energies. The equation for the kinetic energy, E_k, of the ions is given by

$$E_k = zU = \frac{1}{2}mv^2 \tag{1.2}$$

where U is their acceleration voltage, z is the charge on the ion, m is its mass, and v is the velocity of the ion after acceleration. The flight time t of the ions through the tube with length d can be easily derived as

$$t = \frac{d}{v} = \frac{d}{\sqrt{2U}}\sqrt{\frac{m}{z}} \tag{1.3}$$

According to this equation, a series of singly charged ions may be separated, because heavier particles will arrive at the detector later than lighter ones. Thus, a mass spectrum can be obtained as a plot of intensity (number of ions) vs. mass-to-charge ratio (m/z).

Our ToF-SIMS is used in the static mode. Static SIMS is analysis of the top monolayer(s) of a material for prediction of its elemental composition and chemical structure. Static SIMS uses relatively low current densities and total ion doses. On the other hand, dynamic SIMS, which uses much higher ion doses, is used for depth profiling and 3D analysis of materials. Dynamic SIMS is implemented with either one intense beam, typically using one or more high resolution sector analyzers to collect the secondary ions, or with two beams that are used sequentially: a sputtering beam of high brightness followed by a lower intensity analysis beam that probes the center of the crater produced by the first beam. The BYU instrument does not have the sources (or analyzer) necessary for dynamic SIMS.

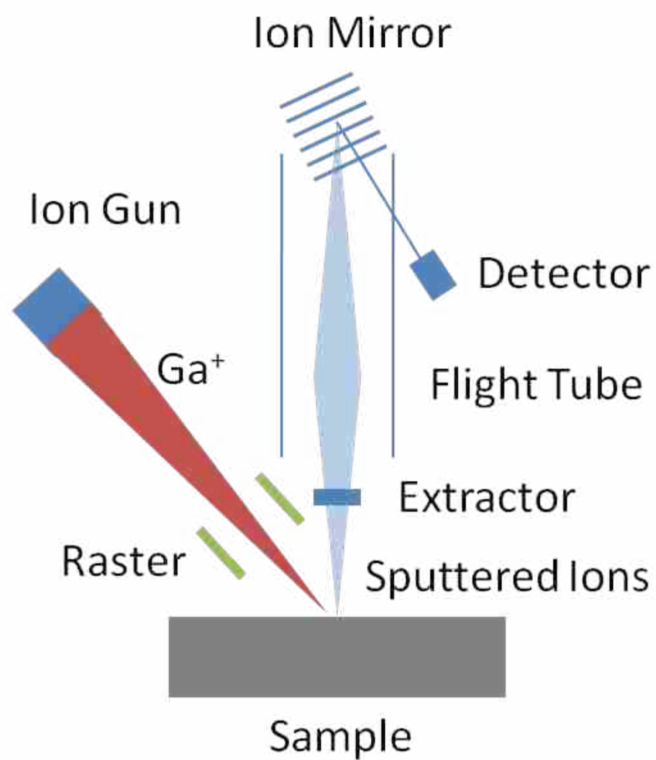

Figure 1.3. Schematic drawing of time of flight secondary ion mass spectrometry (ToF-SIMS) and a photograph of the ION-TOF IV system at BYU.

Several primary ion beam sources, including gallium, indium, cesium, oxygen, SF_6, gold, bismuth, and C_{60}, have been developed for different applications in static SIMS. A gallium ion source, which is a typical liquid metal ion source (LMIS),[15] is used in our ION-TOF IV instrument. With its very low melting point (just above room temperature), liquid gallium is able to wet a tungsten tip. Field emission then occurs when this tip is placed under an intense electric field, e.g., 25 kV. Because the tungsten tip has a radius of a few tens of nanometers, the LMIS provides a tightly focused ion beam of moderate intensity. Note that this source can also be pulsed.

On the analyzer side, compared with quadrupole and magnetic sector analyzers, the ToF analyzer has multiple advantages, including very high transmission, parallel detection of all masses, and (at least in theory) unlimited mass range.[14]

Similar to XPS, ToF-SIMS requires ultra high vacuum, preparatory and analytical chambers with transfer rods, and sample holders. With an electron flood gun, ToF-SIMS can be performed on nonconductive samples. The secondary electrons generated during primary ion bombardment can be detected, allowing a SIMS instrument to function as a low resolution scanning electron microscope. Compared with XPS, ToF-SIMS has better detection limits for many samples – up to parts per million, and spatial resolution better than one micron. Moreover, ToF-SIMS can detect all elements, including hydrogen and helium, isotopes, and even provide molecular information. However, quantitation can be a challenge for ToF-SIMS; SIMS often shows a significant matrix effect. ToF-SIMS and XPS both play an important role in surface characterization, each with unique advantages, where the two methods often serve as

complementary techniques; it is not uncommon to see SIMS and XPS analyses of materials together in the literature.

Both positive ion and negative ion spectra can be obtained by SIMS. Although the detected mass range is unlimited, the low mass region of the spectrum, from approximately 0 m/z to 300 m/z, is most often used in data analysis. This region usually contains information about most elements and molecular species at a surface. Our ToF-SIMS system has an imaging mode to visualize the distribution of chemical species on the sample surface, and in this mode it can be viewed as a chemical microscope. Enormous quantities of data can be taken in this way. For example, in a 256 × 256 resolution ToF-SIMS image, with a complete mass spectrum at every pixel, more than 10 million numbers can be obtained. It may be challenging to find useful information in a data set of this size. For large data sets of ToF-SIMS spectra and images, chemometrics methods are regularly used for data interpretation and data mining.

1.1.3 Atomic force microscopy (AFM)

AFM is one of the scanning probe microscopy (SPM) techniques, which uses a sharp probe or tip that is rastered across a sample surface.[16] The interaction between the probe and surface is monitored. AFM is a high resolution surface analysis technique, which can topographically characterize sample surfaces at micron and even nanometer scales. AFM was invented by Binning, Rohrer, Gerber, and Weibel in 1982. Several operational modes have been developed for AFM, including contact mode, non-contact mode, and tapping mode.[6, 17-18] In my research, most of the AFM measurements were performed in tapping mode. The following is a basic introduction to the theory of the AFM tapping mode.

As shown in Figure 1.4, a sharp tip is attached to the end of a cantilever. The cantilever is mounted on a tip holder and connected to a scan tube. During tapping mode operation, the cantilever is oscillated at or slightly below its resonance frequency of a few hundred kilohertz with an amplitude of 20 – 100 nm. The tip gently “taps” on the sample surface, contacting the surface at the bottom of its swing. Since the tip only periodically touches the surface, and for only a brief period of time, the problem of surface damage that takes place in contact mode scanning is largely avoided. The motion of the tip with the cantilever is monitored by an optical beam deflection detector. Before engaging the tip to the sample surface, a laser beam is aligned with the tip and reflected onto the center of a photodiode. During the AFM scan, changes in the oscillation amplitude are monitored according to the output from the photodiode detector. A feedback loop then adjusts the vertical position (z) of the scanner tube at each (x, y) location in order to maintain a constant oscillation amplitude. The scanner is made from a piezoelectric material, which expands and contracts proportionally to the applied voltage. The individually operated piezo electrodes can manipulate the tip and sample with outstanding precision in the X, Y, and Z directions. During AFM imaging, a constant interaction between the tip and sample surface is maintained and (x, y, z) data points are stored in a computer to form a topographic image of the sample surface.

AFM probes (tips and cantilevers) are produced by semiconductor fabrication techniques.[19-21] Various types of probes have been developed from different materials (such as silicon and silicon nitride), with different structures (pyramidal and cone-shaped), with different coatings (aluminum or gold), and modifications (diamond, nanotube), etc. Figure 1.5 shows a schematic for, and specifications of, a typical tapping mode probe used in my research.

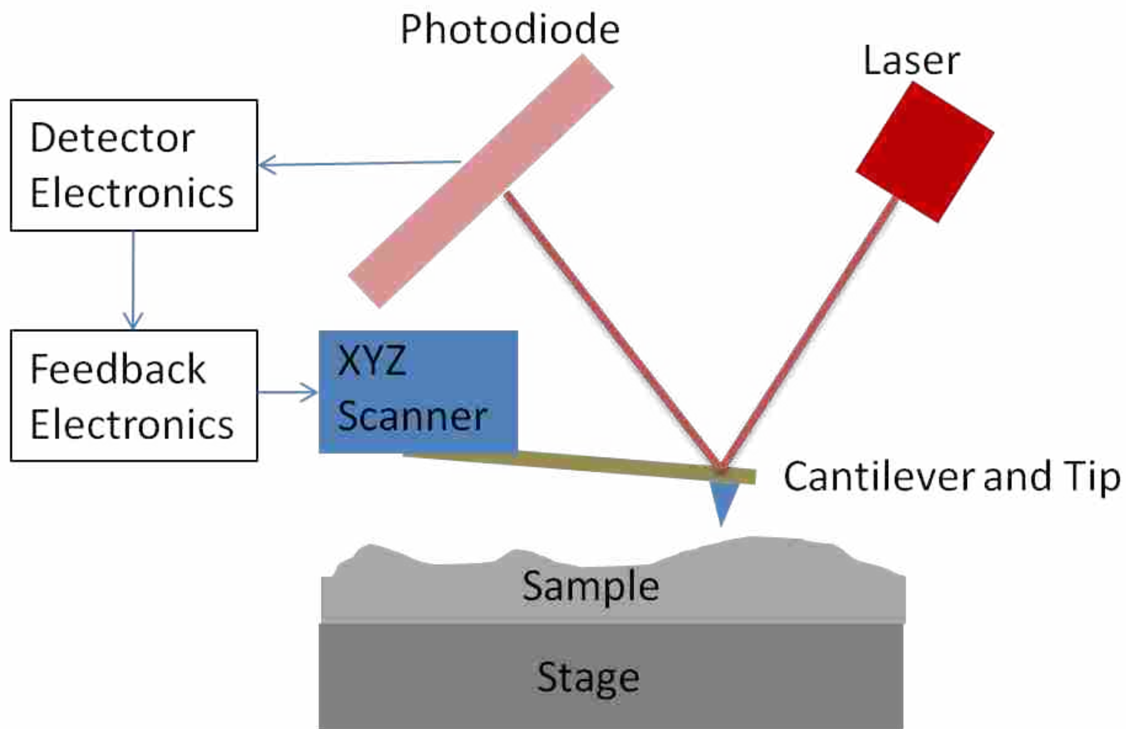

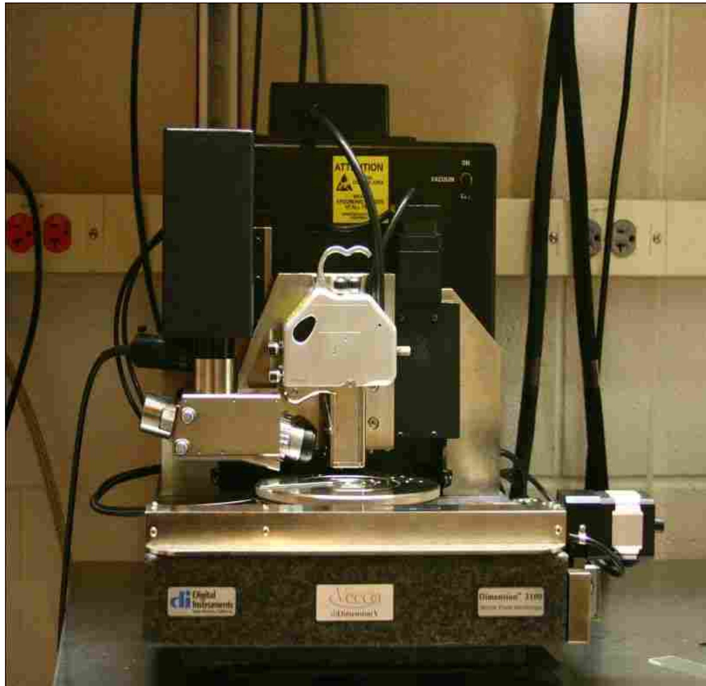

Figure 1.4. Schematic of atomic force microscopy (AFM) and a photograph of the Veeco Dimension V system at BYU.

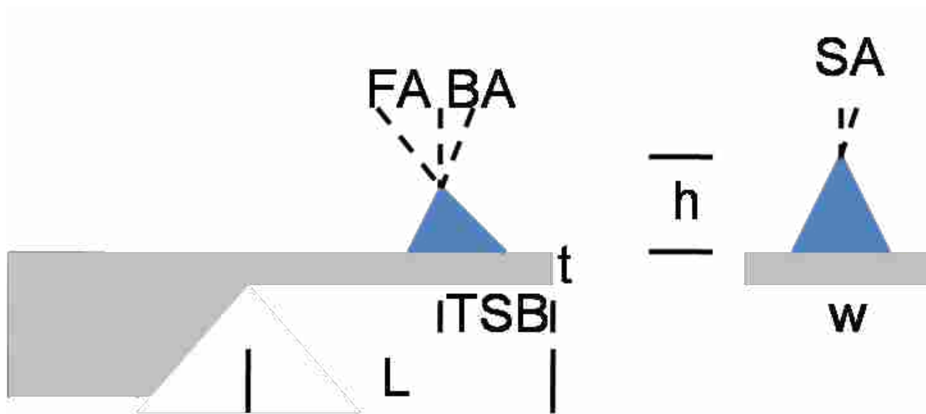

Tip specifications		Cantilever specifications	
Geometry	Anisotropic	Thickness (t)	3.5 ~ 4.5 µm
Tip height (h)	10 ~ 15 µm	Width (w)	25 ~ 35 µm
Front angle (FA)	25° ± 2.5°	Length (L)	110 ~ 140 µm
Back angle (BA)	15° ± 2.5°	Frequency	230 ~ 410 KHz
Side angle (SA)	22.5° ± 2.5°	k	20 ~ 80 N/m
Tip set back (TSB)	5 ~ 25 µm	Coatings	None

Figure 1.5. Schematic and specifications of a Veeco TESP silicon probe.

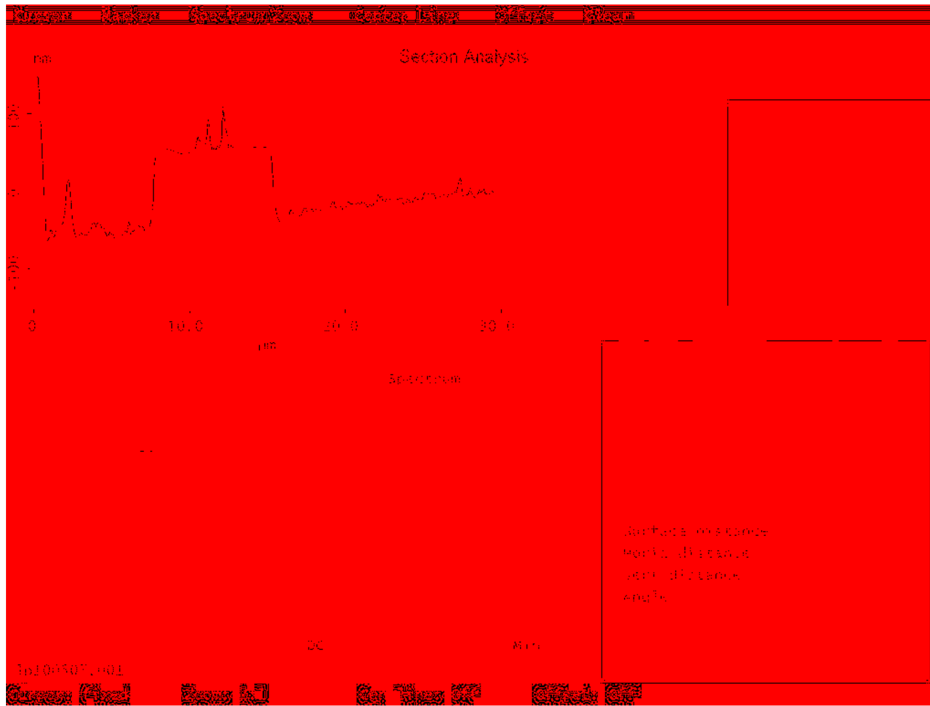

Figure 1.6. AFM measurements on a patterned polymer composite structure.

Compared to other scanning probe techniques, AFM has unique advantages.[17] (1) AFM does not require high vacuum. (2) AFM can provide direct height measurements with nanometer scale resolution. (3) AFM is versatile. For example, both samples and tips for scanning tunneling microscopy (STM) must be conductive, but AFM can analyze non-conductive samples and even surfaces in liquid environments (with conductive or non-conductive tips). Thus, imaging of polymers and biological samples is possible. However, AFM is somewhat limited in the range of features it can measure. It cannot measure differences in height of more than a few micrometers (the total variation in height for our system is 7 μm), and the measurement area for each scan on our system cannot exceed 100 μm × 100 μm.[6]

In my research, AFM was mostly used to obtain film thickness and roughness measurements. Figure 1.6 shows the AFM image of a patterned polymer composite structure that I made and characterized as part of my graduate work. From the section analysis curve in this figure, the thickness of the structure can be determined. Also, from the height contrast, the roughness of the composite pattern can be calculated. In addition, the following useful 'trick' can be used to measure film thicknesses by AFM. A line is first drawn across a substrate with a Sharpie® marker prior to a coating process, e.g., sputtering or thermal evaporation. After the film coating, the marker line can be dissolved in acetone, which exposes the substrate/removes the film. The height difference between the coated and uncoated regions of the substrate obtained by AFM corresponds to the thickness of the film.

1.1.4 Scanning electron microscopy (SEM)

Electron microscopy is an important technique for imaging sample surfaces at resolutions in the micro- and nanometer range.[2, 7] Analogous to optical microscopy, which uses optical lenses to focus light, electron microscopy uses electromagnetic lenses and directs an electron beam to obtain an image. Since electrons have much shorter wavelengths than photons, higher magnifications and greater resolving power can be achieved via electron microscopy than optical microscopy.

SEM, a type of electron microscopy, scans the surface of a solid sample in a raster pattern with a high energy electron beam. Five types of signals are produced from surfaces in this process.[2] (1) Backscattered electrons (BSE) are generated by elastic collisions with surface atoms. (2) Secondary electrons (SE) are emitted from surface atoms, which are excited by inelastic collisions with primary electron beams. (3) X-ray photons are created. (4) Auger electrons are generated, where primary ions provide the energy needed to create the initial hole in an atom. Auger electrons are also produced in the XPS process (see above). (5) Other photons of various energies are produced. These signals can be detected to obtain different types of information. For example, BSE can be used to produce topographic images with atomic number contrast, as well as to determine the crystallographic structure of specimens.[22] X-ray photons can be collected by an X-ray detector for energy-dispersive X-ray spectroscopy (EDX).[23] In my research, I mostly used SE images for surface topographic analyses, pattern profile characterization, and film thickness measurements, etc. For this SEM mode, an SE detector is mounted in the chamber over the sample. A through-the-lens detector (TLD)[23] is mounted within the SEM lens. Since secondary electrons have to pass through the lens pole piece into the collector, TLD collects secondary electrons from immediately over the scanned area of the

sample and yields ultra high resolution (UHR) images. For example, Figure 1.7 shows SEM images of vertically aligned carbon nanotube forests under UHR mode that I fabricated and then analyzed by SEM. These images show a patterned forest profile in three-dimensions and reveal the quality of carbon nanotube bundles.

Our instrument at BYU, the FEI Philips XL30 S-FEG SEM system shown in Figure 1.7, uses a field emission gun (FEG)[2] to emit primary electrons. The FEG can produce an electron beam that is smaller in diameter, more coherent, and of greater current density or brightness than conventional thermionic filaments, so that signal-to-noise ratios and spatial resolution can be largely improved. After a sample is attached to a metal stub with conductive tape and placed on the SEM stage, the SEM chamber is pumped down to around 10^{-5} torr for analysis. The electron beam is then set to a desired acceleration voltage and spot size. Focus and stigmation need to be well adjusted to obtain a clear image.

For some analyses, sample preparation is required. For example, a few nanometers of gold is normally sputtered onto non-conductive samples in order to reduce charging and improve image contrast. If cross-sectional profiles are needed, freeze-fracturing or freeze-and-break methods can be very useful. Ion milling via focused ion beams (FIB)[24] can also be used to create fine cross-sectional profiles.

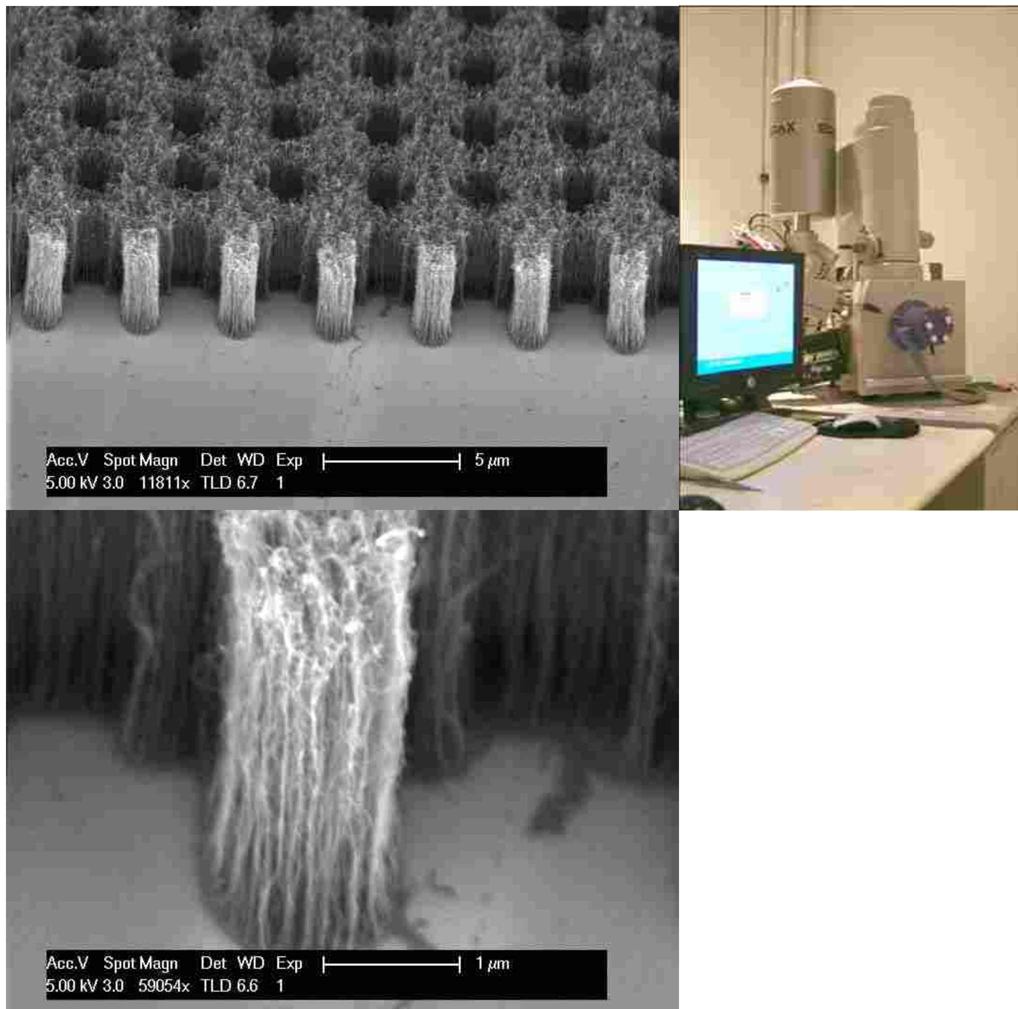

Figure 1.7. SEM images of a vertically aligned carbon nanotube forest and the FEI Philips XL30 S-FEG SEM system at BYU.

1.1.5 Transmission electron microscopy (TEM)

TEM is also a type of electron microscopy.[8, 25] In TEM, an electron beam is transmitted through an ultrathin sample. An image is captured based on the interaction of the transmitted electrons with the sample. TEM is capable of imaging at very high magnification and resolution. For example, Figure 1.8 shows TEM images of carbon nanotubes and nanotube bundles that I made and then characterized with this technique. Moreover, TEM can be used in several modes to perform a variety of material analyses (topographical structure, atomic composition, chemical bonding status, crystalline lattice structures, and crystallographic orientation), including bright field, diffraction, EDX, electron energy loss spectroscopy (EELS), and scanning TEM.[25]

TEM's greatest limitation may be the need for extensive sample preparation, since it is necessary to thin a sample to only a few tens of nanometers. For carbon nanotube analysis, the TEM sample can be prepared by depositing a dispersion of carbon nanotubes in a solvent such as dichloroethane onto a copper TEM grid, and then vaporizing the solvent. For bulk materials and thick films, samples may be prepared by mechanical polishing, chemical etching, or focused ion beam (FIB) milling.[24]

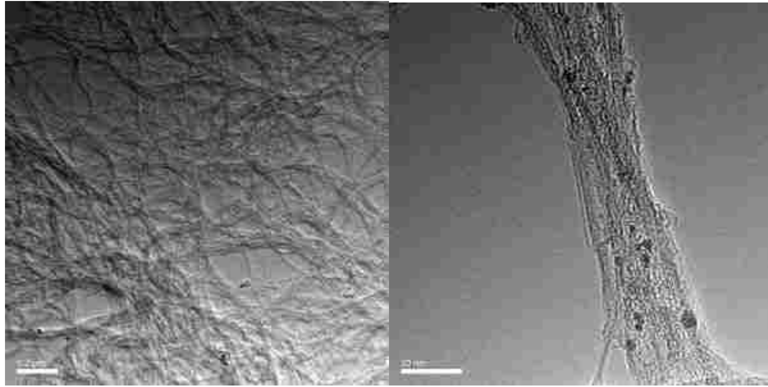

Figure 1.8. TEM images of carbon nanotubes and bundles. The TEM sample was prepared by placing droplets of a dispersion of carbon nanotubes in dichloroethane on a TEM grid and then vaporizing the solvent.

1.1.6 Ellipsometry

Ellipsometry is a surface sensitive technique for thin film thickness measurements, which consists of analyzing the interaction between light and thin film materials.[9, 26-27] As shown in the schematic drawing in Figure 1.9, a polarized beam of light is reflected from the surface of a thin, planar film, and also substrate, at a certain angle of incidence. The output polarization is then measured. Since the polarization state of the incident light is known, the change in polarization, expressed as an amplitude ratio (Ψ) and any phase difference (Δ), can be obtained as functions of wavelength and angle of incidence. The polarization change is also related to the film thickness and optical constants of the film, or films, and substrate.[26]

Film thickness and the incident angle of the light affect the path length of light in the film. The optical constant n determines the light velocity and its angle of refraction. The optical constant k determines the degree to which the light is absorbed by the material. Although film thickness and/or optical constants cannot be directly measured by ellipsometry, i.e., ellipsometry can only determine Ψ and Δ, these values can be determined through an iterative fitting of a model. The model contains the wavelengths of light (our spectroscopic ellipsometer uses multiple wavelengths), incident angles, and information about the beam polarization states, as well as guesses of the film thickness and optical constants. In my research, the optical constants of a material layer are already quite well known. Thus, an initially predicted value of film thickness can be used to calculate the polarization change curves. The mean squared error (MSE) of the fit is used to quantify the difference between the calculated curves and the experimental curves. An unknown thickness is allowed to vary until a minimum in MSE is reached.[26] Of course, by this method, a model with unknown optical constants can also be successfully used

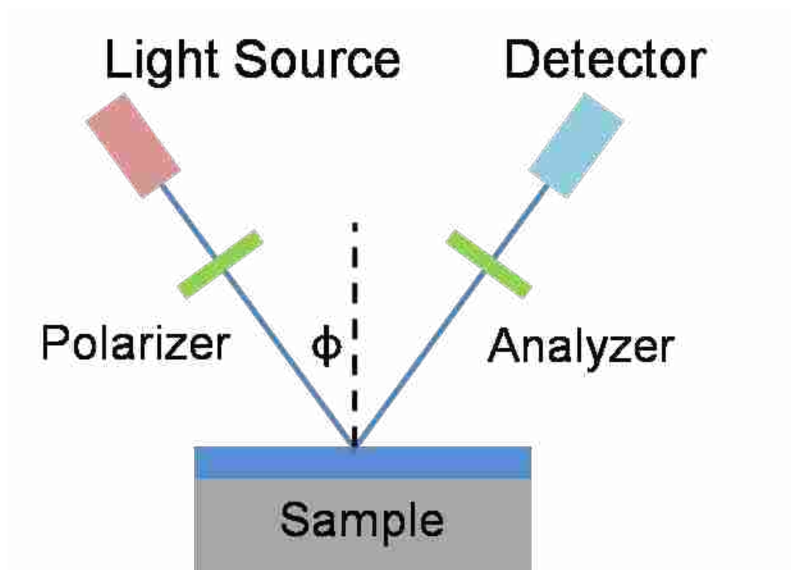

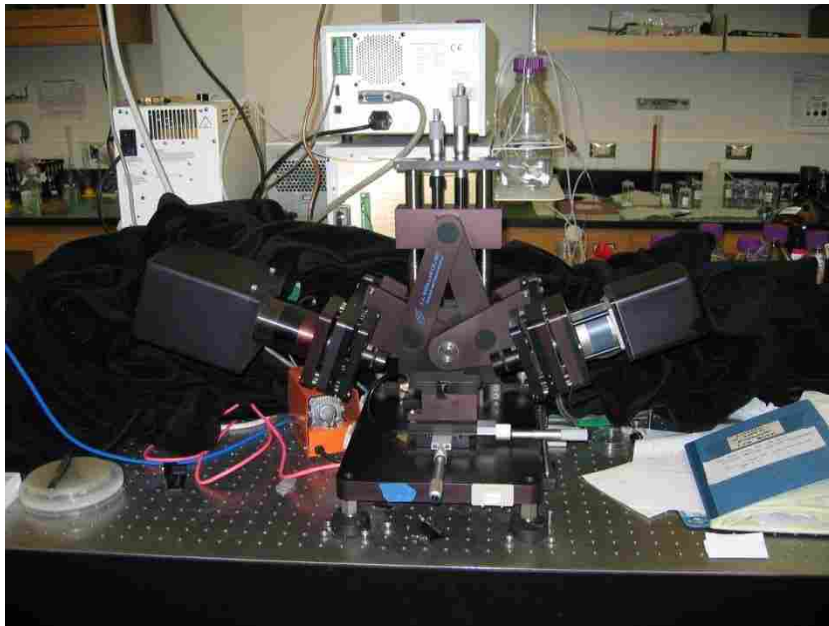

Figure 1.9. Schematic drawing of an ellipsometer and a photograph of the J. A. Woollam M-2000D spectroscopic ellipsometer system at BYU.

with a known film thickness that has previously been measured by AFM or another technique.

Ellipsometry is typically used to determine film thicknesses of single layers and multilayer stacks ranging from less than 1 nm to several micrometers in thickness with excellent accuracy. When films become thicker than several tens of microns, interference oscillations become increasingly difficult to resolve.

Ellipsometry is a fast and precise technique for film thickness measurement, which was routinely used in my research to monitor thickness changes in silicon dioxide and of polymer layers in my polymer fabrication processes.

1.1.7 Water contact angle goniometry

Contact angle goniometry is a quantitative technique for measuring the wettability of a solid by a liquid.[11] Figure 1.10 shows the shape of a small liquid droplet resting on a flat horizontal surface. As shown in Figure 1.10, the contact angle, θ, is the angle between the tangent line of the drop and the solid surface. A low contact angle (less than 90°) indicates that wetting of the surface with the probe liquid is favorable, and in the case of water, that the solid surface free energy is high. That is, the liquid will spread to some degree over the solid surface. A high contact angle (greater than 90°) means that wettablity of the surface with the probe liquid is poor, so that the liquid will form a compact droplet, minimizing its contact area with the surface. For water, a wettable surface can be termed 'hydrophilic' and a non-wettable surface 'hydrophobic'. In my research, contact angle measurements were frequently used to verify surface functionalization and modification processes. For example, a bare silicon wafer normally has a water contact angle less than 10°. After a perfluorosilane treatment, the water contact angle of this same surface will increase to over 118°, which indicates that the surface has been

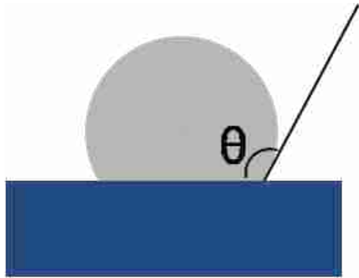

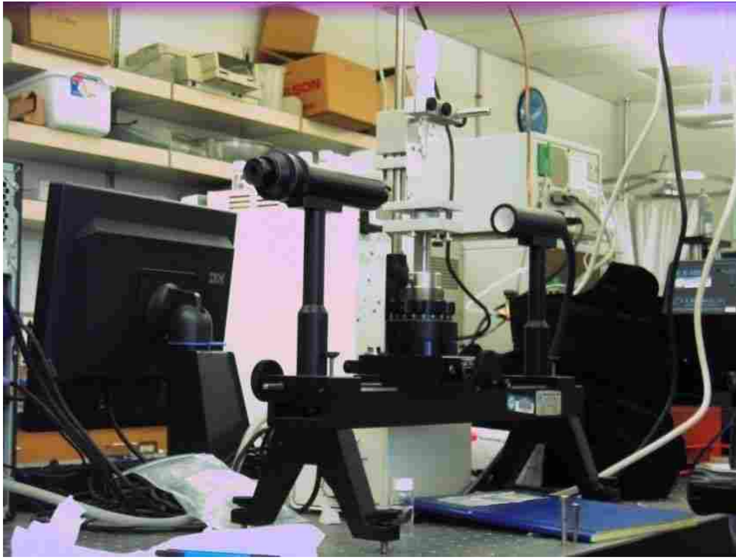

Figure 1.10. Schematic of the contact angle measurement and a photograph of the Ramé-Hart 100 water contact angle goniometer at BYU. A liquid droplet rests on a solid surface. The contact angle, θ, is the angle between the tangent line of the drop and the solid surface.

successfully changed from hydrophilic to hydrophobic and that it can then be used as an anti-adhesion layer.[28]

1.1.8 Optical measurements

Optical transmission and reflection measurements are very useful for probing the optical properties of photovoltaic materials. In my research, an optical measurement was performed on a nanostructured PDMS sample containing amorphous and nano-crystalline silicon layers. Due to light scattering and diffraction from these surfaces, an integrating sphere technique is required.[30] The setup is shown in Figure 1.11. A tungsten lamp, functioning at 7.5 V, was used as the light source. The light beam was collimated with a lens tube. The light was then passed through an aperture to reduce the beam diameter to approximately 3 mm, which was small enough to be easily aligned with a 5 mm × 5 mm nanopatterned area. A two-inch diameter integrating sphere device with a 99% reflectance coating (Thorlabs, IS236A-4) was used for high quality optical measurements, including transmission, reflection, and incident beam intensity measurements. In theory, an integrating sphere is an enclosure that contains and diffuses input light so that it is evenly spread over the entire surface area of the sphere. Two mechanisms are required to complete this diffusion: (1) a Lambertian reflectance surface (or coating),[31] which has a near 100% reflectance, and completely uniform angular spreading of the light energy on the first bounce, and (2) a spherical shape, which ensures that every point within the sphere receives the same intensity or amount of light as every other part of the sphere on the first bounce. Therefore, ideally, the light incident into an integrating sphere is spread evenly and without angular distribution over the entire surface of the sphere.[29] A Czerny-Turner CCD spectrometer (Science-Surplus, Compact Fiber Coupled CCD Spectrometer, 365 - 1100 nm) was fiber coupled to the detector port of the integrating sphere.

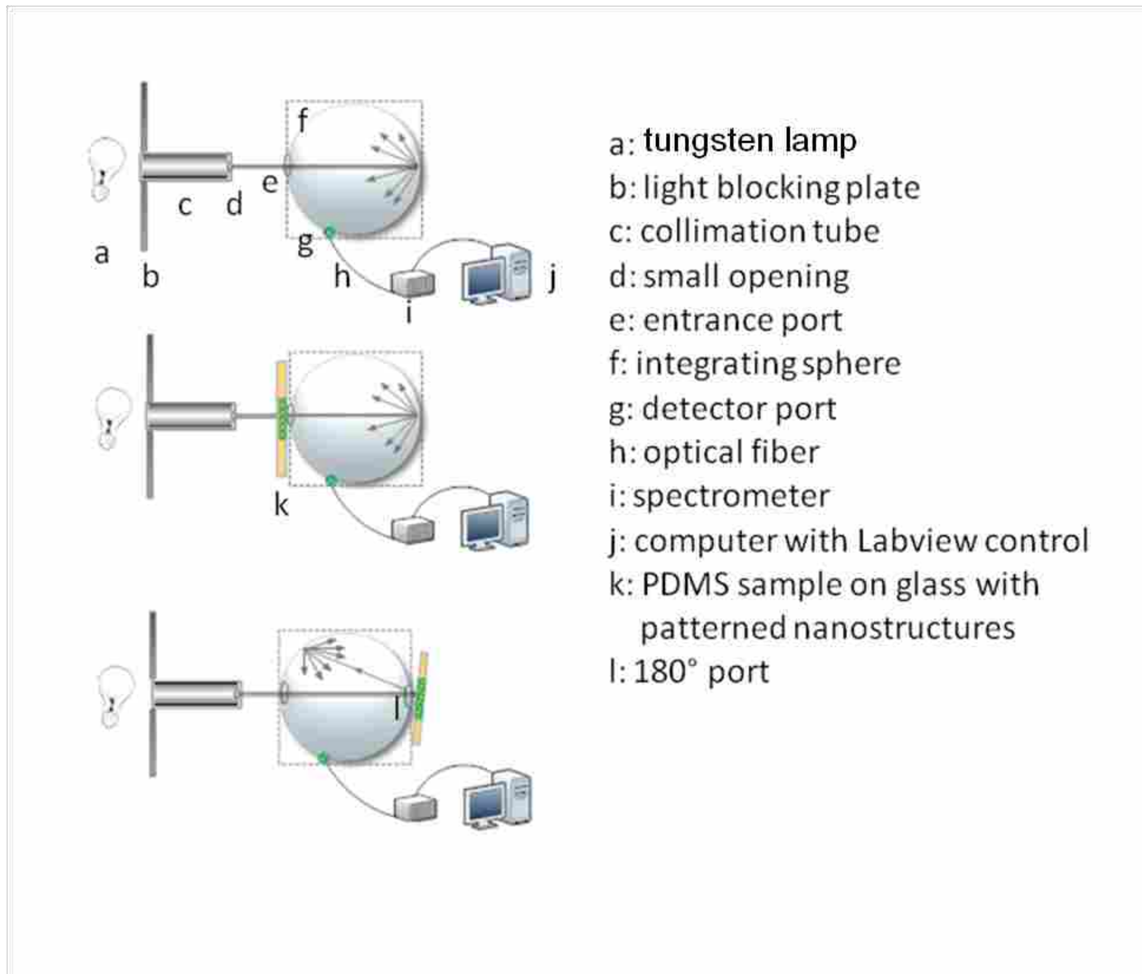

Figure 1.11. Schematic of optical measurements with an integrating sphere.

For the total beam intensity measurements, the entrance port of the integrating sphere was opened but the sample port at 180º was closed. The incident beam passed through the center of the entrance port striking the diffuse white reflective surface on the sample port scattering evenly around the sphere. The spectrum thus obtained was used as the "total" beam intensity for comparison with the transmission and reflection spectra. For transmission measurements, the sample was placed perpendicular to the incident beam in front of the entrance port. For reflection measurements, the 180˚ port of the integrating sphere (opposite the entrance port) was opened and the sample, tilted at a 5˚ angle relative to the perpendicular, was placed up against this port. The tilt on the sample ensures that light reflected specularly from the sample hits the side of the integrating sphere. Without it, specular light could leave through the entrance port and not reach the detector.

1.1.9 Electrical conductivity measurements

A four-point probe measurement[32] was performed to obtain the electrical sheet resistivity of a thin film coating. Using four probes eliminates measurement errors due to the contact resistance[33] between each metal probe and the specimen material. As shown in the scheme in Figure 1.12, a four-point probe consists of four equally spaced tungsten metal tips of finite radius. The probe spacing is 1/16 inch. The tips are supported with springs to minimize sample damage when the metal tips engage and withdraw during measurements. A high impedance current source is used to supply current through the outer two probes; a voltmeter measures the voltage across the inner two probes to determine the resistivity of the material.

When the thickness (t) of a thin film is much less than the probe spacing, the sheet resistance can be expressed as:

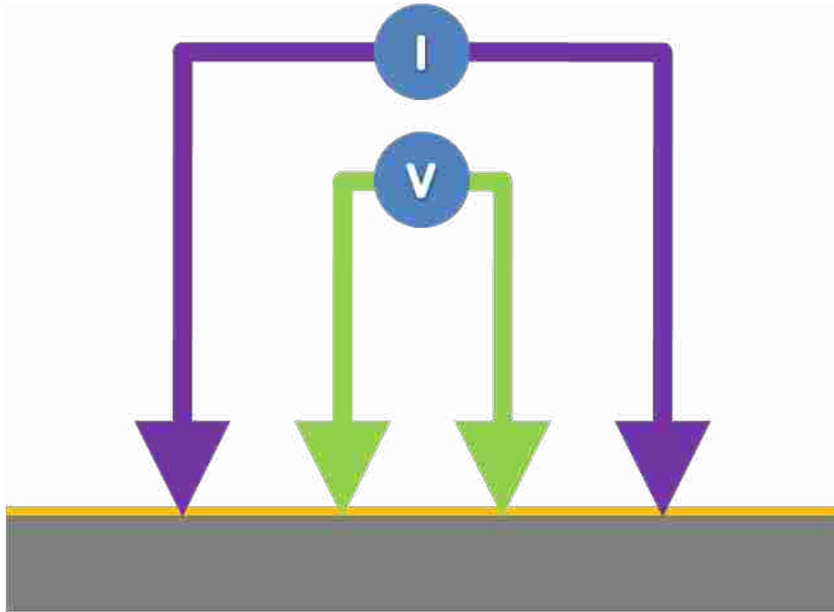

Figure 1.12. Schematic of the four point probe measurement for electrical sheet resistivity measurements.

$$Rs = \frac{\rho}{t} = \frac{\pi}{\ln 2}\left(\frac{V}{I}\right) \quad (1.4)$$

where ρ is the material resistivity, V is the measured voltage, and I is the known current. The common unit of the sheet resistance is Ω/□.

1.2 Materials Fabrication Techniques

In addition to the materials characterization techniques described above, I have learned and studied several fabrication techniques during my research. These fabrication techniques are mostly focused in three areas: thin films coating, surface patterning, and materials etching. Thin film coating techniques include spin coating,[34] thermal evaporation,[35] electron-beam evaporation,[35] sputtering,[35] and silane chemical vapor deposition (CVD)[36]. Surface patterning involves one or more of the following: photolithography,[37] electron beam lithography,[38] nanoimprint lithography,[39-40] and laser modification.[41] Finally, materials etching can consist of wet etching,[42] plasma etching,[43] or inductively coupled plasma reactive ion etching (ICP-RIE).[42] Each technique will be briefly introduced in the following paragraphs. In addition, a specific description of how I used the technique is also provided in some cases.

1.2.1 Spin coating

Spin coating[34] is used to deposit uniform thin films on flat substrates with controllable thicknesses. In my research, polymer films with thickness between a few nanometers and several micrometers were produced by spin coating. For the spin coating process, a solid substrate is loaded onto the spin coater (Figure 1.13), where it is held with a vacuum chuck. After an excess amount of a solution is placed on the substrate, the substrate is spun at high speed in order to spread the solution under the centrifugal force. Most of the material in the solution eventually runs off the edges of the substrate, while the volatile solvent simultaneously evaporates, leaving

Figure 1.13. Photograph of the Laurell spin coater at BYU.

(at least in theory) a uniform thin film. Final film thickness depends on the nature of the solution (viscosity, drying rate, concentration, and surface tension), the wettability of the substrate, and the spin casting profile (the spin rate, acceleration, and fume exhaust rate).

1.2.2 Thermal evaporation

Thermal evaporation is a physical vapor deposition (PVD) technique, which deposits thin films by the condensation of vaporized materials onto sample surfaces.[35] For thermal evaporation, the source material is heated with an electrically resistive filament or boat, and evaporated in a vacuum. Vaporized atoms and molecules travel directly to the target substrate and form a thin film. A quartz crystal monitor[44] is used to measure the deposition rate and film thickness. A shutter plate covering the sample surface is opened when the deposition rate becomes stable, and remains open until a film of desired thickness is achieved.

1.2.3 Electron-beam evaporation

Electron beam (e-beam) evaporation[35] is also a PVD technique that is performed in a vacuum chamber. A high DC voltage is applied to a tungsten filament that causes electrons to be discharged. The emitted electron beam is directed to a target, where it heats the target (the deposition material) and vaporizes it. This material travels to the substrate where it condenses back to the solid state. The deposition rate can be precisely controlled by the electron beam current. In my research, an alumina film was deposited by e-beam evaporation onto a silicon wafer as a catalyst support layer for carbon nanotube growth.[45]

1.2.4 Sputtering

Sputtering is another PVD technique for thin film coating.[35, 46] By applying a DC or RF high voltage across a low pressure gas (often argon at 3-10 mTorr), a plasma can be created. This

plasma contains electrons and ions in a high energy state. During sputtering, plasma particles strike the desired target. Atoms at the target are then ejected or sputtered onto a substrate.

Compared with thermal or electron beam evaporation, sputtered films typically show better adhesion to the substrate.[47] Sputtering can also deposit materials with very high melting points and/or alloys, which can be difficult or impossible with evaporation techniques. However, sputtering produces many high-speed atoms that bombard a substrate and may damage it.

In my research, materials such as iron, alumina, and indium tin oxide were sputtered with a Kurt J. Lesker PVD 75 system.

1.2.5 Chemical vapor deposition (CVD)

Chemical vapor deposition involves chemical reactions, which transform gas phase precursors into a solid thin film on the surface of a substrate.[36] For example, Figure 1.14 shows a perfluorosilane CVD process that was used to coat a silicon wafer with a hydrophobic film. Prior to this deposition, the silicon wafer was cleaned with piranha solution (H_2SO_4/H_2O_2) to introduce hydroxyl groups onto the silicon surface. The silicon wafer was then put in a desiccator. A drop or two of trichloro(1H,1H,2H,2H-perfluorooctyl)silane (448931, Sigma-Aldrich) was put in two scintillation vials, which were placed beside the wafer. The desiccator chamber was evacuated with a rough pump for 10 min to accelerate the silane vaporization. The desiccator was sealed and silane deposition was allowed to proceed overnight. During the deposition, perfluorosilane molecules reacted with silanol groups on the silicon surface. The reaction results in the formation of Si-O bonds and the release of HCl gas. Finally, a silicon wafer with a non-stick coating is obtained.

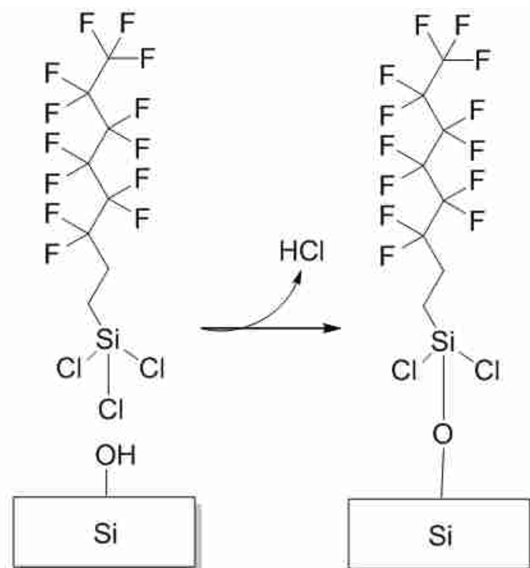

Figure 1.14. Reaction of a perfluorosilane onto silicion dioxide by CVD.

1.2.6 Photolithography

Photolithography is a patterning process used in microfabrication.[37] In photolithography, ultraviolet light is typically directed through a photomask, which is generally a transparent fused silica plate covered with a pattern defined by an optical absorbing chromium film. Figure 1.15a shows an example of a photomask used in my research. UV light is blocked in the chromium-covered regions, but passes through the blank areas and exposes a photoresist layer beneath these areas. A photoresist is a light-sensitive material that generally comes as one of two types: positive or negative. An exposed positive resist is decomposed and becomes soluble in a developing chemical, but the unexposed positive resist remains insoluble in the developer. On the other hand, an exposed negative resist becomes crosslinked and insoluble in the developer, where the unexposed negative resist is dissolved by the developer. As shown in Figure 1.15b, a positive photoresist (AZ3330, a Novolac or phenol formaldehyde resin)[48] was spin coated onto a bare silicon wafer, and prebaked on a hotplate to drive off excess photoresist solvent. The sample and the predesigned photomask were loaded into a mask aligner (Karl Süss Mask Aligner). The photoresist sample was covered with the photomask and then exposed to UV light for a few seconds. The sample wafer was taken out of the aligner, dipped in a photoresist developer, rinsed with water, and dried under a flow of nitrogen. As the exposed positive photoresist was dissolved during development, the photoresist was patterned according to the photomask design. Figure 1.15c shows an optical image of a patterned photoresist layer from my research after development. The patterned photoresist layer in turn protects the underlying material for subsequent fabrication steps.

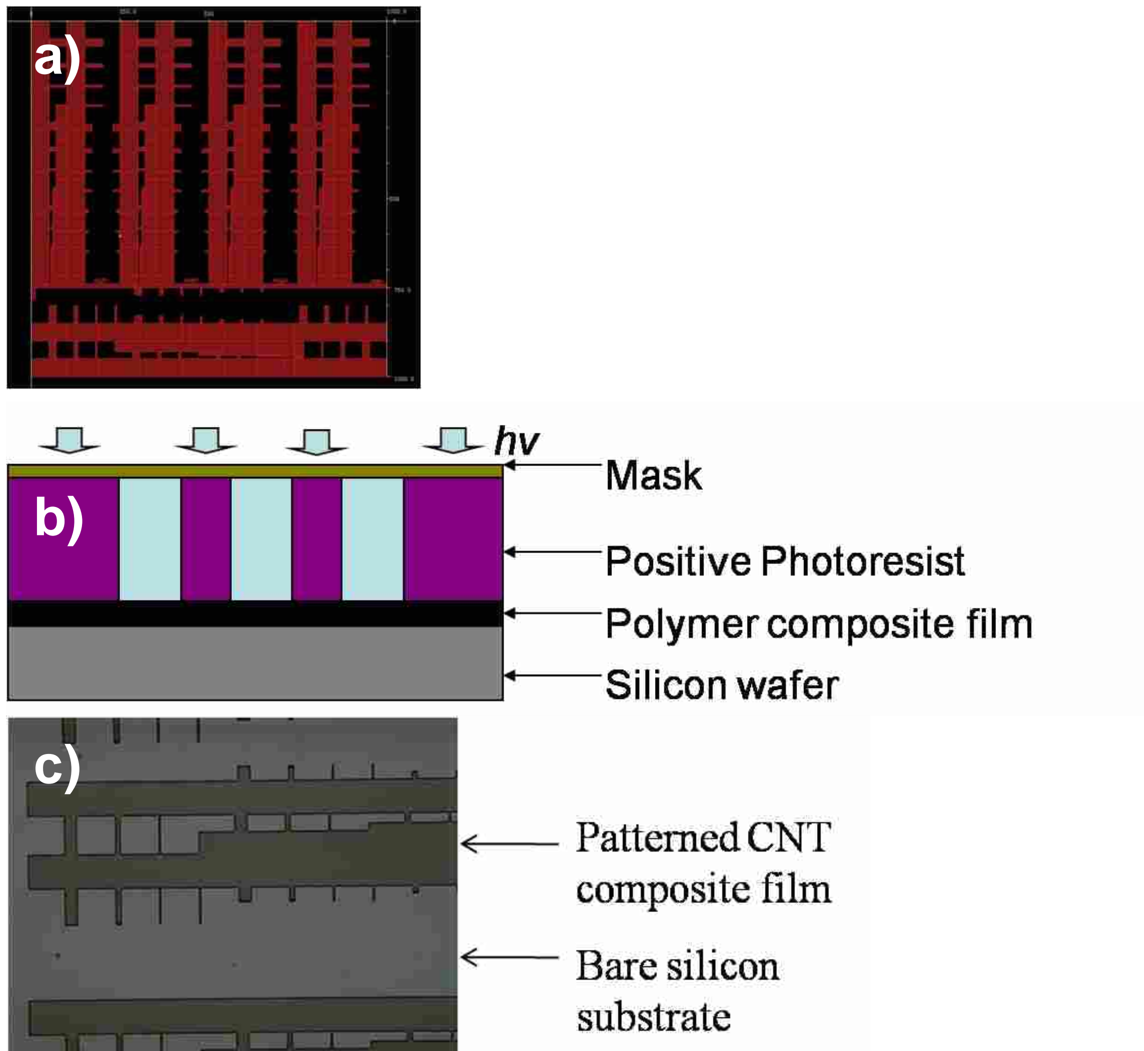

Figure 1.15. (a) Mask design for photolithography, (b) schematic of the photolithography process, and (c) optical image of a photoresist layer patterned by photolithography. Images (a) and (c) were obtained as part of my research.

1.2.7 *Electron beam lithography (EBL)*

EBL is a patterning technique in which an electron beam is scanned across the surface of an electron beam resist in a patterned fashion.[38] Unlike photolithography, EBL has the advantage of making high resolution patterns at nanometer scales without the limitations of light diffraction. It also has the advantage of being a maskless technique. For my research, the electron beam in a scanning electron microscope (SEM) was used for EBL. However, EBL processes are quite time consuming for relatively large areas of exposure. Like photoresists, electron beam resists[49] come in two types: positive and negative. In my research, ZEP 520A (Nippon Zeon) was selected as a positive electron beam resist to make a grid pattern with around 200 nm wide lines. This was done because: (1) compared to other resists such as poly(methylmethacrylate) (PMMA), ZEP is relatively more resistant to reactive ion etching (RIE), i.e., because the RIE process etches both silicon and resist, ZEP is a better candidate to produce high aspect ratio structures; (2) ZEP has high sensitivity, which is particularly valuable for large area patterning; and (3) it is easier to obtain a grid pattern using a positive electron beam resist than a negative one.

1.2.8 *Nanoimprint lithography (NIL)*

I also used NIL, a low cost nanoscale patterning technique. NIL is one of the next-generation lithography (NGL) techniques, which is an alternative to traditional optical photolithography. Instead of using photons or electrons to modify the resist properties, NIL mechanically molds the resist material, forming patterned nanostructures.[39-40,50] There are several advantages of NIL over other lithography techniques: (1) NIL can achieve high resolution without the limitations set by the diffraction of light or beam scattering; (2) NIL instruments are typically less expensive than lithography methods that use complex optics and sophisticated light

sources, e.g., extreme UV lithography (EUV); (3) NIL generally has much higher patterning speed than e-beam lithography; (4) NIL offers high throughput with great precision; and (5) NIL has the ability to reduce processing steps because it can pattern both functional materials and 3D structures.

1.2.9 Wet etching

In a wet etching process, a sample substrate is immersed in an active solution.[42] The etchants in the solution chemically remove layers from the substrate. I used two types of wet etching solutions in my graduate research: piranha solution and hydrofluoric acid (HF).

Piranha solution is a mixture of concentrated sulfuric acid (H_2SO_4) and hydrogen peroxide (H_2O_2).[51] When heated to around 90°C, the piranha solution can aggressively react with organic residues on surfaces. In addition to cleaning sample surfaces, piranha solution makes silicon wafers or glass slides hydrophilic by hydroxylating their surfaces. In my research, piranha solution has been used to remove photoresist residues on patterned silicon wafers and to introduce silanol groups onto surfaces for subsequent silane-based surface modifications.

Aqueous HF is a common etchant for silicon dioxide. HF molecules react with SiO_2 and form water soluble H_2SiF_6.[52] However, HF etches silicon slowly, leaving a hydrophobic hydrogen-terminated silicon surface after etching. In my research, HF etching has been used for two purposes: (1) aqueous HF was used to prepare a hydrogen-terminated silicon surface, which was used as a target for producing organically functionalized silicon nanoparticles via laser ablation;[53] and (2) a silicon dioxide layer was used as a sacrificial layer. For example, a polymer film was deposited on a silicon substrate over a silicon dioxide layer, and HF was used to etch off the sacrificial layer to release the film.[54]

1.2.10 Plasma etching

A plasma is a gaseous substance, in which a certain portion of the particles are ionized.[55] Plasmas have been referred to as a fourth state of matter. These reactive particles can be used to modify or even etch the surfaces of materials. Plasma etching has been routinely used to clean silicon wafers.[42-43] In my research, I used a Technics Planar Etch II (PE2) oxygen plasma etcher and a Harrick air plasma cleaner, where the PE2 machine is a parallel-plate plasma etcher. It uses highly reactive oxygen radicals and energetic oxygen ions to ash organic residues or contaminants. The Harrick (air) plasma cleaner was used at lower powers to promote hydroxylation of surfaces.

1.2.11 Silicon deep etching

To obtain high aspect ratio silicon nanostructures, silicon deep etching[42, 56] was performed with a Surface Technology Systems (STS) multiplex inductively coupled plasma (ICP) reactive ion etcher (RIE). The RF system in the STS-RIE instrument produces a high-density, low-pressure, low-energy inductively coupled plasma, which can provide directional etching with high chemical sensitivity and high etching rate. A silicon sample with a grid pattern was mounted on a 4" wafer with cooling grease and loaded onto a helium-cooled chuck in the STS-RIE system. Fluorine-based gases, such as SF_6 and C_4F_8, were used for silicon etching. SF_6 provides anisotropic etching, while C_4F_8 protects silicon side walls, fostering isotropic etching. The chamber pressure was controlled at 15 – 25 mTorr. Higher pressures may produce broader features, as more particle collisions will occur on the front silicon surfaces. After etching for 7 min, high aspect ratio, taper shaped, silicon nanostructures were fabricated.

1.3 Experimental materials

In my research projects, carbon nanotubes were investigated because of their outstanding mechanical properties. I also used silicon wafers in many of my projects because they are atomically flat, rather inexpensive, and can be silanized. The following paragraphs briefly introduce these two materials.

1.3.1 Carbon nanotubes

Carbon nanotubes (CNTs), discovered by Iijima in the early 1990s,[57] have played a very important role in nanotechnology. Carbon nanotubes have cylindrical, graphitic structures which are based on a hexagonal, sp^2, arrangement of carbon atoms.[58] Due to their unique structures, carbon nanotubes have many remarkable mechanical and electrical properties.[59] There are two main classes of carbon nanotubes: single-walled nanotubes (SWNTs) and multi-walled nanotubes (MWNTs), where this classification is based on the number of outside graphitic layers they contain.[60] Normally, a SWNT is several micrometers in length and a few nanometers in diameter, which gives it a large surface area with a very high length to diameter ratio.[61]

Carbon nanotubes are one of the strongest of all materials because their skeleton is formed of conjugated sp^2 carbon bonds.[58] Their mechanical properties are usually described by their tensile strength and Young's modulus.[62] The tensile strength is the maximum amount of tensile stress that a material can be subjected to before it breaks. The Young's modulus, which is defined as the ratio of tensile stress to tensile strain, measures the tendency of a material to elastically deform along an axis where opposing forces are applied. SWNTs have about 100 GPa tensile strength and 1 TPa Young's modulus which is fifty and five times higher than steel,

respectively.[61, 63] SWNTs are excellent thermal conductors, having a thermal conductivity along the tube ca. 15 times greater than copper.[64] Based on their structure, carbon nanotubes can be either metallic or semiconducting.[65] Metallic carbon nanotubes can support a very high electrical current density.[66] CNTs also have other properties such as low weight, chemical inertness, and good stability in vacuum, air, and at high temperature that should make them valuable in many applications.[67-68]

I performed several experiments on CNT processing in my research, including CNT sheet (bucky paper) formation, CNT purification, CNT dispersion, and CNT functionalization. More details will be described in Chapters 3 and 6.

1.3.2 Silicon wafers

A polished silicon wafer is an atomically flat, thin slice of a silicon crystal normally with a *ca.* 2 nm thick native oxide layer.[35] Silicon wafers are generally doped with phosphate (n-type) or boron (p-type) in the range of 10^{15} – 10^{20} atoms/cm^3 and cut along a crystallographically important direction, where Si(100) and Si(111) wafers are the most common types sold.[69] In my research, silicon wafers are used in a variety of ways. (1) They can be used as substrates for surface chemical modifications.[70] For example, silicon surfaces can be terminated with hydrogen via HF etching or with hydroxyl groups via piranha cleaning.[71] Organic self-assembled monolayers (SAM) are formed via silanization of hydroxyl terminated silicon surfaces.[36, 72-73] Polymer thin films can be grown on a silicon surface via radical functionalization.[74] Silicon surfaces can be simultaneously modified and patterned with a monolayer by scribing,[75-80] or laser activation in the presence of reactive species.[41, 53, 81] (2) Since polished silicon wafers are flat and smooth, silicon wafers are widely used as substrates for microfabrication, including thin film deposition, lithographic patterning, and etching.[82-84] (3) As silicon wafers are stiff, patterned

silicon wafers can be used as molds or masters in nanoimprint lithography.[85-87] (4) Due to silicon's high melting point, silicon wafers have been used as substrate for carbon nanotube growth, which occurs at over 700°C.[45, 88-89] (5) Silicon is a semiconductor. Hence, doped silicon wafers are used as conductive sample carriers for surface analysis by XPS, SEM, and ToF-SIMS to reduce surface charging. (6) Hydrogen-terminated silicon wafers were used as targets for producing organically modified silicon nanocrystals by laser ablation.[53] (7) Silicon is transparent in the infrared (IR), so thin film materials can be analyzed by IR transmission spectroscopy if double polished silicon wafers are used.[90-92]

1.4 Chemometrics

ToF-SIMS analysis often results in very large data sets with thousands to millions of data points. This wealth of information from spectra and images may create a problem for data analysis, especially when a series of complicated spectra from different materials must be compared. Chemometrics methods,[93-95] which are advanced statistical tools, have been applied to these ToF-SIMS data sets to better extract and identify the chemical information that they contain.[81, 96-98] Several chemometrics methods, including principal components analysis (PCA), cluster analysis, partial least-squares (PLS), and multivariate curve resolution (MCR), will be briefly introduced in the following paragraphs.

1.4.1 Principal components analysis (PCA)

PCA takes into account all of the data in a data set to extract the essential factors that are responsible for the differences among the samples.[93-94, 99-100] Mathematically, each spectrum can be treated as a point in a hyperspace, and PCA can be viewed as simply a rotation of the axes of this coordinate system. The axes of the new coordinate system are called the principal components (PCs). The first principal component (PC1) is the axis that captures the largest

fraction of the variation in the data. PC2 then captures the next largest fraction, and so on. Each PC is associated with sample scores and loadings. Scores are the projections of the samples (spectra) in a data set on a given PC. Samples can be separated into subgroups based on their scores. The loadings of each PC describe the contributions of the original variables (peaks or axes) in the old coordinate system to a PC. PCA is often performed with a cross-validation analysis,[101] which can predict the fit of a hypothetical validation set to a PCA model. The minimum value in the root-mean-square error cross-validation (RMSECV) plot from this cross-validation analysis was used to determine the number of PCs to keep.[102] After a PCA model has been established, the Hotelling T^2 can be used to evaluate the distances within the model of the sample spectra from the origin of the PCA model, and the Q Residuals measures the distances of the sample points (spectra) to the PCA model.[100] A plot of Hotelling T^2 vs. Q Residuals is often used to reveal outliers.[103] Thus, PCA analysis of a ToF-SIMS data set can show the major variation among samples, and the peaks responsible for this variation, and identify outliers.

1.4.2 Cluster analysis

Similar to PCA, cluster analysis[104] can also determine the degree of similarity between samples in a data set. However, one key difference between PCA and cluster analysis is that cluster analysis generally considers all of the variation in a data set, while PCA (at least in its final model) only considers a fraction of it. As a result, cluster analysis is useful as a 'second witness' to PCA. That is, greater confidence is had in a chemometrics analysis of a data set if the same result can be obtained using two or more mathematically different algorithms. The K-means clustering method, a type of hierarchical clustering analysis, is conceptually based on the Euclidean distances between data points (spectra).[105-107] In principle, the two closest points are clustered and replaced by the mean of these two points. The next two closest points are then

identified and replaced by their mean, etc. Through this approach, all of the data points can be clustered into a dendrogram, which is a two-dimensional tree-like plot. In a dendrogram, the length of the horizontal line connecting/between the spectra (points) is inversely proportional to their similarity. Using a dendrogram, it is often possible to visualize sample subgroups.

1.4.3 Partial least-squares (PLS)

PLS[108-109] is a regression method used to find a relationship between two sets of data. This relationship should be a linear model, e.g., $Y = b_0 + b_1X_1 + b_2X_2 + \ldots + b_nX_n$, where Y is the predicted variable that is based on weightings, b_i, of variables X_i. For instance, in my research, a series of coal samples was analyzed by ToF-SIMS. These coal samples were also measured by conventional methods for their heating values, elemental compositions, etc. Therefore, the ToF-SIMS spectra were used as the matrix **X** in the equation above, and other properties of the coal samples served as the matrix **Y**. In PLS, latent variables, similar to principle components in PCA, are used to build a regression model to better explain the relationship between the two matrices. From a cross-validation analysis, the number of latent variables in a model can be determined by the minimum value in the root-mean-square error cross-validation (RMSECV) plot. After a model is created, it can be applied to predict property values from a new set of spectra. More details on PLS analysis of ToF-SIMS spectra of coal samples are given in Chapter 5.

1.4.4 Multivariate curve resolution (MCR)

I also used MCR[110-112] for ToF-SIMS data analysis, especially for ToF-SIMS images with large numbers of data points.[108] MCR is a well-established chemometrics technique, which can be viewed as an extension of classical least squares (CLS).[100] The governing equation of CLS is **S** = **PC**. In this equation, **S** is a matrix containing a series of spectra as columns, which are

believed to be linear combinations of a set of the pure component spectra in the matrix **P**. The **C** matrix gives the contributions of the pure component spectra to the spectra in the **S** matrix. In CLS, **S** and **P** are known, so **C** is obtained by left multiplying both sides of the CLS equation by the pseudoinverse of **P** to give the equation: $\mathbf{C} = (\mathbf{P}^T\mathbf{P})^{-1}\mathbf{P}^T\mathbf{S}$, where $\mathbf{P}^T$ is the transpose of **P** and $(\mathbf{P}^T\mathbf{P})^{-1}$ is the matrix inverse of $\mathbf{P}^T\mathbf{P}$. MCR differs from CLS in that only the matrix S is known. The CLS equation is therefore solved in two ways to obtain:

$$\mathbf{C} = (\mathbf{P}^T\mathbf{P})^{-1}\mathbf{P}^T\mathbf{S} \tag{1.5}$$

$$\mathbf{P} = \mathbf{S}\mathbf{C}^T (\mathbf{C}\mathbf{C}^T)^{-1} \tag{1.6}$$

A guess for **P** is then entered into equation (1.5). The calculated **C** values are next entered into equation (1.6). During the repeated iterations of the equations above, the elements of the **P** and **C** matrices are subject to a nonnegativity constraint, and convergence of the **P** and **C** matrices may occur. More details about MCR analysis of ToF-SIMS spectra are given as this method is applied to LAMSS spots in Chapter 4.[81]

1.5 Contents of this Dissertation

In this dissertation, five projects are covered in detail. Chapter 2 describes the fabrication of transparent polymer templates for nanostructured amorphous silicon photovoltaics using low-cost nanoimprint lithography of polydimethylsiloxane. This approach provides a test bed for absorption studies in nanostructured film geometries and should result in improved light capturing designs in thin-film solar cells. Nanopatterned polymer films were characterized by scanning electron microscopy and optical measurements. Chapter 3 describes a straightforward method for fabricating freely suspended, thin, carbon nanotube membranes infiltrated with polymers. This process is a new approach for making thin, reinforced, smooth films or

membranes with high concentrations of CNTs, which may lead to higher performance materials. Characterization of the films and membranes was performed via scanning electron microscopy and atomic force microscopy. Chapter 4 reports laser activation-modification of semiconductor surfaces (LAMSS) on silicon with a series of 1-alkenes. A key finding from this study is that the degree of surface functionalization in a LAMSS spot appears to decrease radially from the center of the spot. These laser spots were studied by time-of-flight secondary ion mass spectrometry (ToF-SIMS), and the resulting spectra were analyzed using a series of chemometrics methods. In chapter 5, a large ToF-SIMS data set from multiple coal samples spanning a wide range of coal properties was subjected to a chemometrics analysis. This analysis separates the spectra into clusters that correspond to measurements from classical combustion analyses. Thus ToF-SIMS appears to be a promising technique for analysis of this important fuel. Several experiments on carbon nanotube processing will be described in chapter 6, including carbon nanotube sheet formation, carbon nanotube purification, carbon nanotube dispersion, and carbon nanotube functionalization. X-ray photoelectron spectroscopy was a key characterization tool for many of these experiments. Chapter 7 provides future directions for these projects.

1.6 References

1. Siegbahn, K., Electron-Spectroscopy for Atoms, Molecules, and Condensed Matter. *Science* **1982,** *217* (4555), 111-115.

2. Skoog, D. A.; Holler, F. J.; Nieman, T. A., *Principles of instrumental analysis*. 5th ed.; Harcourt Brace College Publishers: Philadelphia, 1998.

3. Nefedov, V. I., *X-ray photoelectron spectroscopy of solid surfaces*. VSP: Utrecht, 1988.

4. Sodhi, R. N. S., Time-of-flight secondary ion mass spectrometry (TOF-SIMS): versatility in chemical and imaging surface analysis. *Analyst* **2004,** *129* (6), 483-487.

5. Vickerman, J. C.; Briggs, D., *ToF-SIMS : surface analysis by mass spectrometry*. IM: Chichester, 2001.

6. Veeco Dimension 3100 Atomic Force Microscope Users Manual.

7. Gabriel, B. L., *SEM : a user's manual for materials science*. American Society for Metals: Metals Park, Ohio, 1985.

8. Egerton, R. F., *Physical principles of electron microscopy : an introduction to TEM, SEM, and AEM*. Springer Science Business Media: New York, 2005.

9. Tompkins, H. G.; Irene, E. A., *Handbook of ellipsometry*. William Andrew Pub. ;Springer: Norwich, NY Heidelberg, Germany, 2005.

10. Fujiwara, H., *Spectroscopic ellipsometry : principles and applications*. John Wiley: Chichester, 2007.

11. Mittal, K. L., *Contact angle, wettability and adhesion*. VSP: Utrecht ; Boston, 2003.

12. Serway, R. A., *Physics for scientists & engineers*. 2nd ed.; Saunders College Pub.: Philadelphia, 1987.

13. Briggs, D.; Seah, M. P., *Practical surface analysis*. 2nd ed. ed.; Wiley: 1990.

14. Gross, J. H., *Mass spectrometry : a textbook*. Springer: Berlin ; London, 2004.

15. Swanson, L. W., Liquid-Metal Ion Sources - Mechanism and Applications. *Nucl Instrum Methods* **1983,** *218* (1-3), 347-353.

16. Magonov, S. N.; Whangbo, M.-H., *Surface analysis with STM and AFM : experimental and theoretical aspects of image analysis*. VCH: Weinheim ; Cambridge, 1996.

17. Giessibl, F. J., Advances in atomic force microscopy. *Rev. Mod. Phys.* **2003,** *75* (3), 949-983.

18. Zhong, Q.; Inniss, D.; Kjoller, K.; Elings, V. B., Fractured Polymer Silica Fiber Surface Studied by Tapping Mode Atomic-Force Microscopy. *Surf. Sci.* **1993,** *290* (1-2), L688-L692.

19. Han, J. Q.; Li, X. X.; Bao, H. F.; Zuo, G. M.; Wang, Y. L.; Feng, F.; Yu, Z. Y.; Ge, X. H., AFM probes fabricated with masked-maskless combined anisotropic etching and p(+) surface doping. *J. Micromech. Microeng.* **2006,** *16* (2), 198-204.

20. Albrecht, T. R.; Akamine, S.; Carver, T. E.; Quate, C. F., Microfabrication of Cantilever Styli for the Atomic Force Microscope. *J. Vac. Sci. Technol. A* **1990,** *8* (4), 3386-3396.

21. Boisen, A.; Hansen, O.; Bouwstra, S., AFM probes with directly fabricated tips. *J Micromech. Microeng.* **1996,** *6* (1), 58-62.

22. Krinsley, D. H., *Backscattered scanning electron microscopy and image analysis of sediments and sedimentary rocks*. Cambridge University Press: Cambridge, U.K. ; New York, 1998.

23. Goldstein, J., *Scanning electron microscopy and x-ray microanalysis*. 3rd ed.; Kluwer Academic/Plenum Publishers: New York, 2003.

24. Orloff, J.; Utlaut, M. W.; Swanson, L., *High resolution focused ion beams : FIB and its applications : the physics of liquid metal ion sources and ion optics and their application to focused ion beam technology*. Kluwer Academic/Plenum: New York ; London, 2003.

25. Williams, D. B.; Carter, C. B., *Transmission electron microscopy: a textbook for materials science*. Plenum: New York; London, 1996.

26. J.A. Woollam, Inc., Variable angle spectroscopic ellipsometer user manual.

27. Azzam, R. M. A.; Bashara, N. M., *Ellipsometry and polarized light*. North-Holland Pub. Co. ; sole distributors for the U.S.A. and Canada, Elsevier North-Holland: Amsterdam; New York, 1977.

28. Pei, L.; Balls, A.; Tippets, C.; Abbott, J.; Linford, M. R.; Hu, J.; Madan, A.; Allred, D. D.; Vanfleet, R. R.; Davis, R. C., Polymer Molded Templates for Nanostructured Amorphous Silicon Photovoltaics. *J. Vac. Sci. Technol. A* **2011**, in press.

29. Sphere Optics Technical Publications - Integrating Sphere Design and Applications.

30. Grossweiner, L. I.; Rogers, B. H. G.; Grossweiner, J. B.; Jones, L. R.; SpringerLink (Online service), The Science of Phototherapy: An Introduction. Springer: Dordrecht, 2005.

31. Acharya, T.; Ray, A. K., *Image processing: principles and applications*. Wiley-Interscience; [Chichester: John Wiley, distributor]: Hoboken, N.J., 2005.

32. Van Zant, P., *Microchip fabrication: a practical guide to semiconductor processing*. 5th ed. ed.; McGraw-Hill: New York; London, 2004.

33. Holm, R., *Electric contacts: theory and application*. 4th ed. ed.; Springer: Berlin, 1967.

34. Schubert, D. W.; Dunkel, T., Spin coating from a molecular point of view: its concentration regimes, influence of molar mass and distribution. *Mater. Res. Innovations* **2003,** *7* (5), 314-321.

35. Sze, S. M., *Semiconductor devices, physics and technology*. Wiley: New York, 1985.

36. Zhang, F.; Sautter, K.; Larsen, A. M.; Findley, D. A.; Davis, R. C.; Samha, H.; Linford, M. R., Chemical Vapor Deposition of Three Aminosilancs on Silicon Dioxide: Surface Characterization, Stability, Effects of Silane Concentration, and Cyanine Dye Adsorption. *Langmuir* **2010,** *26* (18), 14648-14654.

37. Jaeger, R. C., *Introduction to microelectronic fabrication*. 2nd ed. ed.; Prentice Hall; London: Pearson Education: Upper Saddle River. N.J., 2002.

38. Rai-Choudhury, P., *Handbook of microlithography, micromachining, and microfabrication*. SPIE Optical Engineering Press; London: Institution of Electrical Engineers: Bellingham, Wash., 1997.

39. Costner, E. A.; Lin, M. W.; Jen, W. L.; Willson, C. G., Nanoimprint Lithography Materials Development for Semiconductor Device Fabrication. *Annu. Rev. Mater. Res.* **2009,** *39*, 155-180.

40. Guo, L. J., Nanoimprint lithography: Methods and material requirements. *Adv. Mater. (Weinheim, Ger.)* **2007,** *19* (4), 495-513.

41. Zhang, F.; Pei, L.; Bennion, E.; Jiang, G. L.; Connley, D.; Yang, L.; Lee, M. V.; Davis, R. C.; Smentkowski, V. S.; Strossman, G.; Linford, M. R.; Asplund, M. C., Laser activation modification of semiconductor surfaces (LAMSS). *Langmuir* **2006,** *22* (26), 10859-10863.

42. Liu, C. P. D., *Foundations of MEMS*. Prentice Hall: Upper Saddle River, N.J.; London, 2006.

43. Sugawara, M., *Plasma etching : fundamentals and applications*. Oxford University Press: Oxford, 1998.

44. May, G. S.; Spanos, C. J., *Fundamentals of semiconductor manufacturing and process control*. IEEE Wiley-Interscience, Chichester : John Wiley [distributor]: Hoboken, N.J., 2006.

45. Hutchison, D. N.; Morrill, N. B.; Aten, Q.; Turner, B. W.; Jensen, B. D.; Howell, L. L.; Vanfleet, R. R.; Davis, R. C., Carbon Nanotubes as a Framework for High-Aspect-Ratio MEMS Fabrication. *J. Microelectromech. S* **2010,** *19* (1), 75-82.

46. Newbury, D. E., *Advanced scanning electron microscopy and X-ray microanalysis*. Plenum Press: New York, 1986.

47. Dini, J. W., *Electrodeposition: the materials science of coatings and substrates*. Noyes Publications: Park Ridge, N.J., 1993.

48. Krongauz, V. V.; Trifunac, A. D., *Processes in photoreactive polymers*. Chapman & Hall: New York, 1995.

49. Kemme, S. A., Microoptics and nanooptics fabrication. CRC Press: Boca Raton, 2010.

50. Odom, T. W.; Love, J. C.; Wolfe, D. B.; Paul, K. E.; Whitesides, G. M., Improved pattern transfer in soft lithography using composite stamps. *Langmuir* **2002,** *18* (13), 5314-5320.

51. Narasimhan, B.; Mallapragada, S.; Porter, M. D., *Combinatorial materials science*. Wiley-Interscience: Hoboken, N.J., 2007.

52. Kern, W.; Knovel (Firm), Handbook of semiconductor wafer cleaning technology science, technology, and applications. In *Materials science and process technology series. Electronic materials and process technology* [Online] Noyes Publications: Park Ridge, N.J., U.S.A., 1993.

53. Shirahata, N.; Linford, M. R.; Furumi, S.; Pei, L.; Sakka, Y.; Gates, R. J.; Asplund, M. C., Laser-derived one-pot synthesis of silicon nanocrystals terminated with organic monolayers. *Chem. Commun. (Cambridge, U. K.)* **2009,** (31), 4684-4686.

54. Buhler, J.; Steiner, F. P.; Baltes, H., Silicon dioxide sacrificial layer etching in surface micromachining. *J. Micromech. Microeng.* **1997,** *7* (1), R1-R13.

55. Fridman, A., *Plasma Chemistry*. Cambridge University Press: 2008.

56. Cui, Z., *Micro-nanofabrication: technologies and applications*. Higher Education Press: 2005.

57. Iijima, S., Helical microtubules of graphitic carbon. *Nature* **1991,** *354*, 56-58.

58. Saito, R.; Dresselhaus, G.; Dresselhaus, M. S., *Physical properties of carbon nanotubes*. Imperial College Press: 1998.

59. Marulanda, J. M., *Current Transport Modeling of Carbon Nanotubes*. VDM Verlag: 2009.

60. Merkoçi, A., Carbon Nanotubes in Analytical Sciences. *Microchim. Acta* **2006,** *152* (3), 157-174.

61. Treacy, M. M. J.; Ebbesen, T. W.; Gibson, J. M., Exceptionally high Young's modulus observed for individual carbon nanotubes *Nature* **1996,** *381*, 678-680.

62. Liu, C., *Foundations of MEMS*. Prentice Hall 2005.

63. Qian, D.; Wagner, G. J.; Liu, W. K.; Yu, M.-F.; Ruoff, R. S., Mechanics of carbon nanotubes. *Appl. Mech. Rev.* **2002,** *55*, 495-533.

64. Berber, S.; Kwon, Y.-K.; Tománek, D., Unusually High Thermal Conductivity of Carbon Nanotubes. *Phys. Rev. Lett.* **2000,** *84*, 4613-4616.

65. Chen, C.; Zhang, Y., *Nanowelded Carbon Nanotubes: From Field-Effect Transistors to Solar Microcells*. Springer: 2009.

66. Collins, P. G.; Avouris, P., Nanotubes for Electronics. *Scientific American* **2000,** *December*, 68.

67. Jorio, A.; Dresselhaus, G.; Dresselhaus, M. S., *Carbon nanotubes: advanced topics in the synthesis, structure, properties and applications*. Springer: 2008.

68. Meyyappan, M., *Carbon nanotubes: science and applications*. CRC Press: 2005.

69. Taur, Y.; Ning, T. H., *Fundamentals of modern VLSI devices*. Cambridge University Press: Cambrige, UK; New York, 1998.

70. Bhushan, B., *Springer handbook of nanotechnology*. 2nd rev. & extended ed.; Springer: Berlin; New York, 2007.

71. O'Mara, W. C.; Herring, R. B.; Hunt, L. P., *Handbook of semiconductor silicon technology*. Noyes Publications: 1990.

72. Tjong, S. C., *Nanocrystalline materials: their synthesis-structure-property relationships and applications*. Elsevier: 2006.

73. Jones, R. G.; Wataru, A.; Chojnowski, J., *Silicon-Containing Polymers: The Science and Technology of Their Synthesis and Applications*. Springer: 2001.

74. Blake, R. B.; Pei, L.; Yang, L.; Lee, M. V.; Conley, H. J.; Davis, R. C.; Shirahata, N.; Linford, M. R., One-step growth of ca. 2-15 nm polymer thin films on hydrogen-terminated silicon. *Macromol. Rapid Commun.* **2008,** *29* (8), 638-644.

75. Lee, M. V.; Lee, J. R. I.; Brehmer, D. E.; Linford, M. R.; Willey, T. M., Unanticipated C = C Bonds in Covalent Monolayers on Silicon Revealed by NEXAFS. *Langmuir* **2010,** *26* (3), 1512-1515.

76. Lee, M. V.; Nelson, K. A.; Hutchins, L.; Becerril, H. A.; Cosby, S. T.; Blood, J. C.; Wheeler, D. R.; Davis, R. C.; Woolley, A. T.; Harb, J. N.; Linford, M. R., Nanografting of silanes on silicon dioxide with applications to DNA localization and copper electroless deposition. *Chem. Mater.* **2007,** *19* (21), 5052-5054.

77. Lee, M. V.; Hoffman, M. T.; Barnett, K.; Geiss, J. M.; Smentkowski, V. S.; Linford, M. R.; Davis, R. C., Chemomechanical nanolithography: Nanografting on silicon and factors impacting linewidth. *J. Nanosci. Nanotechnol.* **2006,** *6* (6), 1639-1643.

78. Yang, L.; Lua, Y. Y.; Lee, M. V.; Linford, M. R., Chemomechanical functionalization and patterning of silicon. *Acc. Chem. Res.* **2005,** *38* (12), 933-942.

79. Lua, Y. Y.; Fillmore, W. J. J.; Yang, L.; Lee, M. V.; Savage, P. B.; Asplund, M. C.; Linford, M. R., First reaction of a bare silicon surface with acid chlorides and a one-step preparation of acid chloride terminated monolayers on scribed silicon. *Langmuir* **2005,** *21* (6), 2093-2097.

80. Lua, Y. Y.; Lee, M. V.; Fillmore, W. J. J.; Matheson, R.; Sathyapalan, A.; Asplund, M. C.; Fleming, S. A.; Linford, M. R., Amine-reactive monolayers on scribed silicon with controlled levels of functionality: Reaction of a bare silicon surface with mono- and diepoxides. *Angew. Chem. Int. Edit.* **2003,** *42* (34), 4046-4049.

81. Pei, L.; Jiang, G. L.; Davis, R. C.; Shaver, J. M.; Smentkowski, V. S.; Asplund, M. C.; Linford, M. R., Laser activation-modification of semiconductor surfaces (LAMSS) of 1-alkenes on silicon: A ToF-SIMS, chemometrics, and AFM analysis. *Appl. Surf. Sci.* **2007,** *253* (12), 5375-5386.

82. Franssila, S., *Introduction to Microfabrication*. John Wiley & Sons: 2010.

83. Hesketh, P. J.; Society, E.; Meeting, E. S., *Microfabricated Systems and MEMS VI: proceedings of the international symposium*. Electrochemical Society, Inc.: 2002.

84. Jackson, M. J., *Microfabrication and nanomanufacturing*. CRC/Taylor & Francis: 2006.

85. Matsui, J.; Takahashi, H.; Xie, N.; Mizuno, J.; Utaka, K. In *Fabrication of silicon mold for thermal Nanoimprint Lithography*, Nano-Optoelectronics Workshop, 2008. i-NOW 2008. International, 2-15 Aug. 2008; 2008; pp 267-268.

86. Bruinink, C. M.; Burresi, M.; de Boer, M. J.; Segerink, F. B.; Jansen, H. V.; Berenschot, E.; Reinhoudt, D. N.; Huskens, J.; Kuipers, L., Nanoimprint Lithography for Nanophotonics in Silicon. *Nano Lett.* **2008,** *8* (9), 2872-2877.

87. Buyukserin, F.; Aryal, M.; Gao, J.; Hu, W., Fabrication of Polymeric Nanorods Using Bilayer Nanoimprint Lithography. *Small* **2009,** *5* (14), 1632-1636.

88. Wang, Z. L.; Liu, Y.; Zhang, Z., *Handbook of Nanophase and Nanostructured Materials: Materials systems and applications II*. Kluwer Academic/Plenum: 2003.

89. Kumar, C. S. S. R.; Hormes, J.; Leuschner, C., *Nanofabrication towards biomedical applications: techniques, tools, applications, and impact*. Wiley-VCH: 2005.

90. Luo, H.; Chemistry, S. U. D. o., *Silicon surface chemistry studied by infrared spectroscopy*. Stanford University: 1998.

91. Prokhorov, Y. I.; Sologub, V. A.; Sukhodaev, B. A., The infrared transmission and reflectance spectra of silicon nitride films obtained in a high-frequency discharge plasma. *Journal of Applied Spectroscopy* **1973,** *19* (3), 1211-1213.

92. Gamsky, C. J.; Howes, G. R.; Taylor, J. W., Infrared Reflection Absorption Spectroscopy of Photoresist Films on Silicon Wafers: Measuring Film Thickness and Removing Interference Fringes. *Anal. Chem.* **1994,** *66* (7), 1015-1020.

93. Brereton, R. G., *Chemometrics: data analysis for the laboratory and chemical plant*. Wiley: Chichester, 2003.

94. Kramer, R., *Chemometric techniques for quantitative analysis*. Marcel Dekker: New York, 1998.

95. Beebe, K. R.; Pell, R. J.; Seasholtz, M. B., *Chemometrics: a practical guide*. Wiley: New York ; Chichester, 1998.

96. Yang, L.; Shirahata, N.; Saini, G.; Zhang, F.; Pei, L.; Asplund, M. C.; Kurth, D. G.; Ariga, K.; Sautter, K.; Nakanishi, T.; Smentkowski, V.; Linford, M. R., Effect of Surface Free Energy on PDMS Transfer in Microcontact Printing and Its Application to ToF-SIMS to Probe Surface Energies. *Langmuir* **2009,** *25* (10), 5674-5683.

97. Yang, L.; Lua, Y. Y.; Jiang, G. L.; Tyler, B. J.; Linford, M. R., Multivariate analysis of TOF-SIMS spectra of monolayers on scribed silicon. *Anal. Chem.* **2005,** *77* (14), 4654-4661.

98. Pei, L.; Jiang, G.; Tyler, B. J.; Baxter, L. L.; Linford, M. R., Time-of-flight secondary ion mass spectrometry of a range of coal samples: A chemometrics (PCA, cluster, and PLS) analysis. *Energy Fuels* **2008,** *22* (2), 1059-1072.

99. Jolliffe, I. T., *Principal component analysis*. Springer-Verlag: New York, 1986.

100. Jackson, J. E., *A user's guide to principal components*. Wiley: 1991.

101. Martens, H.; Martens, M., *Multivariate analysis of quality: an introduction*. Wiley: Chichester, 2001.

102. Smilde, A. K.; Bro, R.; Geladi, P., *Multi-way analysis with applications in the chemical sciences*. J. Wiley: 2004.

103. Lillhonga, T.; Geladi, P., Replicate analysis and outlier detection in multivariate NIR calibration, illustrated with biofuel analysis. *Anal. Chim. Acta* **2005,** *544* (1-2), 177-183.

104. Aldenderfer, M. S.; Blashfield, R. K., *Cluster analysis*. Sage Publications: Beverly Hills, 1984.

105. Otto, M., *Chemometrics: statistics and computer application in analytical chemistry*. 2nd rev. ed. ed.; Wiley-VCH ; Chichester : John Wiley [distributor]: Weinheim, 2007.

106. Hung, M. C.; Wu, J. P.; Chang, J. H.; Yang, D. L., An efficient k-means clustering algorithm using simple partitioning. *J. Inf. Sci. Eng.* **2005,** *21* (6), 1157-1177.

107. Kanungo, T.; Mount, D. M.; Netanyahu, N. S.; Piatko, C. D.; Silverman, R.; Wu, A. Y., An efficient k-means clustering algorithm: Analysis and implementation. *Ieee T Pattern Anal.* **2002,** *24* (7), 881-892.

108. Vickerman, J. C.; Gilmore, I. S., *Surface analysis: the principal techniques*. 2nd ed.; Wiley: Chichester, 2009.

109. Esposito Vinzi, V., *Handbook of partial least squares: concepts, methods and applications*. Springer: Berlin ; London, 2010.

110. Keenan, M. R.; Kotula, P. G., Optimal scaling of TOF-SIMS spectrum-images prior to multivariate statistical analysis. *Appl. Surf. Sci.* **2004,** *231-2*, 240-244.

111. Ohlhausen, J. A. T.; Keenan, M. R.; Kotula, P. G.; Peebles, D. E., Multivariate statistical analysis of time-of-flight secondary ion mass spectrometry images using AXSIA. *Appl. Surf. Sci.* **2004,** *231-2*, 230-234.

112. Smentkowski, V. S.; Ohlhausen, J. A.; Kotula, P. G.; Keenan, M. R., Multivariate statistical analysis of time-of-flight secondary ion mass spectrometry images-looking beyond the obvious. *Appl. Surf. Sci.* **2004,** *231-2*, 245-249.

Chapter 2 Polymer Molded Templates for Nanostructured Amorphous Silicon Photovoltaics

2.1 Abstract

Here I report the fabrication of transparent polymer templates for nanostructured amorphous silicon photovoltaics using low cost nanoimprint lithography of polydimethylsiloxane. The template contains a square two-dimensional array of high-aspect-ratio nanoholes (300 nm diameter by 1 μm deep holes) on a 500×500 nm^2 pitch. A 100 nm thick layer of a-Si:H was deposited on the template surface resulting in a periodically nanostructured film. The optical characterization of the nanopatterned film showed lower light transmission at 600–850 nm wavelengths and lower light reflection at 400–650 nm wavelengths, resulting in 20% higher optical absorbance at AM 1.5 spectral irradiance versus a nonpatterned film.

2.2 Introduction

Compared to crystalline silicon based solar cells,[1-3] thin-film hydrogenated amorphous silicon (a-Si:H) solar cells[4-6] have the potential advantages of less raw material usage and lower fabrication costs as well as the benefits of high flexibility and light weight.[7] However, the efficiency of single-layer, thin-film a-Si:H solar cells is relatively low. Several efforts have been made to increase single-layer cell efficiency by improving the light trapping of devices.[8-25]

To achieve efficient light trapping, researchers have developed a number of scattering techniques. These include randomly textured substrates, such as Asahi – U type glass[23] and other high-haze transparent conductive oxide material coatings[21] which scatter light at their rough interfaces. The scattered light increases the effective optical path length for internally diffused light rays, which widens the absorption window towards long light wavelength. Metal nanoparticles[9, 26] have also been incorporated into photovoltaic (PV) systems as plasmonic

structures for light scattering and for exciting near-field charge carriers, and coupling light into guided modes. These techniques have been applied either on the front or rear of the solar cell.[11, 14] Periodically nanostructured plasmonic back contacts have been reported to improve short-circuit current densities in the spectral range from 550 nm to 800 nm. These demonstrated light trapping, enhanced beyond that of a randomly textured cell.[13] Another surface-texture geometry that has resulted in increased efficiencies is the nanodome solar cell device with significant higher absorption than flat solar cell.[25] Sub-wavelength gratings (SWGs), which have consisted of a one dimensional array of lines with pitch smaller than the light wavelength, have been used to suppress reflection over wide spectral bandwidth and large field of view.[18, 27] In photovoltaic applications,[9-10, 16, 24, 28-29] for example, periodically structured ZnO:Al front contacts[10] have been implemented in amorphous silicon thin-film solar cells to reduce reflectance and increase current density.

To directly measure light absorption in periodic nanopatterned a-Si:H films, I designed and fabricated a polymer template with a square two-dimensional array of high aspect-ratio nanoholes (300 nm diameter by 1 μm deep holes) on a 500×500 nm^2 pitch. A 100 nm thick layer of a-Si:H was deposited on the template surface, resulting in a periodically nanostructured film, and on planar surfaces for comparison. Optical reflection and transmission measurements were then conducted with an integrating sphere to capture both specular and scattered light. In order to measure the effect of nanoscale structuring on absorption of the amorphous silicon without absorption contributions by other adjacent materials, a simplified sample was fabricated without any metal back reflector or electrode coating.

Besides the analysis of optical absorption, several other aspects have been considered in this nanostructure design. (1) The template can be cost-effectively incorporated into a single

junction thin-film PV device using conventional PV film deposition techniques. (2) Fast, scalable production of the template using roll-to-roll techniques[30] can be applied on inexpensive polymer substrates. (3) The patterned photovoltaic approach, when implemented at the appropriate dimensions, could have an impact on using PV materials characterized by high defect densities including organic, quantum dot, and oxide PV systems.[31-33]

2.3 Experimental

The fabrication process for our three-dimensional nanostructured polymer template has two main steps: silicon master fabrication and nanoembossing. A reusable silicon master was first produced with a nanopillar array. This silicon master was used as a mold to emboss on a polymer film via nanoimprint lithography. This is a technique for high throughput patterning of polymer nanostructures at great precision and at low costs.[34-35] The process diagram is shown in Figure 2.1.

2.3.1 Electron-beam lithography

ZEP 520A e-beam resist (Nippon Zeon) was spin coated on a silicon wafer and baked on a hotplate at 170 °C for 2 min. ZEP has high sensitivity which is particularly valuable for large area patterning, and has relatively high plasma etch resistance. To reduce resist charging during exposure, a layer of conductive polymer was also spin coated on top of the ZEP layer and baked on a hotplate at 90 °C for 30 s. The designed pattern was a square about 5×5 mm^2. This pattern contains an 18 × 18 array of 300 × 300 μm^2 squares with a 5 μm overlap of the squares on each side. The 300 μm squares are made of a series of perpendicularly crossed lines with 500 nm pitch to form a grid pattern. An FEI/Philips XL30 FEG ESEM (operating in high vacuum mode) with a Nanometer Pattern Generation System (JC Nabity Lithography Systems) was used for electron beam exposure. The electron beam was set at 30 kV, and the spot set to size 5 (1172 pA)

to allow fast writing. The magnification was 200× and the exposure line dose was 0.867 nC/cm. The exposed ZEP sample was first rinsed with DI water to remove the conductive polymer, followed by development in ZED-N50 developer, rinsing in ZMD-D, and again rinsing in DI water. Finally the sample was put into an oxygen plasma etcher (Technics Planar-Etch II) at 100 W for 1 min to descum the resist pattern.

2.3.2 Silicon master etching

After descumming, the sample was then loaded into STS Multiplex ICP-RIE with SF_6 and C_4F_8 flow for directional etching. The exposed regions of the silicon surface were etched down 1 μm. After etching, the sample was put into the PE2 oxygen plasma etcher to remove most of the e-beam resist. The sample was then treated in piranha solution to thoroughly clean and to add hydroxyl groups on the surface. More details on plasma treatment are described in Appendix 3.

2.3.3 Anti-adhesion coating deposition

A perfluorosilane anti-adhesion coating layer was deposited on the surface of the silicon master via the following steps. The silicon master was put into a desiccator. A drop or two of trichloro(1H,1H,2H,2H-perfluorooctyl)silane (448931, Sigma-Aldrich) were deposited in two scintillation vials which were placed beside the master. The desiccator chamber was pumped down with the lab vacuum for 10 min to accelerate the silane vaporization. Finally, the desiccator was sealed overnight to allow sufficient deposition on the high-aspect-ratio pattern. This perfluorosilane anti-adhesion coating had an advancing water contact angle over 118°, which helps the silicon master separate from imprinted polymer at the end of the nanoimprint process. Figure 2.2 shows the resulting silicon nanopillar array master.

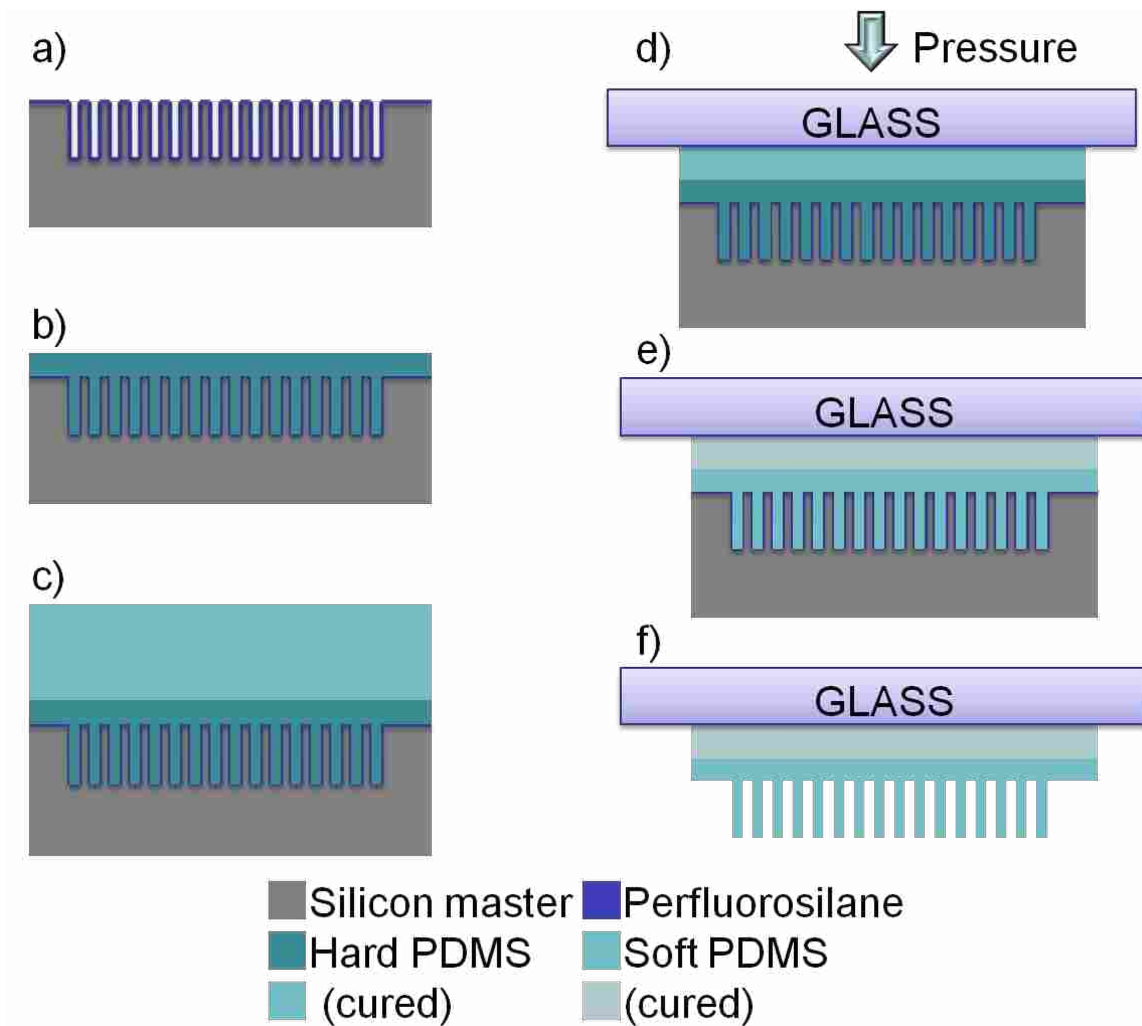

Figure 2.1. Schematic of the nanoimprint process: (a) silicon master coated with a perfluorosilane; (b) spin coating hard PDMS; (c) pouring soft PDMS on top of the hard PDMS; (d) placement of a glass slide; (e) curing the PDMS stack; and (f) releasing the silicon master.

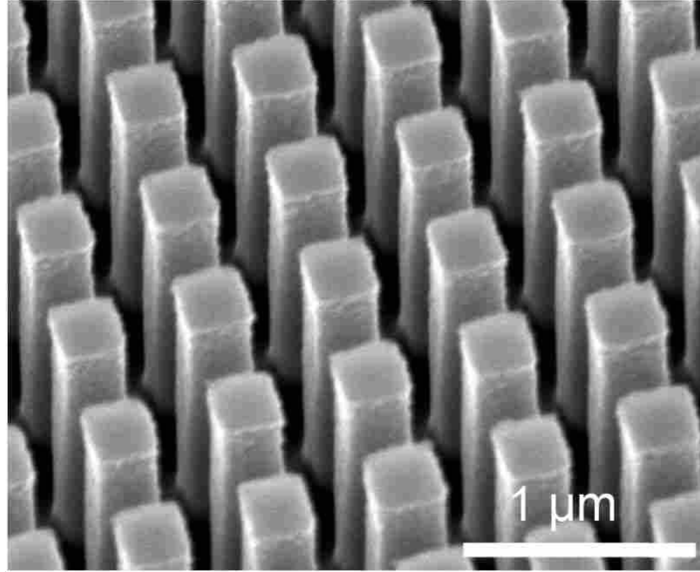

Figure 2.2. SEM image of the patterned silicon wafer with nanopillar array.

2.3.4 Nanoimprint patterning of the polymer

Polydimethylsiloxane (PDMS) was used for the patterned polymer template. PDMS has the advantages of: (1) low cost, (2) optical transparency, and (3) thermal stability (well over the temperature of 200˚C required for the silicon layer deposition). Both hard PDMS and soft PDMS were employed in the process. The hard PDMS has a higher modulus of elasticity and is used to replicate the high-resolution high-aspect ratio template features. Soft PDMS was used as a glue to attach the hard PDMS to a glass slide.

To prepare hard PDMS, 3.4 g of a vinyl PDMS prepolymer (VDT-731, Gelest.), 18 µL of a Pt catalyst (platinum divinyltetramethyldisiloxane, SIP6831.1, Gelest), and one drop of a modulator (2,4,6,8-tetramethyl-tetravinylcyclotetrasiloxane, 87927, Sigma-Aldrich) were mixed and degassed for 15 min in a vacuum desiccator. 1 g of a hydrosilane prepolymer (HMS-301, Gelest) was then gently stirred into this mixture and degassed for another 2 min. Immediately (within 3 min), this hard PDMS mixture was spin-coated onto the silicon master at 1000 rpm for 40 s, forming a 30 to 40 µm thick layer. Hard PDMS thus fully covered the nanopillars on the silicon master. The coated master was then put into an oven and partially cured for 30 min at 60 °C.

The soft PDMS pre-polymer Sylgard 184 PDMS (Dow Corning) base and curing agent were mixed 10:1 and degassed for 30 min ahead of time. This liquid pre-polymer was poured onto the hard PDMS layer immediately after the partial curing, while the hard PDMS was still slightly tacky. The partially completed structure was then degassed in a vacuum desiccator for one h. After a glass slide was placed on the soft PDMS and a 530 g weight was placed on the glass slide (Figure 2.1), the structure was returned to the vacuum for further degassing to remove

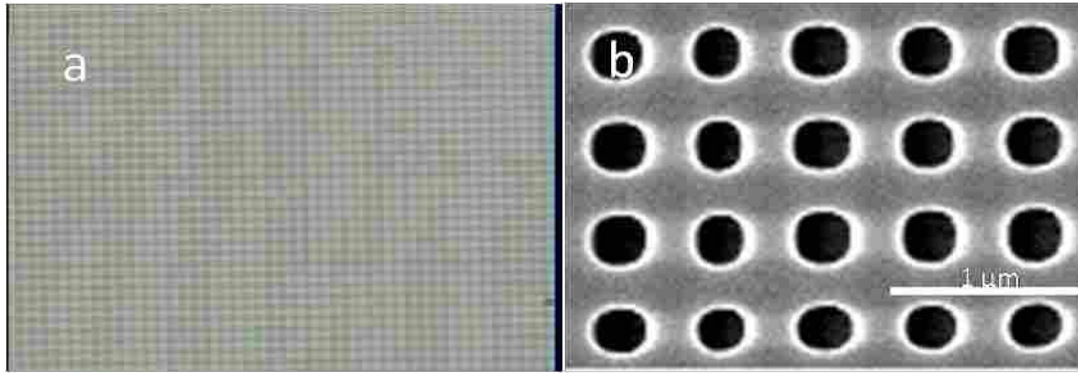

Figure 2.3. (a) Optical and (b) SEM images of embossed nano-holes.

any bubbles between the soft PDMS and the glass. The PDMS stack was slowly cured at room temperature (overnight, 12-14 h). Fast curing at high temperature can cause the hard PDMS to crack. After this slow curing, the entire assembly was placed in an oven at 60 °C for a 1 h hard bake. The composite PDMS template was then released from the master surface by carefully peeling the template from the surface while it was still warm. Figure 2.3 shows the optical and SEM images of the imprinted nanoholes, which are the inverse of the silicon master pattern. Other polymers have also been tested as a template material, which are described in Appendix 2.

2.3.5 Photovoltaic material deposition

Patterned and unpatterned PDMS layer regions on a glass slide were simultaneously coated with 100 nm amorphous silicon by plasma enhanced chemical vapor deposition (PECVD). The deposition was done in an MVSystems PECVD reactor (MVSystems) at 200 °C from pure silane gas. The amorphous silicon produced in this study results in a typical hydrogen concentration of ~10%; the optical bandgap is 1.7-1.8 eV. For planar amorphous silicon layers of 100 nm thickness, the largest gain in absorption is in the wavelength range of 400~540 nm as the absorption coefficient of the material becomes > 1E5/cm in this wavelength range. For sample description, the area outside the nanostructured region is labeled “planar” sample, while the area inside the nanostructured template is labeled as a “patterned” sample. Both samples consisted of a glass/PDMS/a-Si:H stack. The 100 nm layer thickness was chosen because in amorphous silicon devices the Staebler-Wronski degradation limits the active layer thickness for highly efficient carrier extraction to approximately 100 nm.[36] At this thickness, however, planar layers capture little of the light at wavelengths above 600 nm. Figure 2.4a shows an SEM front view of the patterned sample. The diameter of the nanoholes was reduced by around 100 nm on the surface by the amorphous silicon deposition. In the cross-section image (Figure 2.4b) processed

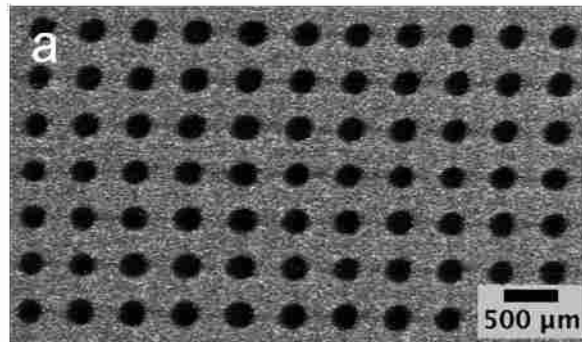

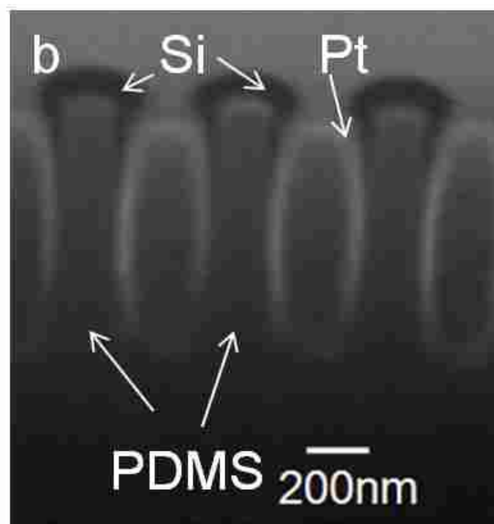

Figure 2.4. (a) SEM top view of an a-Si coated, patterned polymer template, and (b) cross-section view showing (starting from the top of a post and moving down) Pt (FIB deposited), a-Si (dark cap), and PDMS posts.

by focused ion beam (FIB), 100 nm of amorphous silicon (which shows up as black) can be seen deposited mostly at the top of the posts with the coating continuing down the posts approximately 150 nm. An experiment was also performed to deposit aluminum as an electrode layer onto a PDMS template, which is described in Appendices 1 and 3.

2.3.6 Optical measurement setup

Reflectance and transmission as a function of wavelength were measured on both patterned and planar samples. A tungsten lamp was used as the light source. The light beam was collimated with a lens tube. Then the light passed through an aperture to reduce the beam diameter to approximately 3 mm, which is small enough to easily align with the 5×5 mm^2 nanopatterned area. A two-inch diameter integrating sphere with a 99% reflectance coating (Thorlabs, IS236A-4) was used for transmission, reflection, and incident beam intensity measurements. A Czerny-Turner CCD spectrometer (Science-Surplus, Compact Fiber Coupled CCD Spectrometer, 365 - 1100 nm) was fiber coupled to the detector port of the integrating sphere.

For the total beam intensity measurements, the entrance port of the integrating sphere was opened, but the sample port at 180º was closed. The incident beam passed through the center of the entrance port, striking the diffuse white reflective surface on the sample port, scattering evenly around the sphere. The obtained spectrum was used as the "total" beam intensity to compare with the transmission and reflection spectra. For transmission measurements, the sample was placed perpendicular to the incident beam in front of the entrance port. For reflection measurements, the 180° port of the integrating sphere (opposite the entrance port) was opened and the sample, tilted at a 5° angle relative to the perpendicular, was placed up against this port. The tilt on the sample ensures that light reflected specularly from the sample hits the side of the

integrating sphere. Without it, specular light could leave through the entrance port and not reach the detector.

2.4 Optical Results and Discussion

The transmittance (relative to total beam) spectra (Figure 2.5a) show a significant difference between patterned and planar samples at longer wavelengths (600 nm – 850 nm). Especially around 700 nm - 750 nm, the patterned sample transmits 40 – 50% less light than the planar sample. Lower light reflection of the patterned sample was also observed at 400 nm – 650 nm wavelengths (Figure 2.5b). There are many sharper optical features seen between 600 and 800 nm; I attribute these features to complex optical resonances of my subwavelength periodic structures.

The absorbance spectra (Figure 2.5c) were calculated from transmittance and reflectance spectra. The spectra show that the patterned area has higher absorption in most of the visible spectrum. At longer wavelengths (650 nm – 800 nm), where the absorption of the planar area is very low, the patterned area has significantly more absorption.

The weighted absorbance spectra (Figure 2.5d) were calculated from the absorbance spectra weighted by the spectral irradiance AM 1.5 spectra. The integrated weighted absorbance for patterned and planar samples shows that the patterned sample captured 55% of spectral irradiance energy, whereas the planar sample only captured 35%. Moreover, this 20% improvement might be further increased by optimizing the amorphous silicon deposition profile.

Experimentally it is possible that in transmission (reflection) measurements light scattered (reflected) at wide angles (>70° relative to the normal) will not enter into and be collected in the integrating sphere, due to a ±70° acceptance angle of the sphere's ports. Such

light could appear as an increase in absorption. Also, there is drift in the light source as well as detector noise that will result in some uncertainty in the absorption measurement. By measuring reflection and transmission on patterned and unpatterned transparent PDMS only samples, we were able to put an upper bound on the uncertainty of the absorption measurement due to systematic factors such as noncollected light. There is some wide-angle low-intensity scattering (> 70 degrees from normal) from the patterned PDMS sample, however, reflection and transmission measurements account for all of the incident light with less than 5% uncertainty. There is similar wide angle scattering from the a-Si:H coated template, but it is much dimmer than from the transparent PDMS sample; it should therefore result in measurement uncertainties less than 5 % of incident.

The increased absorption at longer wavelengths is not due to lower reflection; that is, the effect is not simply antireflection. In fact, at longer wavelengths (600 nm - 800nm), the reflection of patterned samples is slightly higher than the reflection of planar samples. Nevertheless, at these long wavelengths, the patterned sample absorption is much higher. Since the only absorbing material in the sample is amorphous silicon, this difference results from increased absorption in the silicon. Since there is the same amount of silicon per area as the planar sample, the effective light path through the silicon must be longer. This is consistent with coupling of the light into in-plane guided modes as proposed by other researchers at grating periods on this scale.[13, 29] However in prior work, direct measurement of absorption by the semiconductor has not been possible due to the presence of nanopatterned metal layers. My results here indicate that the nanopatterned semiconductor itself acts as an effective coupling grating.

Periodic patterning can also minimize reflection, as I see at the short wavelength end of the spectrum in Figure 2.5b. Eisele et. al.[10] showed that periodic patterning reduced reflections

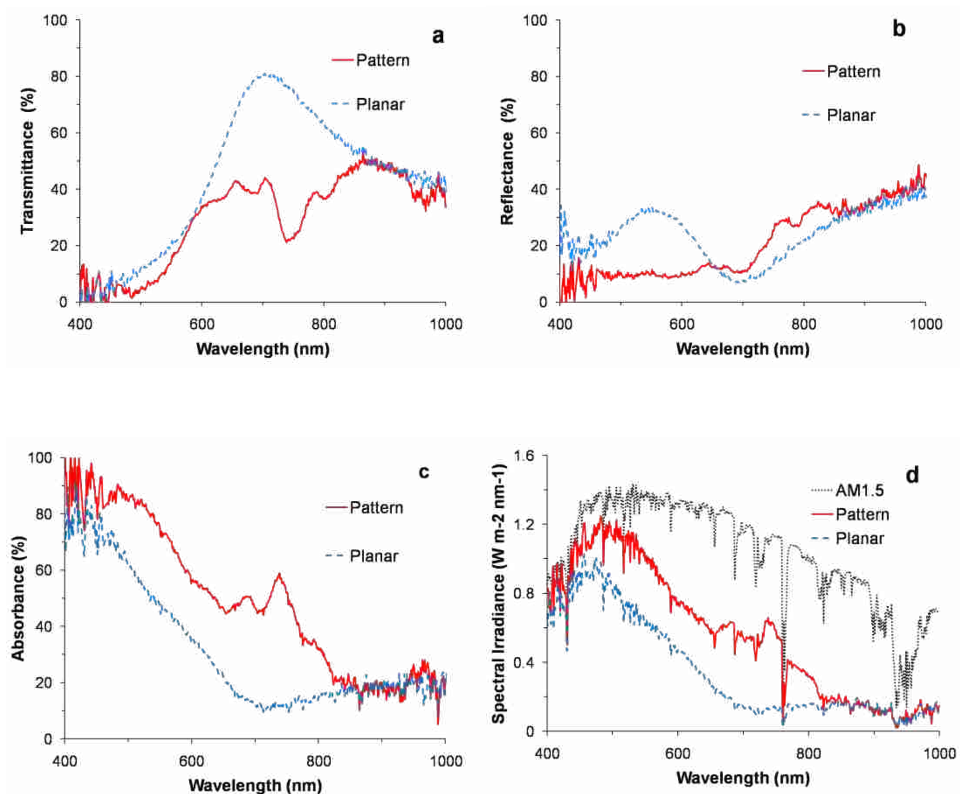

Figure 2.5. (a) transmittance spectra of patterned and planar areas, (b) reflectance spectra of patterned and planar areas, (c) absorbance spectra of patterned and planar areas, and (d) spectral irradiance of AM 1.5 and weighted absorbance of patterned and planar areas.

most effectively at 980 nm pitch. However, a shorter pitch is likely required for maximum coupling of the light into guided modes. My absorption work indicates that with a 500 nm pitch, I am effectively coupling 600 nm - 800 nm light, increasing absorption at the wavelengths most critical for light capture in amorphous silicon. Light capture is critical at the long wavelength end of the visible spectrum because a-Si has such a very small absorption coefficient there. This is also in contrast to random textures that increase absorption nonresonantly, resulting in a smaller absorption gain where it is most needed.[13]

2.5 Conclusions

I have developed a low-cost-template fabrication process for nanostructuring of amorphous silicon into a layer with a two-dimensional array of holes. This geometry was a convenient platform for optical absorption measurements on nanopatterned semiconductor layers. The increased absorption in the nanohole array indicates coupling to lateral guided surface modes. This approach provides a test bed for absorption studies in nanostructured film geometries and should result in improved light capturing designs in thin film solar cells.

2.6 Acknowledgements

I acknowledge the support of a CHIRP Grant from the College of Physical and Mathematical Sciences at Brigham Young University. Cary Tippets was supported by a grant from the BYU Office of Research and Creative Activities. I thank Steven Schultz of the BYU Department of Electrical Engineering for useful discussions.

2.7 References

1. Bergmann, R. B., Crystalline Si thin-film solar cells: a review. *Appl. Phys. A-Mater.* **1999,** *69* (2), 187-194.

2. Helbig, R. E., *Advances in solid state physics*. Vieweg: 1998.

3. Shah, A.; Torres, P.; Tscharner, R.; Wyrsch, N.; Keppner, H., Photovoltaic technology: The case for thin-film solar cells. *Science* **1999,** *285* (5428), 692-698.

4. Schropp, R. E. I.; Zeman, M., *Amorphous and microcrystalline silicon solar cells: modeling, materials, and device technology*. Kluwer Academic: Boston ; London, 1998.

5. Carlson, D. E.; Wronski, C. R., Solar-Cells Using Discharge-Produced Amorphous Silicon. *J. Electron. Mater.* **1976,** *5* (4), 436-436.

6. Guha, S.; Yang, J.; Nath, P.; Hack, M., Enhancement of Open Circuit Voltage in High-Efficiency Amorphous-Silicon Alloy Solar-Cells. *Appl. Phys. Lett.* **1986,** *49* (4), 218-219.

7. Nelson, J., *The physics of solar cells*. Imperial College Press: London, 2003.

8. Zeman, M.; Krc, J., Optical and electrical modeling of thin-film silicon solar cells. *J. Mater. Res.* **2008,** *23* (4), 889-898.

9. Atwater, H. A.; Polman, A., Plasmonics for improved photovoltaic devices. *Nat. Mater.* **2010,** *9* (3), 205-213.

10. Eisele, C.; Nebel, C. E.; Stutzmann, M., Periodic light coupler gratings in amorphous thin film solar cells. *J. Appl. Phys.* **2001,** *89* (12), 7722-7726.

11. Fahr, S.; Rockstuhl, C.; Lederer, F., Engineering the randomness for enhanced absorption in solar cells. *Appl. Phys. Lett.* **2008,** *92* (17), 171114.

12. Fan, Z. Y.; Razavi, H.; Do, J. W.; Moriwaki, A.; Ergen, O.; Chueh, Y. L.; Leu, P. W.; Ho, J. C.; Takahashi, T.; Reichertz, L. A.; Neale, S.; Yu, K.; Wu, M.; Ager, J. W.; Javey, A., Three-

dimensional nanopillar-array photovoltaics on low-cost and flexible substrates. *Nat. Mater.* **2009,** *8* (8), 648-653.

13. Ferry, V. E.; Verschuuren, M. A.; Li, H. B. T.; Verhagen, E.; Walters, R. J.; Schropp, R. E. I.; Atwater, H. A.; Polman, A., Light trapping in ultrathin plasmonic solar cells. *Opt. Express* **2010,** *18* (13), A237-A245.

14. Franken, R. H.; Stolk, R. L.; Li, H.; van der Werf, C. H. M.; Rath, J. K.; Schropp, R. E. I., Understanding light trapping by light scattering textured back electrodes in thin film n-i-p-type silicon solar cells. *J. Appl. Phys.* **2007,** *102* (1), 121904.

15. Garnett, E.; Yang, P. D., Light Trapping in Silicon Nanowire Solar Cells. *Nano Lett.* **2010,** *10* (3), 1082-1087.

16. Haase, C.; Stiebig, H., Optical properties of thin-filin silicon solar cells with grating couplers. *Prog. Photovoltaics* **2006,** *14* (7), 629-641.

17. Han, S. E.; Chen, G., Optical Absorption Enhancement in Silicon Nanohole Arrays for Solar Photovoltaics. *Nano Lett.* **2010,** *10* (3), 1012-1015.

18. Kanamori, Y.; Kobayashi, K.; Yugami, H.; Hane, K., Subwavelength antireflection gratings for GaSb in visible and near-infrared wavelengths. *Jpn. J. Appl. Phys. 1* **2003,** *42* (6B), 4020-4023.

19. Kayes, B. M.; Atwater, H. A.; Lewis, N. S., Comparison of the device physics principles of planar and radial p-n junction nanorod solar cells. *J. Appl. Phys.* **2005,** *97* (11), 114302.

20. Kelzenberg, M. D.; Boettcher, S. W.; Petykiewicz, J. A.; Turner-Evans, D. B.; Putnam, M. C.; Warren, E. L.; Spurgeon, J. M.; Briggs, R. M.; Lewis, N. S.; Atwater, H. A., Enhanced absorption and carrier collection in Si wire arrays for photovoltaic applications. *Nat. Mater.* **2010,** *9* (3), 239-244.

21. Krc, J.; Smole, F.; Topic, M., Potential of light trapping in microcrystalline silicon solar cells with textured substrates. *Prog. Photovoltaics* **2003,** *11* (7), 429-436.

22. Peng, K. Q.; Wang, X.; Li, L.; Wu, X. L.; Lee, S. T., High-Performance Silicon Nanohole Solar Cells. *J. Am. Chem. Soc.* **2010,** *132* (20), 6872.

23. Sato, K.; Gotoh, Y.; Wakayama, Y.; Hayasahi, Y.; Adachi, K.; H. Nishimura, Highly textured SnO2:F TCO films for a-Si solar cells. *Rep. Res. Lab. Asahi Glass Co. Ltd.* **1992,** *42*, 129–137

24. Senoussaoui, N.; Krause, M.; Muller, J.; Bunte, E.; Brammer, I.; Stiebig, H., Thin-film solar cells with periodic grating coupler. *Thin Solid Films* **2004,** *451-52*, 397-401.

25. Zhu, J.; Hsu, C. M.; Yu, Z. F.; Fan, S. H.; Cui, Y., Nanodome Solar Cells with Efficient Light Management and Self-Cleaning. *Nano Lett.* **2010,** *10* (6), 1979-1984.

26. Nakayama, K.; Tanabe, K.; Atwater, H. A., Plasmonic nanoparticle enhanced light absorption in GaAs solar cells. *Appl. Phys. Lett.* **2008,** *93* (12), 121904.

27. Kanamori, Y.; Roy, E.; Chen, Y., Antireflection sub-wavelength gratings fabricated by spin-coating replication. *Microelectron. Eng.* **2005,** *78-79*, 287-293.

28. Sopian, K.; Asim, N.; Amin, N.; Zaidi, S. H., Enhancement of Optical Absorption in Thin-Film Silicon Solar Cells in Silicon-On-Insulator (SOI) Configuration. *European Journal of Scientific Research* **2008,** *24* (3), 358-364.

29. Soderstrom, K.; Haug, F. J.; Escarre, J.; Cubero, O.; Ballif, C., Photocurrent increase in n-i-p thin film silicon solar cells by guided mode excitation via grating coupler. *Appl. Phys. Lett.* **2010,** *96* (21), 213508.

30. Schropp, R. E. I.; Zeman, M., New developments in amorphous thin-film silicon solar cells. *IEEE Trans. Electron Devices* **1999,** *46* (10), 2086-2092.

31. Johnston, K. W.; Pattantyus-Abraham, A. G.; Clifford, J. P.; Myrskog, S. H.; MacNeil, D. D.; Levina, L.; Sargent, E. H., Schottky-quantum dot photovoltaics for efficient infrared power conversion. *Appl. Phys. Lett.* **2008,** *92* (15), 151115.

32. Brabec, C. J.; Dyakonov, V.; Scherf, U., *Organic photovoltaics: materials, device physics, and manufacturing technologies*. Wiley-VCH: Weinheim, 2008.

33. Brabec, C. J., *Organic photovoltaics: concepts and realization*. Springer: Berlin; London, 2003.

34. Guo, L. J., Nanoimprint lithography: Methods and material requirements. *Adv. Mater. (Weinheim, Ger.)* **2007,** *19* (4), 495-513.

35. Odom, T. W.; Love, J. C.; Wolfe, D. B.; Paul, K. E.; Whitesides, G. M., Improved pattern transfer in soft lithography using composite stamps. *Langmuir* **2002,** *18* (13), 5314-5320.

36. Luque, A.; Hegedus, S.; Knovel (Firm), Handbook of photovoltaic science and engineering. Wiley: Hoboken, NJ, 2003.

Chapter 3 Processing of Thin, Composite Carbon Nanotube-Polyimide Composite Membranes

3.1 Abstract

Here I report a straightforward method for fabricating freely suspended, thin, carbon nanotube (CNT) membranes infiltrated with polymers. A CNT film was made by compressing (rolling) vertically aligned carbon nanotubes (VACNTs) on a silicon substrate. A nanotube – polymer composite film was then fabricated by spin casting a polymer layer on top of the flattened CNT film. The composite film was subsequently released from the silicon substrate by dipping in HF solution, resulting in thin, smooth, suspended membranes. To aid in releasing intact, quality films, a mesh frame was adhered to the films prior to release. Characterization of the film and membrane was performed via scanning electron microscopy (SEM) and atomic force microscopy (AFM). This process is a new approach for making thin, reinforced, smooth films or membranes with high concentrations of CNTs, which may lead to higher performance materials.

3.2 Introduction

Due to their obvious advantages of high mechanical strength, high thermal stability, good chemical resistance, low dielectric constant, light weight, and high durability, polyimide (PI) thin films and membranes have found application in microelectronic devices,[1] aircraft structures,[2] and surface protection coatings.[3] Moreover, carbon nanotubes (CNTs)[4-5] have been used to reinforce polyimide[3, 6-9] and other polymer[10-20] materials to further enhance their high strength and Young's modulus. Satyanarayana et al.[3] demonstrated that the addition of single walled carbon

nanotubes (SWCNTs) to PI increases its hardness and elastic modulus by 60–70%. Naebe et al.[7] reported a more than two-fold increase in the tensile strength of PI by addition of only 1.0% multi-walled carbon nanotubes (MWNTs). Yuen et al.[8-9] prepared PI composites in plate form with modified CNTs. Their best mechanical results showed that the composite material increases 60% in tensile strength and 130% in Young's modulus, compared to the unmodified PI. And although stable dispersions of CNT's in PI have previously been made, few reports exist on PI/CNT thin films, at least in part because only very low CNT weight fractions (< 5%) were achieved,[3] and spin casting high CNT weight fraction solutions may result in rough thin films. Other polymer (not PI)/CNT composite thin films have been reported via spin casting,[15] but their CNT weight fractions were also low.

My objective in this work was to develop a fabrication process for preparing sub-micron thickness, smooth, composite PI/CNT membranes that contained high CNT weight fractions. Because of the known difficulty in preparing high concentration CNT dispersions, I investigated a method to infiltrate polyimide into pre-existing CNT films.[12, 14] Due to the porous nature of CNT films, polymers may well diffuse into a CNT matrix and then crosslink during a curing process. In describing the preparation of thin, composite PI/CNT films, I also report a simple and straightforward release of these films to yield free standing membranes.

3.3 Experimental Procedures

A vertically aligned carbon nanotube forest (VACNT) was grown on a silicon substrate by chemical vapor deposition (CVD) (Figure 3.1). To begin this process, a silicon wafer was coated with a 30 nm alumina layer by electron beam evaporation (Denton Vacuum E-beam Evaporator). A 6 nm Fe layer was then deposited on the alumina layer by PVD sputtering (Kurt J. Lesker PVD75). These coated samples were loaded in a fused silica boat and placed into the

fused silica tube of a tube furnace. Argon gas (377 sccm) flowed through the tube during the entire growth cycle. After an initial purge with argon, the iron surface was reduced with hydrogen (396 sccm) at 750 °C. For CNT forest growth, the ethylene flow was controlled precisely. For example, to obtain a 2 μm thick VACNT forest, ethylene was flowed at 679 sccm for 1 s. Ethylene and hydrogen flow were turned off immediately after CNT growth, and the cover of the tube furnace was opened to accelerate the cooling process. With this same approach, 300 nm VACNT forests were also produced with reduced ethylene flow.

Forests were manually rolled into thin, dense CNT films on the growth substrate. As shown in Figure 3.2, a ca. 18 mm × 18 mm VACNT forest sample was placed on a hard, flat surface to avoid substrate cracking. The entire nanotube sample surface was then covered with ca. 30 mm × 30 mm piece of aluminum foil, which was taped in place so it would not shift. A 50 mm × 80 mm sheet of nitrile rubber was placed over the aluminum foil and also taped down. The rubber sheet was used to stabilize the rolling, evening out the distribution of applied forces. A smooth glass tube (1.57 cm outer diameter) was then manually rolled over and pressed into the nitrile rubber sheet more than 100 times from different directions. Finally, the nitrile rubber sheet and the aluminum foil were removed.

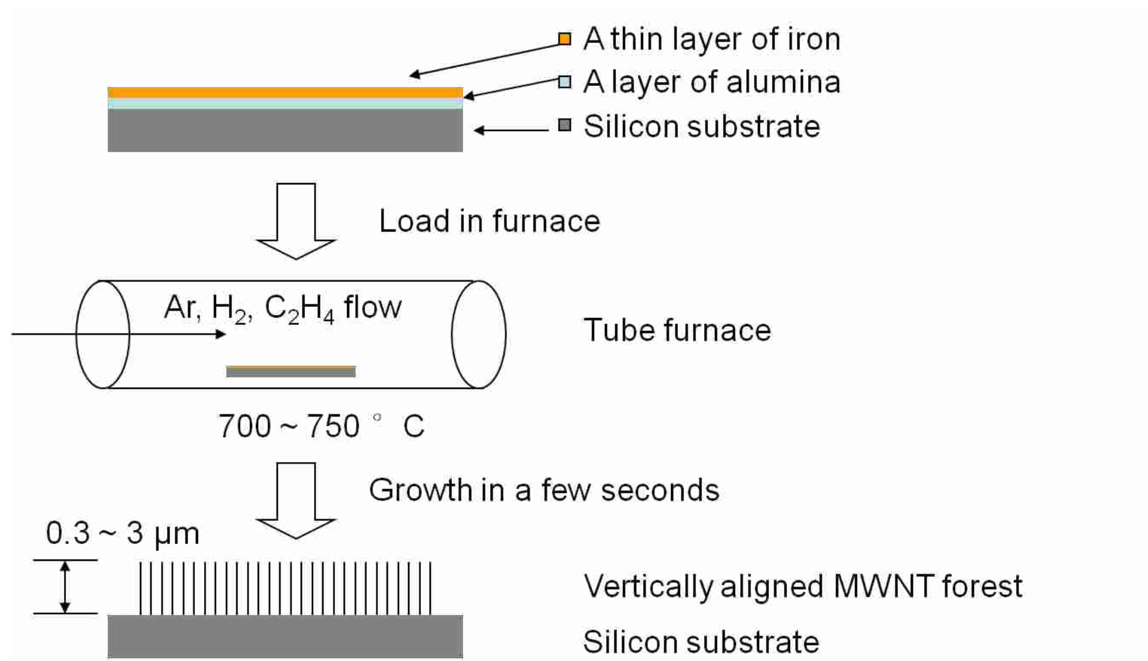

Figure 3.1. VACNT forest growth. A silicon substrate with Fe/Alumina layers was placed into a tube furnace and heated to 750 °C. Argon, hydrogen, and ethylene were used for MWNT growth. The ethylene flow was for 1 s for short VACNTs.

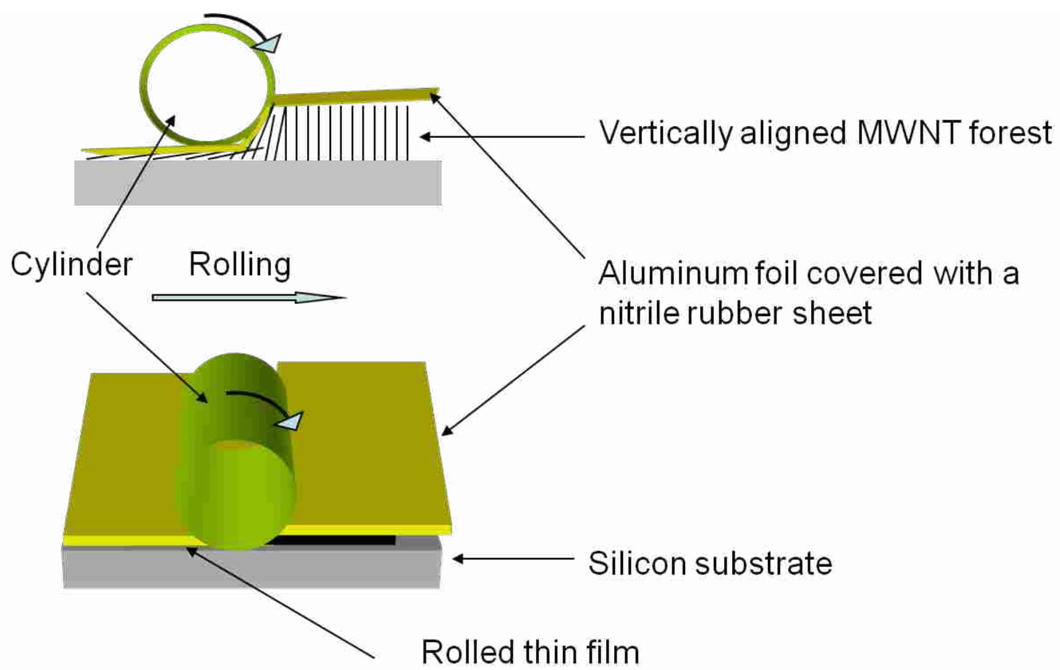

Figure 3.2. Rolling a MWNT forest into a thin film. A smooth glass tube was manually rolled over and pressed into the nitrile rubber sheet/aluminum foil/as-grown VACNT forest assembly.

The compressed CNT film was infiltrated with PI and the composite was cured in a furnace. As shown in Figure 3.3, the sample of compressed CNT film was first placed on a spin coater (WS-400B-6NPP/LITE, Laurell, North Wales, PA). The entire surface of the sample was then covered with a solution of polyimide prepolymer. The solution was allowed to sit on the substrate for 10 min to allow it to diffuse into the pressed CNT matrix. After spin casting at 2600 rpm for 90 s and baking in a furnace, a thin, smooth, polymer-CNT composite was produced. If the same spin rate and time are used for casting polyimide only, a 300 nm thick film on silicon is obtained.

The composite film was released from the silicon substrate by dipping in a solution of hydrofluoric acid (HF). To aid in this process (see Figure 3.4), a polypropylene mesh frame (Mcmaster-Carr, 9275T7) larger than the substrate was attached on the composite film with spray adhesive (3M Super 77 adhesive). The frame supports the composite film, keeping it from folding and wrinkling during release. The assembly was dipped in an aqueous HF solution (49%) for 15 min and then thoroughly rinsed with water. The film was gradually released by bending down the edges of the mesh frame that extend beyond the silicon substrate. A sub-micron thick, composite membrane was obtained. In this process, wrinkles were almost entirely avoided, since the membrane was held under tension by the frame.

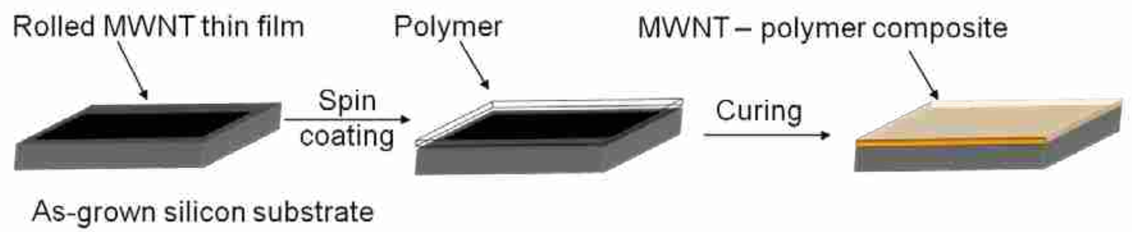

Figure 3.3. Polymer/CNT composite fabrication process. Polymer was spin coated onto a compressed CNT film. After baking in a furnace, a thin, smooth polymer/CNT composite film was produced.

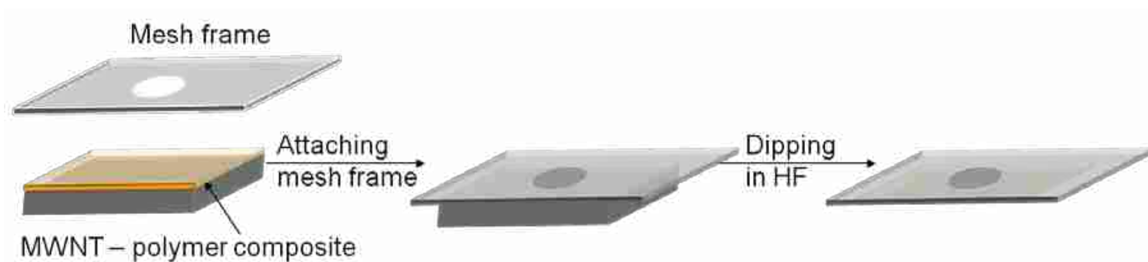

Figure 3.4. Mesh frame attachment to and release from a composite film. For release, the assembly was dipped into a solution of HF.

3.4 Results and Discussion

Figure 3.5 shows an as-grown, uniform VACNT forest prepared via CVD. Like most CNT forests, its density is low. The forest thickness (2.4 μm) was measured by SEM. For preparation of membranes with sub-micron thicknesses, short VACNTs are required. Several aspects of the CNT growth process were investigated and modified to obtain short VACNT forests:

(1) Ethylene flow time. Ethylene is the carbon source for the carbon nanotube growth. As expected, reducing the ethylene flow time reduces the thickness of the VACNT forests.

(2) Ethylene flow rate. Ethylene flow rate is another key factor for controlling the amount of carbon that is introduced. The flow rate can also be easily and precisely controlled with a mass flow controller.

(3) Argon gas flow. When argon flows with ethylene during carbon nanotube growth, the ethylene is diluted. Hence, the growth rate can be further controlled.

(4) Substrate. A sputtered iron catalyst, instead of thermally deposited iron, shows slower nanotube growth. The thickness of the iron layer also affects the CNT growth rate and diameter of nanotubes.

By adjusting these parameters, VACNT forests with initial thicknesses between 300 nm and 2 μm were made (Table 3.1). Figure 3.6 shows compressed CNT films after rolling, which resemble the mesh of fibers in a nonwoven textile, and clearly have higher densities than the initial VACNT forests. The compression ratio (the ratio of the thickness before and after rolling) was approximately 2 to 3. Unfortunately, SEM images (Figure 3.6b) also show that the manually rolling force may be uneven and can cause tearing in the films. Thus, in the

future, the rolling process should be modified and improved by using mechanically controlled machines.[21-22]

The forest was manually rolled into a thin, dense CNT film on the growth substrate. Related dry contact transfer methods have previously been reported,[12, 23-25] which compress and relocate as-grown CNT films from the growth substrate to a target substrate. Pint et al. rolled vertically aligned nanotube forests into compressed CNT thin films.[24] Liu et al. demonstrated a mechanical pressing or sliding approach to transfer CNTs via contact printing.[25] However, for our polymer infiltration process, the transfers to other materials mentioned in these earlier studies may be unnecessary, as they involve additional processing. In addition, I compared the rolling results obtained with different iron catalyst deposition techniques (thermal evaporation[23] and sputtering[22]) and found that compressed CNT films prepared from thermally evaporated Fe tend to stick to the transfer substrate, while CNT films prepared with sputtered Fe remain on the as-grown substrates without being transferred. It appears that CNTs grown with a sputtered iron catalyst have higher adhesion to their initial substrate than those prepared via thermal evaporation.

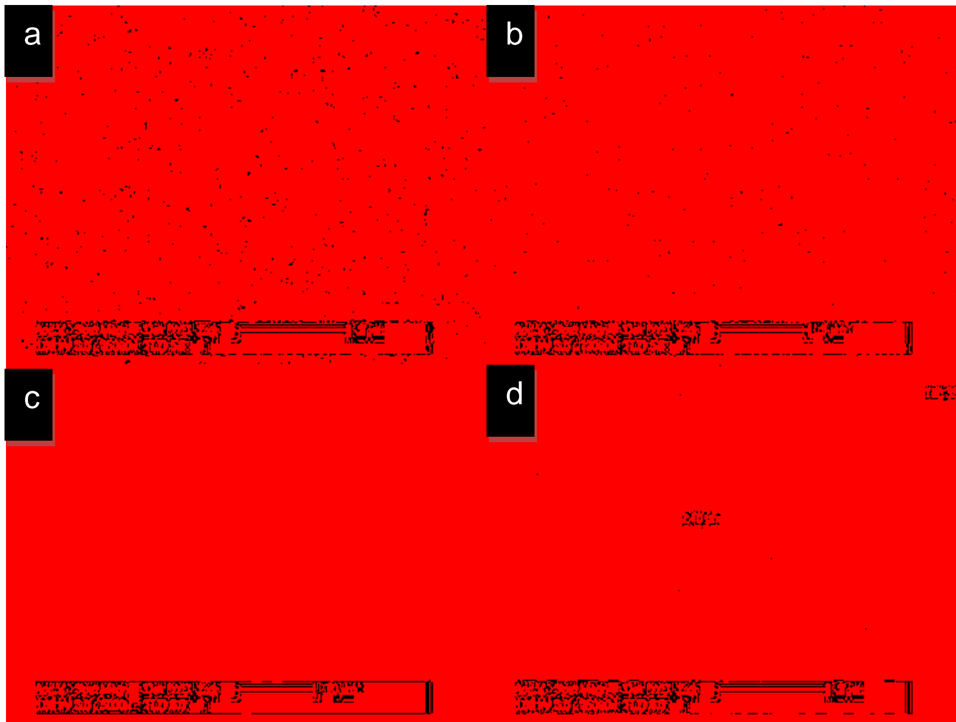

Figure 3.5. SEM images of a VACNT forest. Top view (a, b) and tilted view (c, d) at different magnifications. The forest thickness was 2.4 μm.

Table 3.1. Film thicknesses of CNT films.

As-grown VACNT	Compressed CNT	Polymer CNT Composite
2000 nm[a]	600 nm	650 nm
750 nm[b]	350 nm	450 nm
300 nm[c]	150 nm	400 nm

[a]grown under argon (377 sccm), hydrogen (396 sccm), and ethylene (679 sccm) at 750 °C for 1 s. [b]grown under argon (199 sccm), hydrogen (192 sccm), and ethylene (161 sccm) at 750 °C for 2 s. [c]grown under argon (199 sccm), hydrogen (192 sccm), and ethylene (161 sccm) at 750 °C for 1 s.

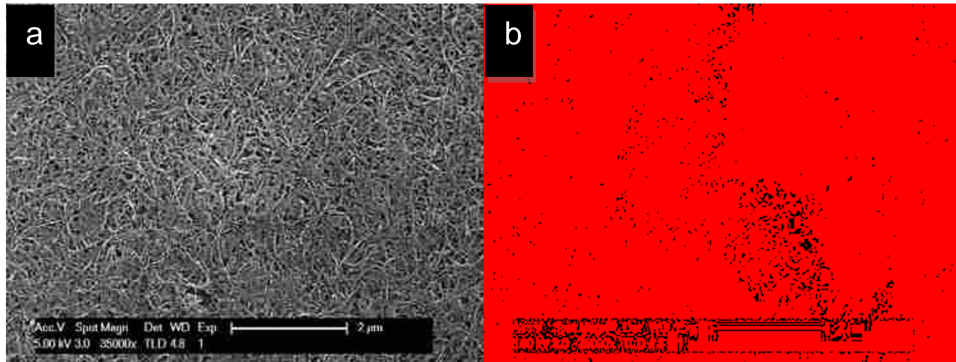

Figure 3.6. SEM images of a compressed CNT film (600 nm thick). (a) Major area of the film surface showing a high CNT density, and (b) Example of a tearing defect in a film.

The thicknesses of polymer infiltrated CNT composite films measured by AFM and SEM are given in Table 3.1. The composite films are thicker than either the compressed CNT films or the individual polymer control films. The additional thickness on the composite film may be due to excess loading of the infiltration polymer in the spin casting process. For thicker, compressed CNT films, less increase in the composite film thickness comes from the infiltration polymer. This may be because there is more space for polymer molecules to infiltrate. Figure 3.7 shows the SEM cross-section images of the composite films. Because of the shorter diffusion length required for the infiltrating polymer, the thinner composite film has fewer voids and appears to be more uniformly infiltrated than the thicker one. These images appear to show nanotubes surrounded with polymer, forming a composite film.

After preparation of polymer-CNT composite films, film release was necessary to produce free standing, composite membranes. To this end, an HF solution was used to attack the interface between the composite films and the silicon dioxide layer on the silicon substrate. However, composite films tend to be wrinkled or even folded after HF etching and subsequent water rinsing. Puckering may take place as a result of capillary forces exerted by the water during drying. Some wrinkles even appear on free-standing membranes released after application of a thick supporting polymer layer onto the composite film. To make smooth membranes, I developed a method that consisted of attaching a mesh frame to the composite film via adhesive before the release process. Since HF does not attack the frame, the adhesive, or the composite materials, the frame sticks to the composite membrane and is released with it from the silicon substrate. Because the membrane was held tightly under tension to the support, wrinkles were

almost entirely avoided. Figure 3.8 shows some released CNT-polymer membranes. The degree of membrane transparency can be tuned with the CNT film thickness.

There are a number of advantages of my release process:

(1) The polypropylene mesh frame is easy to glue onto a composite film with a spray adhesive, which is not attacked by HF solution. The mesh frame has a center hole as seen in Figure 3.8. This keeps spray adhesive off the region of interest of the film. The center hole of the mesh frame is easily made with a punch press. In addition, the size of the hole is controllable, and the polypropylene mesh material is inexpensive.

(2) The mesh frame can be easily cut into a desired size with scissors. Compared to a plastic washer, which was also considered as a support, a mesh frame better holds the membrane. The frame also allowed for a shorter HF etch release process than the washer.

(3) Large, free-standing mesh frames can be easily bent in the release process. This allows the membrane to be released in a straightforward manner by gradually squeezing the mesh frame, while directly peeling the membrane. In contrast, the rigidity of the washer creates problems in membrane release.

(4) The membrane remains in slight tension after release.

(5) The mesh frame process should be scalable to whole wafer size membranes.

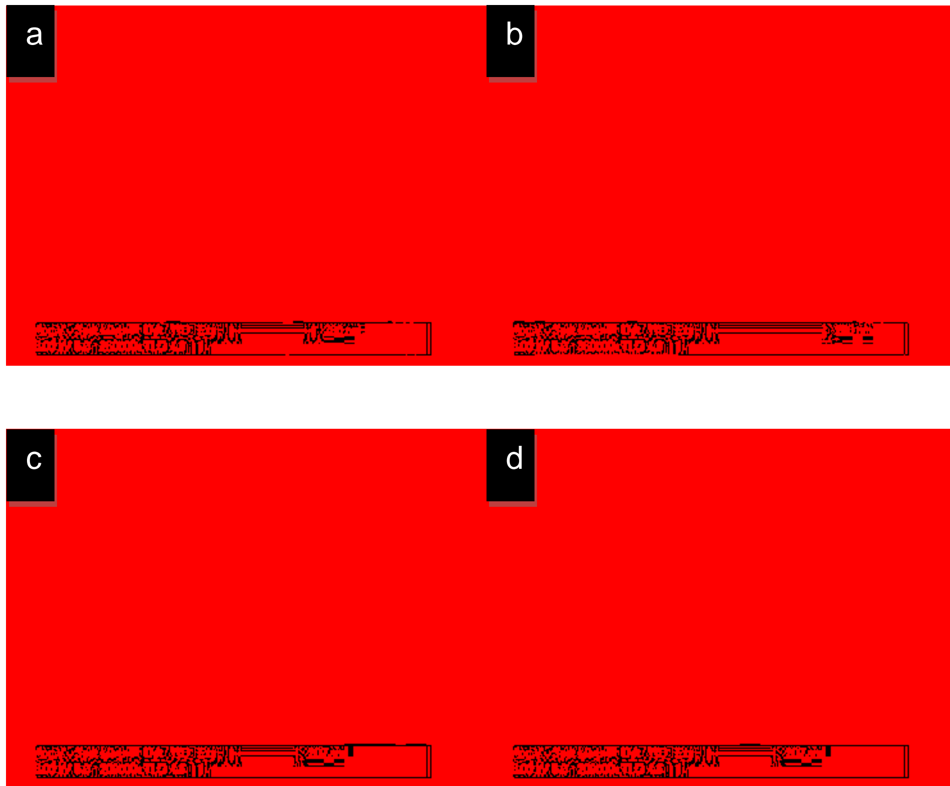

Figure 3.7. Cross-sectional SEM images of polymer CNT composite films at thicknesses of 400 nm (a, b) and 650 nm (c, d). A thin gold layer (5 nm) was sputtered on top of the sample surface to reduce charging. The samples were then frozen, cut into small pieces, and images were taken at sharp edges of the shards.

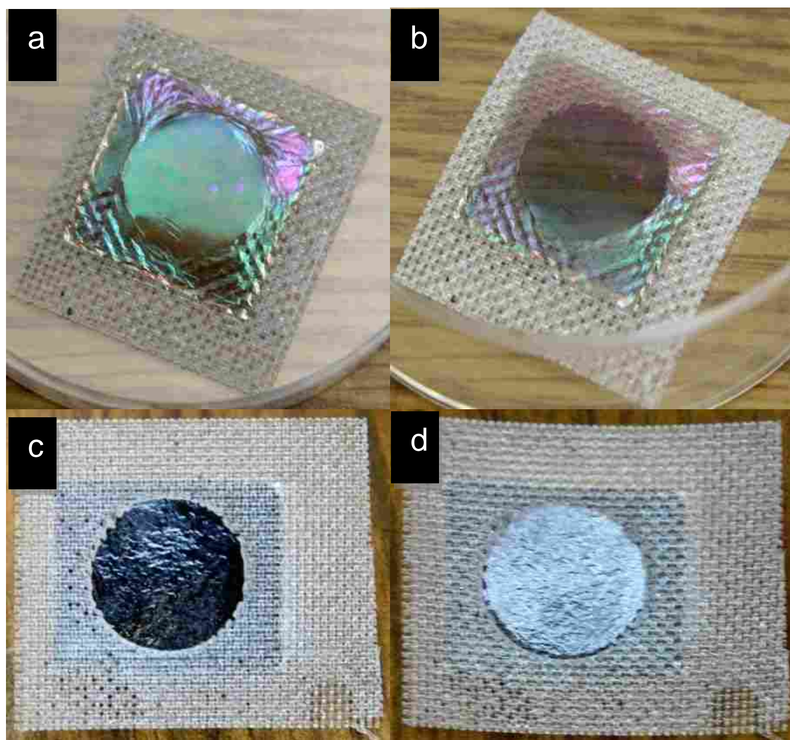

Figure 3.8. Photographs of released polymer-CNT composite membranes on mesh frames at thickness of 400 nm (a, b) and 650 nm (c, d).

3.5 Conclusions

I successfully developed a straightforward method for fabricating freely suspended, thin, carbon nanotube (CNT) membranes infiltrated with polymers. This process is a new approach for making high concentration CNT reinforced thin films or membranes, which may lead to better material performance in multiple applications.

3.6 Acknowledgements

I appreciate the research funding from Moxtek (Orem, UT).

3.7 References and Notes

1. Deligoz, H.; Ozgumus, S.; Yalcinyuva, T.; Yildirim, S.; Deger, D.; Ulutas, K., A novel cross-linked polyimide film: synthesis and dielectric properties. *Polymer* **2005,** *46* (11), 3720-3729.

2. Jiang, X. W.; Bin, Y. Z.; Matsuo, M., Electrical and mechanical properties of polyimide-carbon nanotubes composites fabricated by in situ polymerization. *Polymer* **2005,** *46* (18), 7418-7424.

3. Satyanarayana, N.; Rajan, K. S. S.; Sinha, S. K.; Shen, L., Carbon nanotube reinforced polyimide thin-film for high wear durability. *Tribol. Lett.* **2007,** *27* (2), 181-188.

4. Iijima, S., Helical Microtubules of Graphitic Carbon. *Nature* **1991,** *354* (6348), 56-58.

5. Treacy, M. M. J.; Ebbesen, T. W.; Gibson, J. M., Exceptionally high Young's modulus observed for individual carbon nanotubes. *Nature* **1996,** *381* (6584), 678-680.

6. Cai, H.; Yan, F. Y.; Xue, Q. J., Investigation of tribological properties of polyimide/carbon nanotube nanocomposites. *Mat. Sci. Eng. A-Struct.* **2004,** *364* (1-2), 94-100.

7. Naebe, M.; Wang, J.; Xue, Y. H.; Wang, X. G.; Lin, T., Carbon Nanotube Reinforced Rigid-Rod Polyimide. *J. Appl. Polym. Sci.* **2010,** *118* (1), 359-365.

8. Yuen, S. M.; Ma, C. C. M.; Chiang, C. L.; Lin, Y. Y.; Teng, C. C., Preparation and morphological, electrical, and mechanical properties of polyimide-grafted MWCNT/polyimide composite. *J. Polym. Sci. Pol. Chem.* **2007,** *45* (15), 3349-3358.

9. Yuen, S. M.; Ma, C. C. M.; Chiang, C. L.; Teng, C. C.; Yu, Y. H., Poly(vinyltriethoxysilane) modified MWCNT/polyimide nanocomposites - Preparation, morphological, mechanical, and electrical properties. *J. Polym. Sci. Pol. Chem.* **2008,** *46* (3), 803-816.

10. Coleman, J. N.; Khan, U.; Blau, W. J.; Gun'ko, Y. K., Small but strong: A review of the mechanical properties of carbon nanotube-polymer composites. *Carbon* **2006,** *44* (9), 1624-1652.

11. Hellstrom, S. L.; Lee, H. W.; Bao, Z. N., Polymer-Assisted Direct Deposition of Uniform Carbon Nanotube Bundle Networks for High Performance Transparent Electrodes. *ACS Nano* **2009,** *3* (6), 1423-1430.

12. Lahiff, E.; Ryu, C. Y.; Curran, S.; Minett, A. I.; Blau, W. J.; Ajayan, P. M., Selective positioning and density control of nanotubes within a polymer thin film. *Nano Lett.* **2003,** *3* (10), 1333-1337.

13. Naebe, M.; Lin, T.; Tian, W.; Dai, L. M.; Wang, X. G., Effects of MWNT nanofillers on structures and properties of PVA electrospun nanofibres. *Nanotechnology* **2007,** *18* (22), 225605.

14. Peng, H. S., Aligned carbon nanotube/polymer composite films with robust flexibility, high transparency, and excellent conductivity. *J. Am. Chem. Soc.* **2008,** *130* (1), 42.

15. Pyo, M.; Bae, E. G.; Cho, Y.; Jung, Y. S.; Zong, K., Composites of low bandgap conducting polymer-wrapped MWNT and poly(methyl methacrylate) for low percolation and high transparency. *Synth. Met.* **2010,** *160* (19-20), 2224-2227.

16. Qian, D.; Dickey, E. C.; Andrews, R.; Rantell, T., Load transfer and deformation mechanisms in carbon nanotube-polystyrene composites. *Appl. Phys. Lett.* **2000,** *76* (20), 2868-2870.

17. Sreekumar, T. V.; Liu, T.; Min, B. G.; Guo, H.; Kumar, S.; Hauge, R. H.; Smalley, R. E., Polyacrylonitrile single-walled carbon nanotube composite fibers. *Adv. Mater. (Weinheim, Ger.)* **2004,** *16* (1), 58 - 61.

18. Zeng, J. J.; Saltysiak, B.; Johnson, W. S.; Schiraldi, D. A.; Kumar, S., Processing and properties of poly(methyl methacrylate)/carbon nanofiber composites. *Compos. Part B-Eng.* **2004,** *35* (3), 245-249.

19. Zhang, X. F.; Liu, T.; Sreekumar, T. V.; Kumar, S.; Moore, V. C.; Hauge, R. H.; Smalley, R. E., Poly(vinyl alcohol)/SWNT composite film. *Nano Lett.* **2003,** *3* (9), 1285-1288.

20. Zhou, Y. X.; Wu, P. X.; Cheng, Z. Y.; Ingram, J.; Jeelani, S., Improvement in electrical, thermal and mechanical properties of epoxy by filling carbon nanotube. *Express Polym. Lett.* **2008,** *2* (1), 40-48.

21. Tawfick, S.; O'Brien, K.; Hart, A. J., Flexible High-Conductivity Carbon-Nanotube Interconnects Made by Rolling and Printing. *Small* **2009,** *5* (21), 2467-2473.

22. Bradford, P. D.; Wang, X.; Zhao, H. B.; Maria, J. P.; Jia, Q. X.; Zhu, Y. T., A novel approach to fabricate high volume fraction nanocomposites with long aligned carbon nanotubes. *Compos. Sci. Technol.* **2010,** *70* (13), 1980-1985.

23. Pint, C. L.; Xu, Y. Q.; Moghazy, S.; Cherukuri, T.; Alvarez, N. T.; Haroz, E. H.; Mahzooni, S.; Doorn, S. K.; Kono, J.; Pasquali, M.; Hauge, R. H., Dry Contact Transfer Printing of Aligned Carbon Nanotube Patterns and Characterization of Their Optical Properties for Diameter Distribution and Alignment. *ACS Nano* **2010,** *4* (2), 1131-1145.

24. Pint, C. L.; Xu, Y. Q.; Pasquali, M.; Hauge, R. H., Formation of highly dense aligned ribbons and transparent films of single-walled carbon nanotubes directly from carpets. *ACS Nano* **2008,** *2* (9), 1871-1878.

25. Liu, H. P.; Takagi, D.; Chiashi, S.; Homma, Y., Transfer and Alignment of Random Single-Walled Carbon Nanotube Films by Contact Printing. *ACS Nano* **2010,** *4* (2), 933-938.

Chapter 4 Laser Activation-Modification of Semiconductor Surfaces (LAMSS) of 1-Alkenes on Silicon: A ToF-SIMS, Chemometrics, and AFM Analysis

4.1 Abstract

Laser-activation-modification of semiconductor surfaces (LAMSS) was carried out on silicon with a series of 1-alkenes. These laser spots were studied by time of flight secondary ion mass spectrometry (ToF-SIMS). The resulting spectra were analyzed using the multivariate curve resolution (MCR) method within the Automated eXpert Spectral Image Analysis (AXSIA) toolkit, and also by MCR and cluster analysis using commercially available toolboxes for Matlab: the PLS_Toolbox and the MIA_Toolbox, respectively. AXSIA based MCR generally finds three components for the spectral images: one for the background and two for the laser-activated spots, for both the positive and negative ion images. The negative ion component spectra from the spots show increased carbon and hydrogen signals compared to oxygen. They also show reduced chlorine and fluorine (contamination) peaks. In order to compare AXSIA-MCR results from different images, the AXSIA component spectra of different spots were further analyzed by principal components analysis (PCA). PCA of all of the negative ion components shows that component 1 is chemically distinct from components 2 and 3. PCA of all of the positive ion components yields the same result. The loadings plots of this PCA analysis confirm that component 1 generally contains fragments expected from the substrate, while components 2 and 3 contain fragments expected from an overlayer composed of alkyl chains in the spots. A comparison of the two MCR analyses suggests that roughly the same information can be obtained from AXSIA, which is not commercially available, and the PLS_Toolbox. Cluster analysis of the data also clearly separates the spots from the backgrounds. A key finding from

these analyses is that the degree of surface functionalization in a LAMSS spot appears to decrease radially from the center of the spot. Finally, a comparison of atomic force microscopy (AFM) of the spots vs. the AXSIA analysis of the ToF-SIMS data produced another important result, which is that the surface morphology is only weakly correlated with the LAMSS chemistry.

4.2 Introduction

Time of flight secondary ion mass spectrometry (ToF-SIMS) is a powerful tool for surface analysis.[1-3] The secondary ion spectra produced by this method usually consist of hundreds or even thousands of peaks. This complexity is further increased when ToF-SIMS is used in its imaging mode, in which case three-way (three-dimensional) data sets are created, where two dimensions correspond to the x and y lateral dimensions of the image and the third dimension corresponds to mass spectra taken at the pixels.[4] An image can easily consist of 128 by 128 pixels, each with a complete mass spectrum associated with it, leading to the formation of very large data matrices. The data set from a ToF-SIMS image can contain millions of spectral regions for consideration. In conventional data analysis methods, an analysis would consider only a few characteristic peaks, based on the pre-knowledge of the operator, and these peaks would be compared from sample to sample. This approach is often adequate for well-known samples. However the risk of peak choice bias, and of missing important information for unknown samples is real since the majority of the sample data is wasted in a univariate approach. As a result, the ToF-SIMS community is increasingly employing chemometrics methods to analyze their large data matrices.[5-12] Methods such as principal components analysis (PCA) and partial least squares (PLS) have now been employed a number of times for this purpose.[5-6, 13-14]

The results of this chapter are divided into three sections. The first section contains a ToF-SIMS study of the homologous series of 1-alkenes deposited onto silicon with the laser-activation modification of semiconductor surfaces (LAMSS) method.[15] The LAMSS method consists of wetting a silicon surface with a liquid and then firing a laser pulse through the liquid onto the surface to drive a chemical reaction between the substrate and the chemical above it. This set of spots is analyzed using the multivariate curve resolution (MCR) algorithm in the Automated eXpert Spectral Image Analysis (AXSIA) tool kit. AXSIA based MCR has previously been applied to ToF-SIMS data.[16-20] AXSIA was originally developed by Sandia National Laboratories and has been broadly used for analysis of data sets collected by many different instruments. MCR simplifies a ToF-SIMS total ion image that contains information of all spectral channels of a sample to a limited number of component images that sufficiently describe the chemical variations of a sample surface. Each component image is represented by a full mass spectrum with characteristic spectral signatures. Compared to the individual ion images of ToF-SIMS, these components are more representative in describing chemical information of sample surfaces.

The AXSIA analysis of the ToF-SIMS images of LAMSS on silicon with 1-alkenes generates essentially two types of different AXSIA components for each sample: a background or unmodified part, and a functionalized region. A principal components analysis (PCA) of the component spectra generated by AXSIA shows that all components from all of the LAMSS spots designated as backgrounds form a cluster based on similarity and show significant inorganic spectral characteristics; while, all the components from functionalized regions form a separate cluster showing significant organic spectral characteristics, all as expected. These results provide additional characterization for surface modification by LAMSS of silicon wetted with 1-alkenes.

The importance of this PCA analysis of MCR components is that it allows MCR results from different images to be compared; PCA of MCR factors should be useful for other ToF-SIMS imaging data sets as well, especially when one is comparing complicated data sets with multiple components.

In the second section of this chapter, I analyze a different set of LAMSS spots that were made at lower power densities. These spots are also analyzed by AXSIA, which shows that these spots exhibit a radial decrease in surface functionalization, i.e., they appear to be of higher quality than the LAMSS spots analyzed in the first section. These results indicate that changing the optics and/or laser power in the LAMSS process can change the surface chemistry.

A major drawback to the AXSIA toolkit is that the software is not yet commercially available. I therefore compared some of our AXSIA based MCR results to those obtained using an MCR algorithm within the PLS_Toolbox, which is commercially available from Eigenvector Research. The amount of user input and work in selecting factors is higher, but not burdensome, for the MCR analysis performed using the PLS_Toolbox, *i.e.*, the PLS_Toolbox requires the user to determine the number of factors that should be used. It appears that very similar information can be obtained with both methods. The PLS_Toolbox MCR analysis confirms the radial decrease in surface functionalization of the LAMSS spots.

In any statistical analysis, it is important to consider errors and confidence limits for results. Thus, the ability of the factor-based MCR model to account for the variation in the data was checked. A PCA analysis of the data with the same number of factors was also performed and the errors associated with this analysis were studied. The PLS_Toolbox provides Q Residuals for its MCR analysis, and Hotelling T^2 and Q Residuals analyses for its PCA analysis.

These analyses showed that the outliers in the MCR and PCA analyses were largely localized in the LAMSS spots. This small inadequacy in the MCR analysis led me to perform a cluster analysis, which was not based on factors. Cluster analysis was performed with the sister toolbox of the PLS_Toolbox: the MIA_Toolbox. Cluster analysis provided complementary results to the MCR analyses that had been performed.

Finally, in the third section of this chapter, LAMSS spots were analyzed by both atomic force microscopy (AFM)[21-22] and ToF-SIMS to understand the relationship between surface morphology and surface chemistry. A comparison of MCR results with those obtained by AFM indicate that the surface morphology is only weakly correlated with the surface chemistry.

4.3 Brief Overview of PCA and MCR

The following is intended to be a brief explanation of principal components analysis (PCA) and multivariate curve resolution (MCR). For a more complete explanation, the reader is referred to any of a number of books on chemometrics.[7-8, 23-29]

PCA takes all of the data in a data set into account to extract the essential factors that are responsible for the difference among the samples. These factors are the principal components (PCs) that capture the majority of the variation in the data set. PCA can usually simplify a complex data set into several PCs that account for most of the variance in the samples of concern. Each PC is associated with scores or projections of the samples in the data set on that PC, which can often separate samples into subgroups based on their similarities. Loadings describe the contributions of original variables or peaks to the PCs. Thus, PCA analysis of a ToF-SIMS data set reveals the major factors that underlie the variation among the samples and the peaks responsible for those major factors.

MCR is a well-established chemometrics technique. It can be viewed as an extension of classical least squares (CLS). The governing equation of CLS is $\mathbf{S} = \mathbf{P}*\mathbf{C}$. In this equation, **S** is a matrix containing a series of spectra as columns in the matrix, which are believed to be linear combinations of a set of pure component spectra in the matrix **P**. The **C** matrix gives the contributions of the pure component spectra to the spectra in the **S** matrix. In CLS, **S** and **P** are known, so **C** is obtained by left multiplying both sides of the CLS equation by the pseudoinverse of **P** to obtain the equation: $\mathbf{C} = (\mathbf{P}^T\mathbf{P})^{-1}\mathbf{P}^T\mathbf{S}$, where $\mathbf{P}^T$ is the transpose of **P** and $(\mathbf{P}^T\mathbf{P})^{-1}$ is the matrix inverse of $\mathbf{P}^T\mathbf{P}$. MCR differs from CLS in that only the matrix **S** is known. The CLS equation is therefore solved in two ways to obtain:

$$\mathbf{C} = (\mathbf{P}^T\mathbf{P})^{-1}\mathbf{P}^T\mathbf{S} \quad (4.1)$$

$$\mathbf{P} = \mathbf{S}\mathbf{C}^T(\mathbf{C}\mathbf{C}^T)^{-1} \quad (4.2)$$

A guess for **P** is then entered into Equation 4.1. The calculated **C** values are next entered into Equation 4.2. The elements of the **P** and **C** matrices are subject to a nonnegativity constraint. After repeated iterations of Equations 4.1 and 4.2, convergence of the **P** and **C** matrices may be obtained. With PLS_Toolbox MCR, the user inputs the number of pure components (factors) that the model is to calculate. The user has the option, which was not exercised in this work, of providing guesses for these factors.

4.4 Experimental Section

4.4.1 Materials

Silicon (100) wafers (p-boron, 2-6 Ω cm, test grade) were obtained from Montco Silicon Technologies. (Spring-City, PA). 1-Hexene (97%) and 1-octene (97%) were obtained from Acros (Morris Plains, NJ). 1-Decene (96%) was obtained from Lancaster (Windham, NH). 1-

Dodecene (95%) was obtained from Aldrich (Milwaukee, WI). 1-Tetradecene (97%) and 1-hexadecene (99%) were obtained from Fluka (Milwaukee, WI). All chemicals were used as received. Water was obtained from a Millipore Milli-Q water system, and acetone was reagent grade.

4.4.2 Sample preparation

All LAMSS experiments were carried out with pulses from a Nd:YAG (Coherent Infinity) laser in an open laboratory with compounds that were not degassed or specially treated in any way. To prepare a LAMSS sample, a clean silicon chip was loaded onto a manually controlled two-dimensional translation stage and wetted with a reagent. A laser beam was then focused by a short focus lens (50 mm) onto the reagent-wetted silicon chip. Here LAMSS samples were usually prepared by using 1 mJ of 532 nm laser light with a pulse length of 4 ns. The laser was run at 1 Hz to guarantee that only one laser pulse was incident on each spot on the sample. The samples were again cleaned with a standard procedure described elsewhere and stored in a vacuum chamber before ToF-SIMS analysis.

4.4.3 ToF-SIMS imaging

ToF-SIMS was performed with an ION-TOF TOF-SIMS IV instrument with monoisotopic 25 KeV $^{69}Ga^+$ primary ions in bunched mode. The 1-alkene- modified spots on silicon by LAMSS were around 100 μm in diameter. The ToF-SIMS was set up with imaging size of 201 μm × 201 μm with a LAMSS spot inside, with a resolution of 128 × 128 pixels, 5 shots per pixel and 30 scans per image. A bunch of ions and total ions for each sample were selected for real-time imaging and these images were then saved for subsequent comparison. Raw data files were saved for the multivariate statistical analysis. To do multivariate statistical analysis (AXSIA analysis as well as PLS analysis), the ToF-SIMS raw data files were first

converted into a format that could be read. To reduce file size the mass range over 0 – 400 or 0 – 200 amu was binned every 0.5 amu (e.g., 0.25-0.75 amu is 0.5 amu, 0.75-1.25 amu is 1.0 amu, etc.). Retrospective spectral analysis confirmed that all of the spectral features were within this mass range. The same data file was used as the input for all of the multivariate statistical analysis reported here.

4.4.4 AXSIA-based MCR analysis of ToF-SIMS imaging

AXSIA was run with a PC Microsoft Windows 2000 operating system. The AXSIA analysis generated component images that were visualized in different colors to express chemical variations among a ToF-SIMS imaging area, and corresponding spectra of the components for a given ToF-SIMS raw data file. The data file before AXSIA analysis was visualized as a so-called mean image, similar to its ToF-SIMS total ion image.

4.4.5 PCA analysis of AXSIA components

PCA analysis on the AXSIA component spectra helps to interpret the chemical variations shown on the component images. To do PCA, a data matrix was created with all the major positive or negative component spectra of all samples. That is, a component spectrum became a row and a binned 0.5 amu unit became a column of the matrix. After normalization of each row, the matrix was loaded and analyzed using the PLS_Toolbox 3.0 software from Eigenvector Research. (Wenatchee, WA) that runs on a PC Matlab (Natick, MA) platform, where mean centering data preprocessing was used. The first principal component (PC1) generated by PCA that captured the majority of the variation in the data matrix and its loadings plot were chosen for further consideration.

4.4.6 PCA, MCR, and cluster analysis

PCA and MCR of the data in Figure 4.7 were performed with the PLS_Toolbox 3.5 (not version 3.0) for Matlab from Eigenvector Research. Robust k-means cluster analysis, simply referred to as “cluster analysis” in this work, was performed with the MIA_Toolbox 1.0 for Matlab, also from Eigenvector Research. This "robust" clustering algorithm is specifically designed not to be strongly influenced by outliers. For PCA, MCR, and cluster analysis with the Eigenvector software, no preprocessing of the data was performed, *i.e.*, not even normalization, except prior to PCA where the data were mean centered. While initial guesses for these pure component spectra can be entered into the MCR analysis, no such guesses were used in my study and I relied on those generated by the software.[30]

4.5 Results and Discussion

4.5.1 AXSIA analysis of ToF-SIMS images of LAMSS spots

Figure 4.1 shows the comparison of AXSIA images and original ToF-SIMS negative ion images of silicon modified with 1-decene and 1-tetradecene by LAMSS. Very similar results to these were obtained for the other 1-alkenes studied. As expected, AXSIA analysis showed that there were essentially two major distinct regions on each sample: the unmodified region or background represented by AXSIA component 1 or C1 (in red), and the modified spots represented by C2 (in green) and C3 (in blue). The different colors of the component images serve as an aid in visualizing them, and the color intensity is linear with signal intensity. The composite image shows the contributions of C1, C2 and C3 for each sample. It is obvious that the component images: C1, C2 and C3, and composite images of AXSIA reveal significantly different variations over the imaged area and clearly separate out the background and 1-alkene modified regions, while the mean image without AXSIA analysis or ToF-SIMS total ion image

did not show much variation over the imaging areas. Although the same general variation in C1 – C3 was also shown by the individual ToF-SIMS images (O^-, H^-, C_2H^-, Si^-, etc.), the AXSIA results consider a much larger fraction of the data, they have higher S/N ratios and, therefore, provide images with higher contrast.

Consistent results were again obtained from AXSIA analysis of positive ion ToF-SIMS images of silicon surfaces modified by LAMSS using various 1-alkenes, which basically had two chemically distinct regions: the background and the modified area (see Figure 4.2). Here, each row includes one sample's AXSIA component images and the composite image followed by its original Si^+ image for comparison. Again, C1 corresponds to the background and C2 and/or C3 indicate 1-alkene modified regions. It is seen that samples modified with 1-decene and 1-tetradecene (the 3rd and 5th rows in Figure 4.2) contain only two major components, C1 and C2. Note that C2 of the sample modified with 1-dodecene (4th row) reveals a rather uniform distribution over the entire measured area, which may represent a "uniform" distribution of a surface contaminant over the imaged area.

The individual spectra of the AXSIA components give the spectral sources of the chemical variations over the imaging area or among the components of each sample. Figure 4.3 shows the negative-ion AXSIA component spectra (mass range 0-100 amu) of silicon surfaces modified with 1-hexene and 1-hexadecene. These spectra are representative of all of the spectra obtained from the homologous series of 1-alkenes. That is, the C1 component spectra of the two samples are similar to each other and to the other C1 spectra from the other 1-alkene adsorbates, but they are significantly different from the C2s and C3s, which are similar to each other and from sample to sample. These spectra clearly show the variations between the components. For example, small SiO_2^- and SiO_3^- peaks are seen in the C1 spectra from unmodified silicon, while a

$Si_2C_2^-$ peak is seen in the C3 spectra, but not C2 spectra, providing additional evidence for alkyl modification by LAMSS. In addition, the C1 spectra contain different ions that are attributable to surface contamination (F^-, $^{35}Cl^-$ and $^{37}Cl^-$), but the intensities of these peaks in the C2 and C3 spectra from the modified regions are greatly reduced. In a typical univariate analysis of the data, it would be easy to miss some of this variation that is so clear in these component spectra.

Similarly, Figure 4.4 shows the positive ion component spectra (mass range 0-100 amu) of silicon surfaces modified with 1-octene and 1-hexadecene. The component images corresponding to these spectra are shown in Figure 4.2, second from the top and bottom, respectively. Compared to the negative ion spectra, these positive ion spectra are more complicated and less different, obvious differences are not as easily discerned. Nevertheless, it is clear that the ratios of peaks change considerably going from C1 to C2 and C3, and that C2 and C3 are similar; i.e., note that C2 and C3 for the 1-octene modified surface resemble C3 and C2 for the 1-hexadecene surface, respectively. The complexity of these spectra would make a univariate approach to data analysis difficult; however, tools such as MCR easily accomplish this task. That is, in this particular case, AXSIA finds essentially the same components for the modified spots. The fact that it labels them differently is not of importance; i.e., for PCA, the ranking of the principal components is important, but this is not the case in AXSIA, where the component numbers do not have this type of significance.

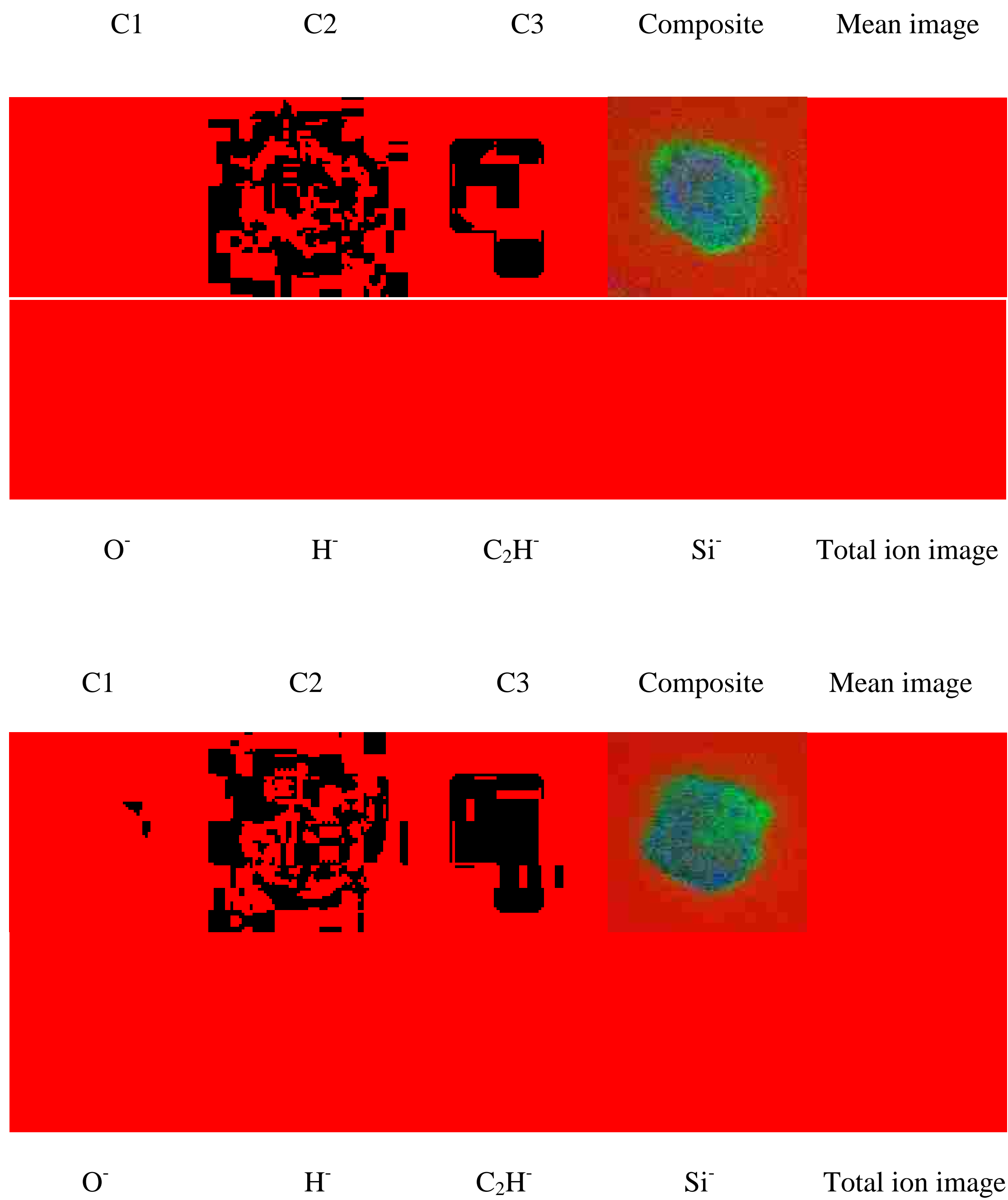

Figure 4.1. AXSIA images and selected ToF-SIMS images from negative ion images of silicon surfaces modified by LAMSS with 1-decene (upper panel), and 1-tetradecene (lower panel).

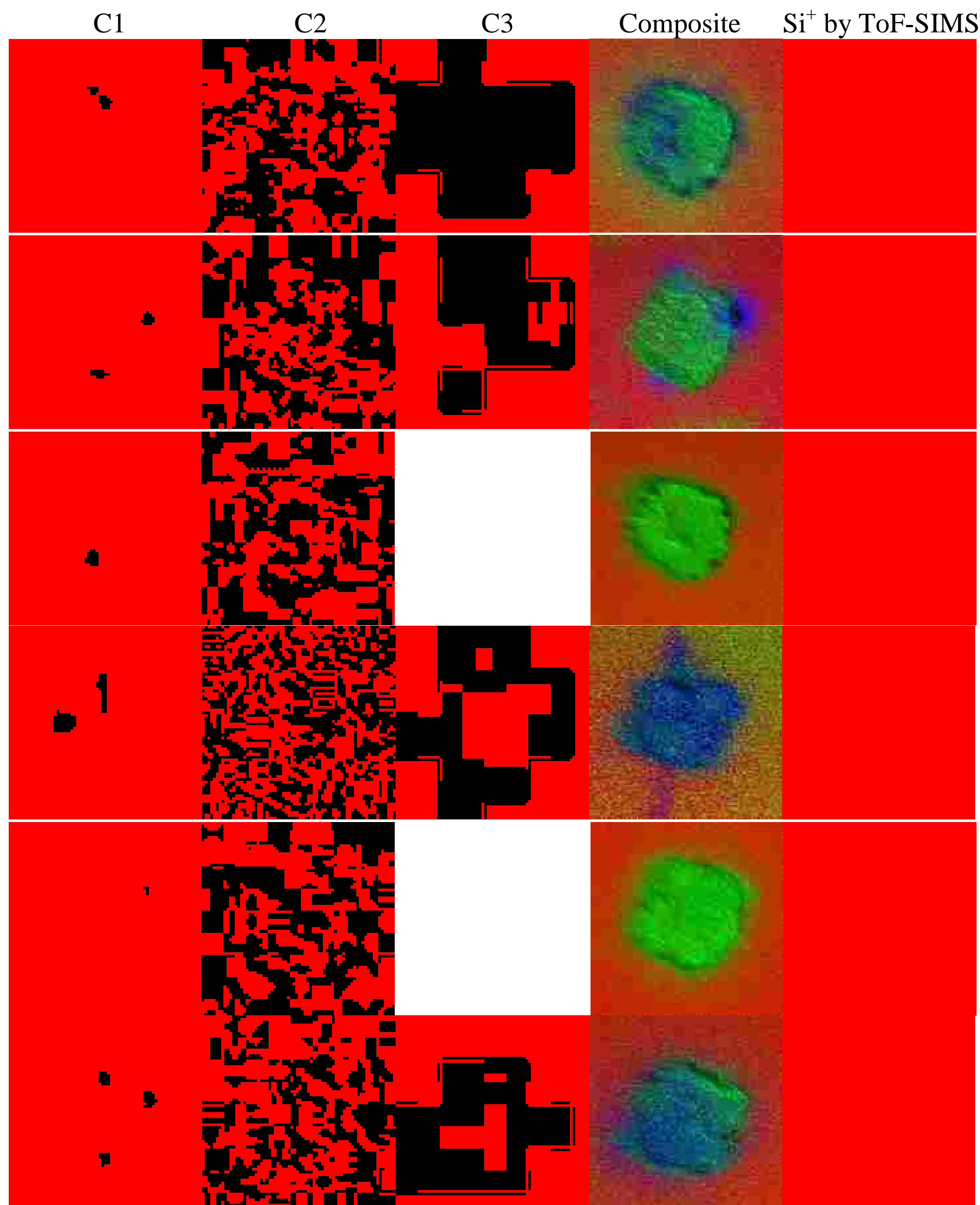

Figure 4.2. AXSIA images and Si^+ ToF-SIMS images taken from positive ion ToF-SIMS images of silicon surfaces modified by LAMSS with 1-hexene, 1-octene, 1-decene, 1-dodecene, 1-tetradecene and 1-hexadecene, respectively (from up to down).

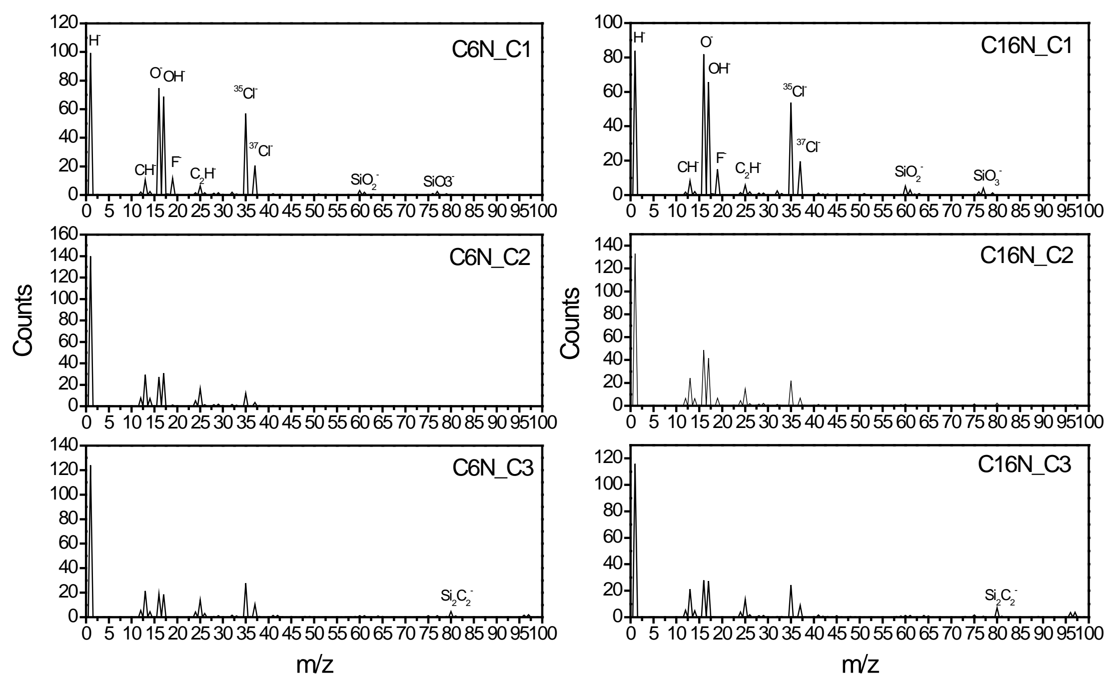

Figure 4.3. Negative-ion AXSIA component spectra of ToF-SIMS images of silicon surfaces modified with 1-hexene (left) and 1-hexadecene (right).

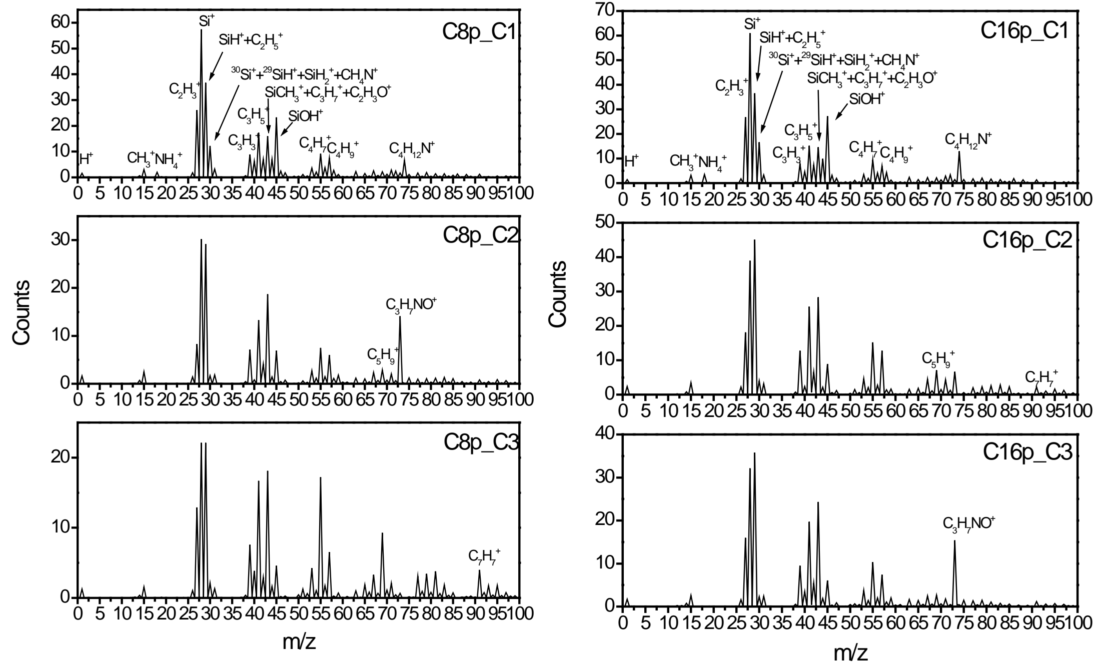

Figure 4.4. Positive-ion AXSIA component spectra of ToF-SIMS images of silicon surfaces modified with 1-octene (left) and 1-hexadecene (right).

While MCR does an excellent job of revealing the key spectral features of an image, it provides no obvious way to compare the results from separate MCR analyses of related images. To more fully understand the chemistry of LAMSS of silicon surfaces modified with different 1-alkenes, PCA analyses were conducted separately for negative and positive ion data matrices of the AXSIA component spectra from all of the different samples. To the best of my knowledge, this is the first report of an MCR/PCA analysis of related images. Figures 4.5 and 4.6 show the scores (left panel) and loadings (right panel) on the first principal components (PC1s) of the PCA analysis of negative and positive ion AXSIA component spectra, respectively. Note that the negative-ion PC1 captures over 82% of the total variance of the whole negative data matrix while the positive-ion PC1 captures over 70% of the total variance of the positive ion data. Thus, it is reasonable to focus the following discussions primarily on the PC1s of both PCA analyses.

In Figure 4.5, it is seen that all of the negative-ion C1 spectra have negative scores and form a cluster, while in contrast, all the negative-ion C2 spectra and C3 spectra, have positive scores and form another cluster on PC1. For two of the 1-alkenes studied, AXSIA found four components. The C4 from the 1-octene LAMSS spot resembles the C2 and C3 spectra of all of the adsorbates, and the C4 from the 1-dodecene LAMSS spot resembles C1 for all of the adsorbates (see Figure 4.5). The results in Figure 4.5 are again consistent with the results from the component images in Figure 4.1 and spectra in Figure 4.3. That is, these results confirm that all of the spectra from spots or backgrounds from all of the 1-alkene adsorbates are similar, and that spots and backgrounds have different surface chemistry. For a mean-centered data set, positive loadings of a PC are anti-correlated to negative loadings of the same PC, while either the positive or negative loadings are generally correlated with themselves. The positive peaks in

loadings plots are more intense in spectra that have positive scores in scores plots, and vice versa. Thus, these results indicate an organic functionalization of LAMSS spots (the C2 and C3 spectra), compared to a more inorganic background (the C1 spectra). The loading plot for PC1 in Figure 4.5 shows that, positive loadings on PC1 of C2 and C3 from the spot interiors come from organic peaks (H^-, C^-, CH^-, CH_2^-, C_2^-, C_2H^-, $Si_2C_2^-$, etc.) and negative loadings of C1 from the backgrounds come from inorganic peaks (O^-, OH^-, F^-, Cl^-, SiO_2^-, SiO_3^-, etc.).

Figure 4.6 shows basically the same results as in Figure 4.5 from the positive component data set. The C1 spectra (the backgrounds) cluster together and are different from the C2 and C3 spectra from the spots. In the loadings plot, the positive peaks correspond to the C1 spectra and have a significant inorganic character, while the negative peaks correspond to the C2 and C3 spectra and are organic in nature. The fact that the inorganic and organic peaks have opposite signs in the loadings plots in Figures 4.5 and 4.6 is irrelevant because of the sign ambiguity in PCA. That is, PCA represents the decomposition of a data matrix, S, into scores, T, and loadings, P, matrices as follows: $\mathbf{S} = \mathbf{TP}^T$, however, it is also true that $\mathbf{S} = (-\mathbf{T})(-\mathbf{P}^T)$.

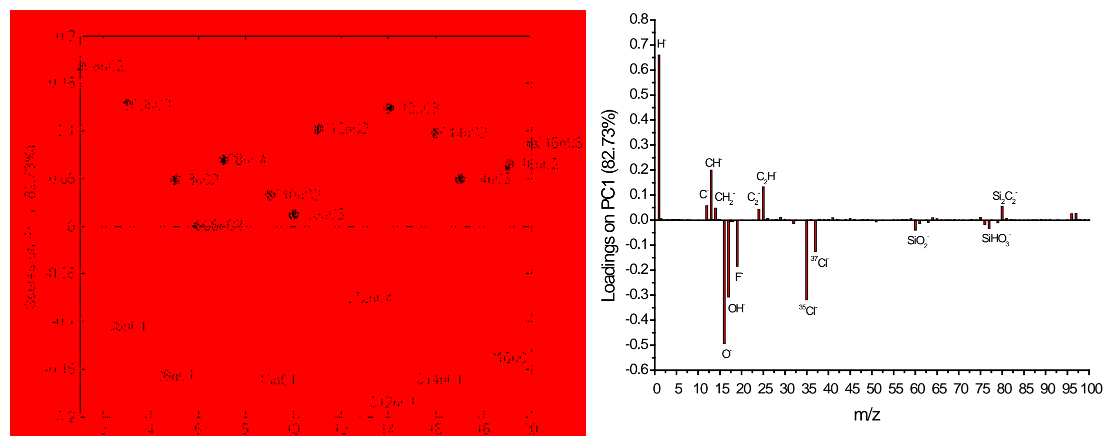

Figure 4.5. PCA analysis of negative-ion AXSIA component spectra of ToF-SIMS images of silicon surfaces modified by LAMSS using 1-alkenes with 6, 8, 10, 12, 14 and 16 carbon atoms.

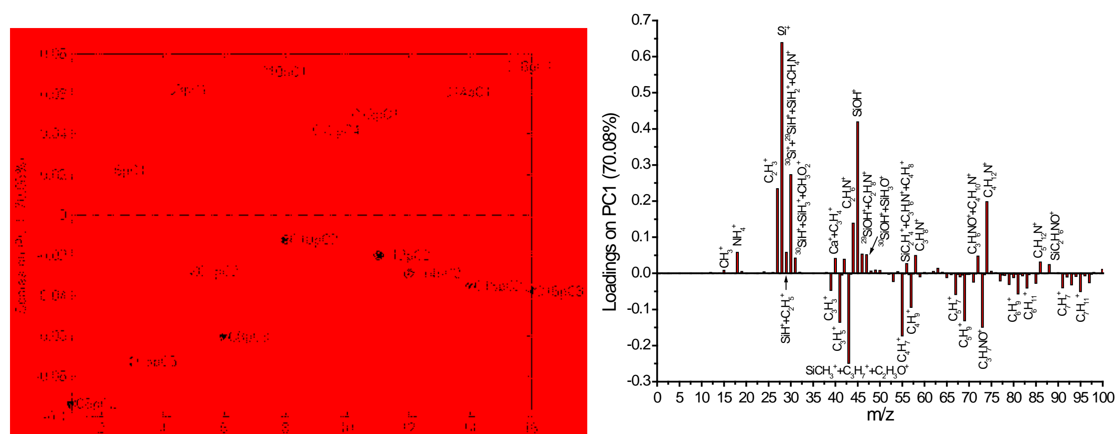

Figure 4.6. PCA analysis of positive ion AXSIA component spectra of ToF-SIMS images of silicon surfaces modified by LAMSS using 1-alkenes with 6, 8, 10, 12, 14 and 16 carbon atoms.

4.5.2 Comparison of AXSIA MCR and PLS_Toolbox MCR analyses, and cluster analysis

The results in section 4.5.1 of this chapter were obtained from LAMSS spots produced at high power densities. The data used in this section and also section 4.5.3 came from somewhat smaller LAMSS spots that were made at lower power densities. One of the important conclusions of this chapter is that significant improvements in spot quality can be obtained by optimizing the laser/optics of the system.

Unfortunately, the AXSIA toolkit is not yet commercially available. This limits the use of this data analysis tool to a select few in the ToF-SIMS community. I therefore felt it would be important to compare a few AXSIA MCR results to those obtained using the same data set in a commercially available chemometrics software package: the PLS_Toolbox, using the PLS_Toolbox's MCR algorithm.

AXSIA based MCR and PLS_Toolbox based MCR analyses were performed on the data set corresponding to the ToF-SIMS image shown in Figures 4.7 and 4.8. In the automated mode (used here), AXSIA uses Eigenvalue plots to define the number of non-noise components in the data (three in these data sets). The PLS_Toolbox based algorithm requires the user to enter the number of factors. I used three different methods to determine the number of factors (components) that should be kept in the MCR model. No preprocessing methods were applied to the data prior to MCR analysis, but the data were mean centered prior to PCA. I recently used a similar approach to determine the number of relevant factors in a complicated ToF-SIMS data set.[31] (Both MCR and PCA are factor-based methods that follow bilinear models, so they should have the same number of factors. Although I note that changing the preprocessing method can change the number of factors PCA needs to describe a data set, *e.g.*, mean centering typically

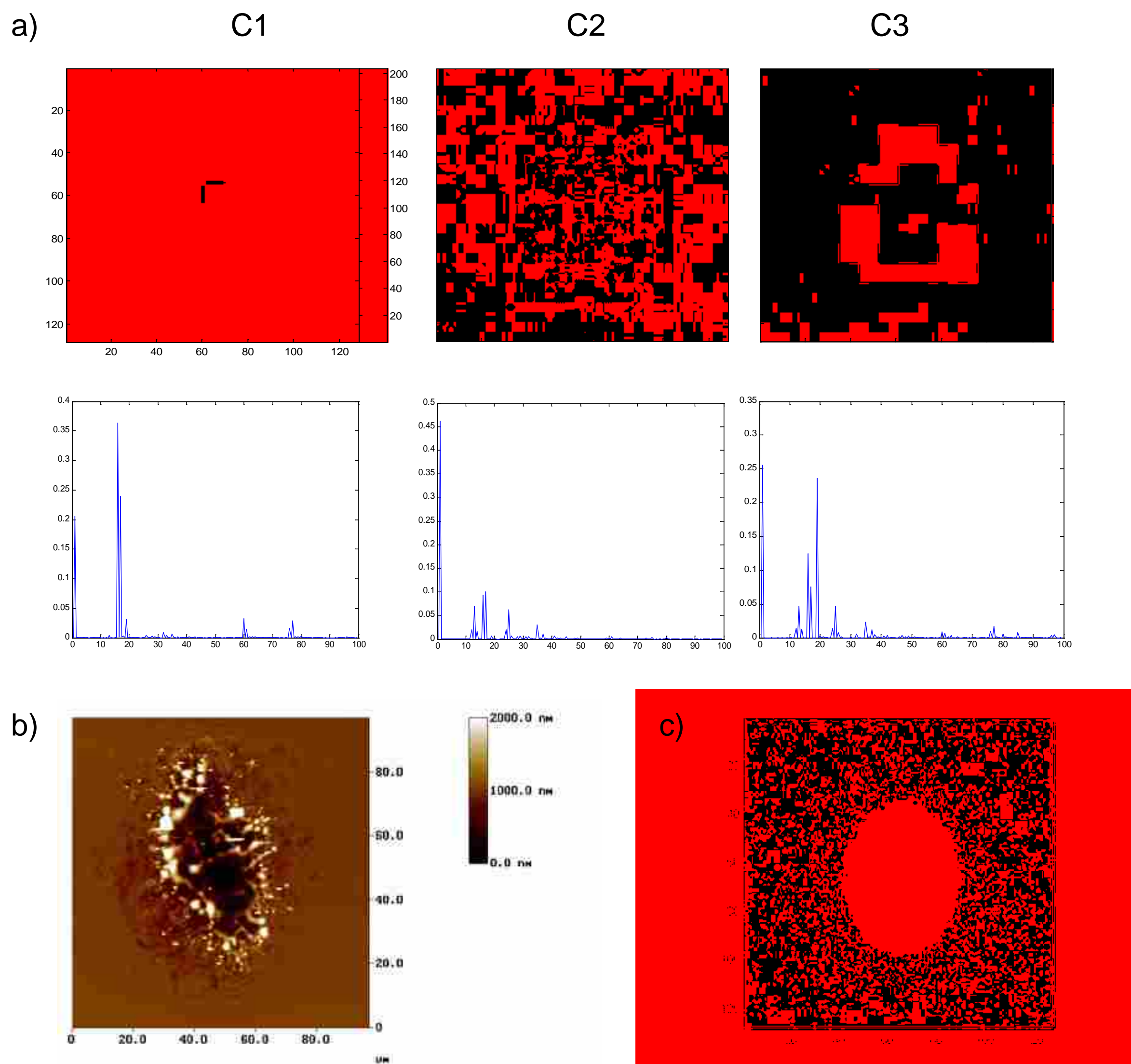

Figure 4.7. (a) Three AXSIA based single color MCR images and corresponding spectra, (b) an AFM image, and (c) the AXSIA C2 image on a different color scale. All data came from a single LAMSS spot made with 1-hexene.

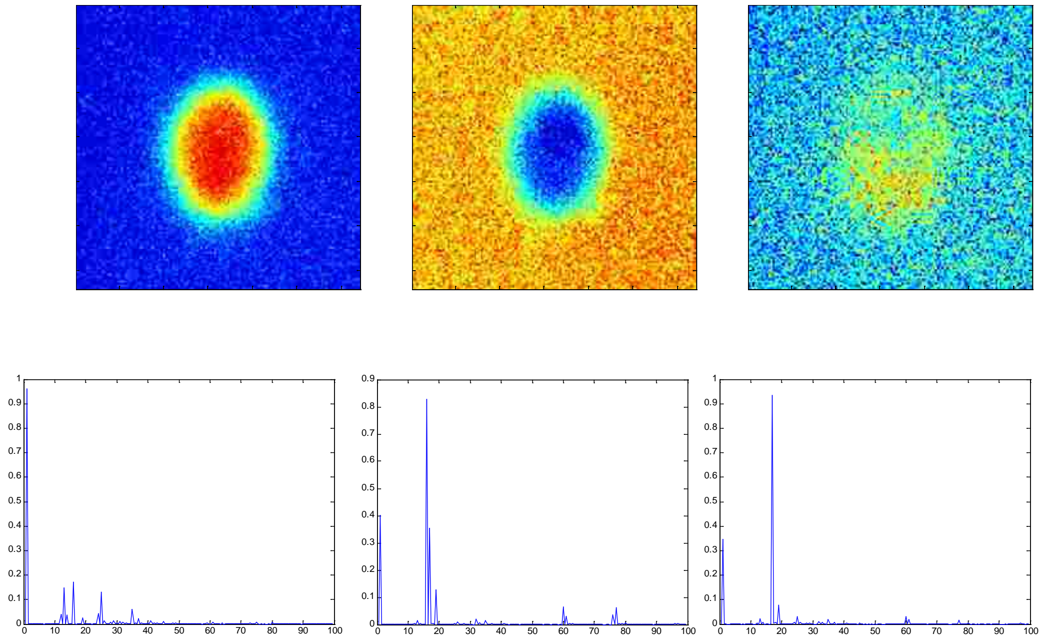

Figure 4.8. PLS_Toolbox based MCR component spectra and loadings of the ToF-SIMS image of the spot shown in Figure 4.7.

Table 4.1. Total percent variance captured for a certain number of MCR components or principal components by PCA for the data shown in Figure 4.7a.

	Total % variance captured	
Number of Components	MCR	PCA
1	17.68	78.52
2	85.50	85.73
3	90.29	90.53
4	92.41	92.49
5	93.43	93.54

removes approximately one significant factor.) First, I evaluated the percent variance captured per MCR component. Second, I evaluated the percent variance captured per PCA principal component. Third, I evaluated the cross-validation results for PCA, using a "Venetian Blinds" cross validation algorithm with 3, 5, 7, and 9 splits and 10 principal components in the PLS_Toolbox. Cross-validation in PCA is a well-established method that sometimes shows a minimum value that corresponds to the number of components in the data. Evaluation of the percent variance captured per factor in both MCR and PCA (see Table 4.1) indicated that a three-component model was appropriate for describing my data set. It is not uncommon for cross-validation to be inconclusive, as it was in this analysis. Failure of cross validation is most often the case for high signal-to-noise data with possible outliers – the PCA cross validation method works best when there are no outliers and noise of a high enough level that it is apparent when it is incorporated into the model. In summary, AXSIA based MCR and PLS_Toolbox based MCR analyses both indicate that three components describe the data set.

Figure 4.8 shows the results for the three-component PLS_Toolbox based MCR analysis of the data in Figure 4.7a. The three components account for 23.2%, 61.3%, and 5.8% of the variance in the data, which together is more than 90% of the total variance in the data. It is gratifying to see that the scores and loadings of the first two PLS_Toolbox based MCR components closely resemble the scores and loadings of the first two AXSIA based MCR analysis components. (I deliberately did not change the order of the AXSIA and MCR PLS_Toolbox components in Figures 4.7 and 4.8 to call attention to the reader that these components are not always ordered the same in the different analyses.) The third MCR component, which accounts for the smallest amount of variance in the MCR data, differs for AXSIA and PLS_Toolbox based MCR analyses. It is important to point out that within AXSIA,

the ToF-SIMS data are scaled to account for Poisson statistics, where the estimated standard deviation of a measurement equals the square root of the measurement itself. It has been shown that optimal scaling of ToF-SIMS data requires accounting for the Poisson nature of the data, e.g., weighting each element appropriately for its particular uncertainty.[32-33] Optimal scaling provides maximum discrimination of chemical information from noise, and allows small features to be detected that would be otherwise overlooked. The PLS_Toolbox also allows scaling of the data to account for Poisson statistics through its "Sqrt Mean Scale" method in its custom preprocessing options, although this method was not used in this work. Most of the minor differences in the two MCR methods can be attributed to the scaling. While this comparison of AXSIA and MCR does not constitute an exhaustive or mathematically rigorous analysis of the two methods, this particular comparison does suggest that with reasonable selection of the number of pure components (factors) by the user, very similar information can be obtained from the two methods.

Whenever MCR and PCA are performed on data, it is valuable to examine the errors associated with these models. The Q Residual errors show the deviations of the data points (spectra) outside the model, and the Hotelling T^2 errors show the deviations of the data points (spectra) within the model. The PLS_Toolbox only provides the Q Residual errors for the MCR analysis because Hotelling's T^2 is not defined for non-orthogonal (oblique) components like those found in MCR models. The errors from the PCA model are discussed here because, as noted above, MCR and PCA are both factor-based methods that follow bilinear models, so they should have the same number of factors, i.e., the ability or inability of these methods to describe the data should be similar. The ToF-SIMS images collected for this paper contain 128 x 128 pixels, or 16,384 pixels, with a full mass spectrum at each pixel. With such a large number of

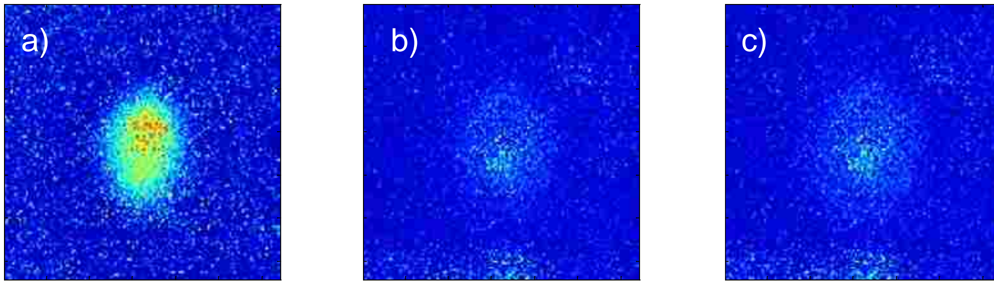

Figure 4.9. (a) Hotelling T^2 analysis/errors (95% confidence limit = 7.82) and (b) Q Residual analysis/errors (95% confidence limit = 105) of the PCA analysis of the data shown in Figure 4.7. (c) Q Residual analysis/errors of the MCR analysis shown in Figure 4.8 (95% confidence limit = 109).

data points, it becomes likely that 5% of the data points really should fall outside of the 95% confidence limit for the Q Residual and Hotelling T^2 statistical tests. For the three statistical tests shown in Figure 4.9 (a, b, and c), 8.5%, 7.0%, and 7.1% of the data points fall outside of the 95% confidence limits, respectively. The fact that these values exceed 5% led me to wonder whether the data points with the largest errors were evenly distributed over the images, or whether they were clustered into certain parts of the images. Plots of the Hotelling T^2 and Q Residual values are shown in Figure 4.9. It is clear from these images that the outliers are concentrated in the LAMSS spots. This suggests that neither MCR, nor PCA, is entirely adequate for describing these data.

In light of the above, I considered yet another chemometrics method for analyzing our data: cluster analysis. I performed cluster analysis in the MIA_Toolbox for Matlab. In cluster analysis, the criterion for separation of data points (spectra) is the distances between them in a hyperspace. In addition, it is my view that my conclusions are strengthened if I apply different statistical tools that use different underlying mathematics to my data because different statistical methods respond differently to variances in data sets. Figure 4.10 shows the results of using two clusters for my data. It is clear that cluster analysis separates the LAMSS spot from background. The average spectra for the interior and exterior regions bear some similarity to the average spectra for the MCR analyses shown in Figures 4.7 and 4.8. A key similarity between these analyses is that the H:O and C:O ratios are clearly higher in the LAMSS spot than they are in the background region (see Table 4.2). Figure 4.11 shows the image that separates the data in Figure 4.7 into three clusters. It is noteworthy that cluster analysis shows a ring (green) around a central spot that is consistent with the gradient in functionalization suggested in the MCR analyses in Figures 4.7 and 4.8. Table 4.2 again shows that as one proceeds from the center of the LAMSS

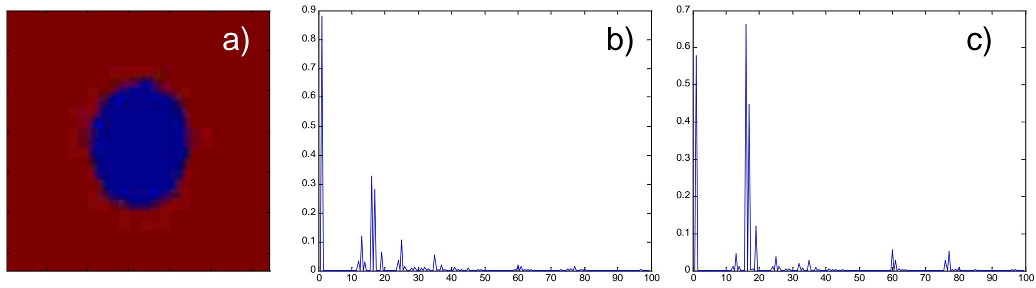

Figure 4.10. (a) Image of the two-cluster analysis of the data shown in Figures 4.7 and 4.8, and average spectra corresponding to the (b) blue, and (c) red pixels.

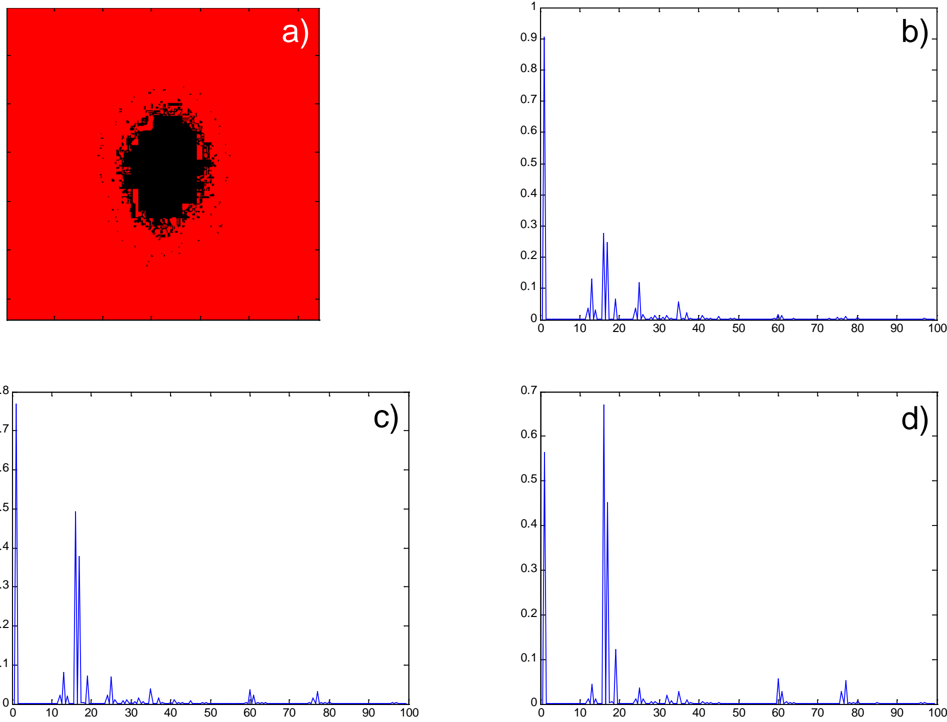

Figure 4.11. (a) Image of the three-cluster analysis of the data shown in Figures 4.7 and 4.8, and average spectra corresponding to the (b) blue, (c) green, and (d) red pixels.

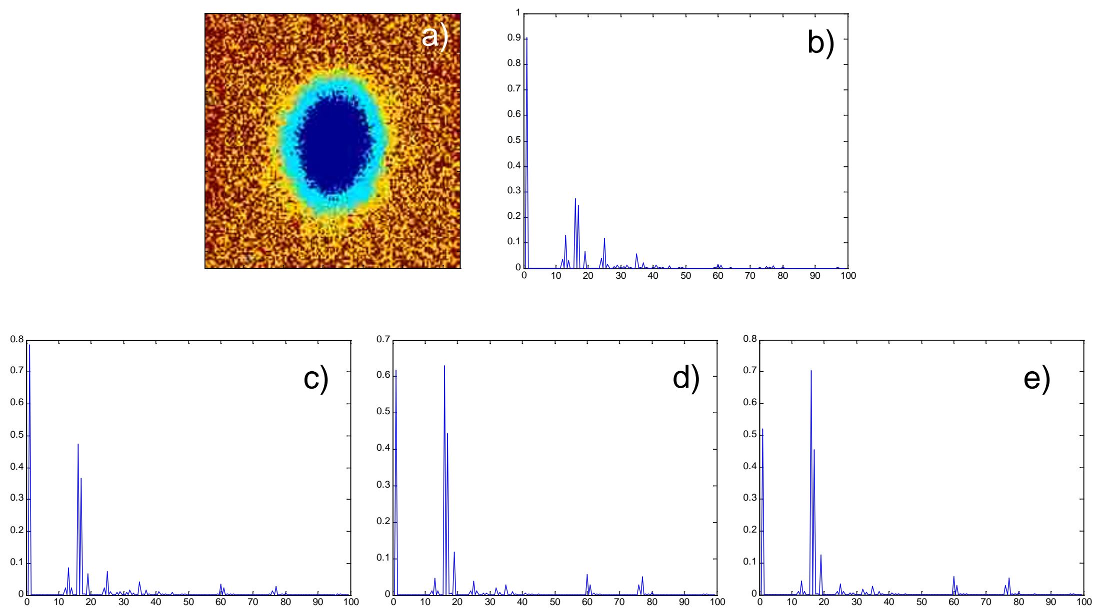

Figure 4.12. (a) Image of the four-cluster analysis of the data shown in Figures 4.7 and 4.8, and average spectra corresponding to the (b) dark blue, (c) light blue, (d) yellow, and (e) red pixels.

Table 4.2 H:O and C:O ratios for the cluster images shown in Figures 4.10 – 4.12.

	Color in Image	H:O ratio	C:O ratio
2 clusters			
	blue	2.7	0.37
	red	0.87	0.069
3 clusters			
	blue	3.3	0.48
	green	1.56	0.16
	red	0.84	0.066
4 clusters			
	dark blue	3.3	0.48
	light blue	1.7	0.18
	yellow	0.98	0.074
	red	0.74	0.060

spot to its exterior, the H:O and C:O ratios decrease, which is again consistent with chemical functionalization in the LAMSS spot and a radial decrease in functionalization as one moves away from the center of the spot. These trends continue for a four-cluster analysis of the data (see Figure 4.12). A ring-like structure (dark blue, light blue, then yellow) is again apparent for the data, and the H:O and C:O ratios again decrease moving out from the center of the LAMSS spot (see Table 4.2).

4.5.3 AFM

A subset of the LAMSS spots that were analyzed by ToF-SIMS was also imaged by atomic force microscopy (AFM). A representative AFM image is shown in Figure 4.7, which demonstrates that these spots are rather rough. Given the roughness of these spots, it was of interest to know the degree to which the ToF-SIMS results depend on the surface morphology. Analysis of a number of spots has let me to conclude that the surface morphology is not closely related to the surface chemistry. That is, Figure 4.7 shows both an AFM image and a plot of the second AXSIA component, which corresponds to the surface chemistry at the spot (see also Figures 4.8 – 4.12). As noted, the degree of functionalization at the surface decreases smoothly and radially from the center of the spot. This is consistent with a decrease in surface temperature from the center of the spot during functionalization. The ToF-SIMS analysis of this surface does not appear to be strongly affected by the surface morphology. That is, one might have expected that higher or lower regions in the spot would have been affected to a larger or smaller extent during surface modification but this appears not to be the case. The primary factor determining surface chemistry appears to be distance from the center of the spot.

4.6 Conclusions

AXSIA-MCR analysis followed by PCA analysis of the AXSIA component spectra of the ToF-SIMS imaging of silicon surfaces modified with 1-alkenes by LAMSS effectively reveals the chemical variations between a related set of samples. These results provide additional evidence for silicon surface modification by LAMSS, as well as a successful example of combining AXSIA and PCA multivariate analysis methods in ToF-SIMS image data. This analysis shows that there are significant chemical similarities between all of the LAMSS spots made with the different 1-alkenes. A comparison of AXSIA based MCR and PLS_Toolbox based MCR showed that essentially the same information can be obtained using either method. It is significant that LAMSS spots can be made that have surface chemistry that varies radially from the center of the spot, as shown by AXSIA based MCR, PLS_Toolbox based MCR, and cluster analysis. AFM and ToF-SIMS images were compared and show that surface chemistry and morphology in LAMSS spots are only weakly correlated.

4.7 References

1. Vickerman, J. C.; Briggs, D., *ToF-SIMS: surface analysis by mass spectrometry*. IM: Chichester, 2001.

2. Mowat, I. A.; Lindley, P. M.; Reich, F., Polymer surface analysis using time-of-flight secondary ion mass spectrometry (TOF-SIMS). *Abstr. Pap. Am. Chem. Soc.* **1998,** *215*, U298-U298.

3. Peterson, R. E.; Tyler, B. J., Analysis of organic and inorganic species on the surface of atmospheric aerosol using time-of-flight secondary ion mass spectrometry (TOF-SIMS). *Atmos. Environ.* **2002,** *36* (39-40), 6041-6049.

4. Sodhi, R. N. S., Time-of-flight secondary ion mass spectrometry (TOF-SIMS): versatility in chemical and imaging surface analysis. *Analyst* **2004,** *129* (6), 483-487.

5. Wagner, M. S.; Graham, D. J.; Ratner, B. D.; Castner, D. G., Maximizing information obtained from secondary ion mass spectra of organic thin films using multivariate analysis. *Surf. Sci.* **2004,** *570* (1-2), 78-97.

6. Wagner, M. S.; Pasche, S.; Castner, D. G.; Textor, M., Characterization of poly(L-lysine)-graft-poly(ethylene glycol) assembled monolayers on niobium pentoxide substrates using time-of-flight secondary ion mass spectrometry and multivariate analysis. *Anal. Chem.* **2004,** *76* (5), 1483-1492.

7. Brereton, R. G., *Chemometrics: data analysis for the laboratory and chemical plant*. Wiley: Chichester, 2003.

8. Massart, D. L., *Chemometrics: a textbook*. Elsevier: Amsterdam; Oxford, 1988.

9. Smentkowski, V. S.; Ostrowski, S. G.; Kollmer, F.; Schnieders, A.; Keenan, M. R.; Ohlhausen, J. A.; Kotula, P. G., Multivariate statistical analysis of non-mass-selected ToF-SIMS data. *Surf. Interface Anal.* **2008,** *40* (8), 1176-1182.

10. Keenan, M. R.; Smentkowski, V. S.; Ohlhausen, J. A.; Kotula, P. G., Mitigating dead-time effects during multivariate analysis of ToF-SIMS spectral images. *Surf. Interface Anal.* **2008,** *40* (2), 97-106.

11. Smentkowski, V. S.; Ostromiski, S. G.; Braunstein, E.; Keenan, M. R.; Ohlhausen, J. A. T.; Kotula, P. G., multivariate statistical analysis of three-spatial-dimension TOF-SIMS raw data sets. *Anal. Chem.* **2007,** *79* (20), 7719-7726.

12. Smentkowski, V. S.; Duong, H. M.; Tamaki, R.; Keenan, M. R.; Ohlhausen, J. A. T.; Kotula, P. G., Using time-of-flight secondary ion mass spectrometry and multivariate statistical analysis to detect and image octabenzyl-polyhedral oligomeric silsesquioxane in polycarbonate. *Appl. Surf. Sci.* **2006,** *253* (2), 1015-1022.

13. Graham, D. J.; Ratner, B. D., Multivariate analysis of TOF-SIMS spectra from dodecanethiol SAM assembly on gold: Spectral interpretation and TOF-SIMS fragmentation processes. *Langmuir* **2002,** *18* (15), 5861-5868.

14. Yang, L.; Lua, Y. Y.; Jiang, G. L.; Tyler, B. J.; Linford, M. R., Multivariate analysis of TOF-SIMS spectra of monolayers on scribed silicon. *Anal. Chem.* **2005,** *77* (14), 4654-4661.

15. Zhang, F.; Pei, L.; Bennion, E.; Jiang, G. L.; Connley, D.; Yang, L.; Lee, M. V.; Davis, R. C.; Smentkowski, V. S.; Strossman, G.; Linford, M. R.; Asplund, M. C., Laser activation modification of semiconductor surfaces (LAMSS). *Langmuir* **2006,** *22* (26), 10859-10863.

16. Keenan, M. R.; Kotula, P. G. U.S. Patent 6,584,413, 2003.

17. Keenan, M. R.; Kotula, P. G. U.S. Patent 6,675,106, 2004.

18. Ohlhausen, J. A. T.; Keenan, M. R.; Kotula, P. G.; Peebles, D. E., Multivariate statistical analysis of time-of-flight secondary ion mass spectrometry images using AXSIA. *Appl. Surf. Sci.* **2004,** *231-2*, 230-234.

19. Smentkowski, V. S.; Ohlhausen, J. A.; Kotula, P. G.; Keenan, M. R., Multivariate statistical analysis of time-of-flight secondary ion mass spectrometry images-looking beyond the obvious. *Appl. Surf. Sci.* **2004,** *231-2*, 245-249.

20. Smentkowski, V. S.; Keenan, M. R.; Ohlhausen, J. A.; Kotula, P. G., Multivariate statistical analysis of concatenated time-of-flight secondary ion mass spectrometry spectral images. Complete description of the sample with one analysis. *Anal. Chem.* **2005,** *77* (5), 1530-1536.

21. Magonov, S. N.; Whangbo, M.-H., *Surface analysis with STM and AFM: experimental and theoretical aspects of image analysis*. VCH: Weinheim; Cambridge, 1996.

22. Skoog, D. A.; Holler, F. J.; Nieman, T. A., *Principles of instrumental analysis*. 5th ed.; Harcourt Brace College Publishers: Philadelphia, 1998.

23. Kramer, R., *Chemometric techniques for quantitative analysis*. Marcel Dekker: New York, 1998.

24. Otto, M., *Chemometrics: statistics and computer application in analytical chemistry*. 2nd rev. ed. ed.; Wiley-VCH; Chichester John Wiley [distributor]: Weinheim, 2007.

25. Jackson, J. E., *A user's guide to principal components*. Wiley: 1991.

26. Jolliffe, I. T., *Principal component analysis*. Springer-Verlag: New York, 1986.

27. Aldenderfer, M. S.; Blashfield, R. K., *Cluster analysis*. Sage Publications: Beverly Hills, 1984.

28. Vickerman, J. C.; Gilmore, I. S., *Surface analysis: the principal techniques*. 2nd ed.; Wiley: Chichester, 2009.

29. Esposito Vinzi, V., *Handbook of partial least squares: concepts, methods and applications*. Springer: Berlin; London, 2010.

30. Gallagher, N. B.; Shaver, J. M.; Martin, E. B.; Morris, J.; Wise, B. M.; Windig, W., Curve resolution for multivariate images with applications to TOF-SIMS and Raman. *Chemom. Intell. Lab. Syst.* **2004,** *73* (1), 105-117.

31. Yang, L.; Shirahata, N.; Saini, G.; Zhang, F.; Pei, L.; Asplund, M. C.; Kurth, D. G.; Ariga, K.; Sautter, K.; Nakanishi, T.; Smentkowski, V.; Linford, M. R., Effect of surface free energy on PDMS transfer in microcontact printing and its application to ToF-SIMS to probe surface energies. *Langmuir* **2009,** *25* (10), 5674-5683.

32. Keenan, M. R.; Kotula, P. G., Optimal scaling of TOF-SIMS spectrum-images prior to multivariate statistical analysis. *Appl. Surf. Sci.* **2004,** *231-2*, 240-244.

33. Keenan, M. R.; Kotula, P. G., Accounting for Poisson noise in the multivariate analysis of ToF-SIMS spectrum images. *Surf. Interface Anal.* **2004,** *36* (3), 203-212.

Chapter 5 Time-of-Flight Secondary Ion Mass Spectrometry of a Range of Coal Samples: A Chemometrics (PCA, Cluster, and PLS) Analysis

5.1 Abstract

This paper documents ToF-SIMS analyses of 34 different coal samples. In many cases, the inorganic Na^+, Al^+, Si^+, and K^+ ions dominate the spectra, eclipsing the organic peaks. A score plot of principal component 1 (PC1) vs. principal component 2 (PC2) in a principal components analysis (PCA) effectively separates the coal spectra into a triangular pattern, where the different vertices of this pattern come from (1) spectra that have a strong inorganic signature that is dominated by Na^+, (2) spectra that have a strong inorganic signature that is dominated by Al^+, Si^+, and K^+, and (3) spectra that have a strong organic signature. Loadings plots of PC1 and PC2 confirm these observations. The spectra with the more prominent inorganic signatures come from samples with higher ash contents. Cluster analysis with the K-means algorithm was also applied to the data. The progressive clustering revealed in the dendrogram correlates extremely well with the clustering of the data points found in the score plot of PC1 vs. PC2 from the principal components analysis. In addition, this clustering often correlates with properties of the coal samples, as measured by traditional analyses. Partial least squares (PLS), which included the use of interval PLS and a genetic algorithm for variable selection, shows a good correlation between ToF-SIMS spectra and some of the properties measured by traditional means. Thus, ToF-SIMS appears to be a promising technique for analysis of this important fuel.

5.2 Introduction

Time-of-flight secondary ion mass spectrometry (ToF-SIMS) is a versatile analytical method that has been successfully applied to a wide variety of surfaces and materials.[1-5] In ToF-SIMS, a primary ion beam is directed onto a surface. The secondary ions that are generated by

surface bombardment with these primary ions are mass analyzed. In general, the secondary ions contain a significant amount of chemical information about the original material.

Traditional fuel analyses characterize coal elemental composition for both the organic (C, H, O, N, S) and ash-forming inorganic (Si, Al, Fe, Ti, Na, K, Ca, Mg, S, P) compounds, the heat of combustion, the moisture content, the softenting/melting behavior under both reducing and oxidizing conditions, and the extent of thermal decomposition under standardized conditions. This study uses all of these data for the samples under investigation (see Tables 5.1 – 5.3). Among these measurements, only the moisture relates directly to a chemical species (as opposed to an element), making it difficult to anticipate the thermal decomposition and chemical reactions fuels undergo in practice. These complex, commonly multiphase reactions depend directly on speciation and chemical functionality of the fuels, characteristics that cannot always be surmised based on elemental compositions. The focus of this work was to determine the extent to which advanced characterization techniques provide additional information that allows more accurate characterization of these reactions.

Table 5.1. Standard organic and combustion characterizations (proximate, ultimate, heating value, rank, etc.) and cluster for each coal sample.

Sample	Cluster	H_2O (Wt%)	VM (Wt%)	FC (Wt%)	ASH (Wt%)	C (Wt%)	H (Wt%)
GAT-034	4	2.04	34.02	61.91	14.23	71.17	4.59
GAT-035	4	4.53	34.83	58.04	12.40	73.24	4.56
RLL-012	3	2.03	33.69	61.17	14.72	71.64	4.51
RLL-014	1,3,7	2.60	35.74	58.03	10.44	75.17	4.80
PCT-010	4,5,5	3.11	35.90	58.11	11.01	74.01	4.52
JIG-014	3	3.63	35.24	59.22	8.29	77.39	4.53
JIG-017	3,3,4	2.88	35.20	59.85	10.73	74.46	4.41
CJR-012	7	1.91	35.87	60.34	9.59	75.75	4.82
GBJ-010	7	2.07	35.13	57.70	8.63	77.12	4.35
GLJ-005	3,3,4	1.88	35.83	59.36	9.95	75.70	4.95
HGB-011	4	5.10	35.13	57.82	13.10	70.42	4.31
HNA-015	4,4,5	2.93	35.61	58.03	9.80	74.17	4.78
RBL-014	7	1.95	35.03	59.75	10.44	75.74	4.74
PCT-012	4	3.43	34.43	60.20	12.77	72.96	4.64
GPB-062	4,4,5	3.27	34.27	61.98	15.39	69.30	4.42
SS-1	5	1.94	30.49	61.83	17.65	68.82	4.29
SS-2	2,3,3	0.48	19.88	78.81	9.19	81.97	4.19
SS-3	4,5,5	5.74	32.22	61.05	14.98	70.84	4.46
SS-4	2,7,7	0.83	24.77	73.37	12.75	77.08	4.36
SS-5	5	0.99	29.26	68.15	13.06	73.92	4.45
SS-6	4	1.03	31.34	66.74	8.31	79.24	4.84
SS-7	2,5,7	1.60	34.30	63.47	12.94	73.15	4.76
SS-8	1	0.89	25.49	72.91	13.76	75.72	4.26
SS-9	7	0.63	20.43	58.82	13.29	77.78	4.04
SS-10	2,7,7	0.71	19.43	60.47	14.30	76.27	3.88
SS-11	1,6,6	20.12	48.92	10.04	8.21	68.85	4.86
SS-12	3,7,7	19.39	43.85	16.58	7.31	69.46	4.40
SS-13	6	20.92	46.72	11.75	5.88	70.37	4.34
SS-14	6	20.18	46.67	29.22	5.59	69.97	4.47
SS-15	6	20.61	47.00	26.38	6.86	67.91	4.34
SS-16	5	3.93	40.62	53.22	5.02	75.31	5.10
SS-17	1	6.01	35.24	54.64	6.94	76.95	4.86
SS-18	1,1,5	2.23	38.81	58.96	7.94	75.20	5.18
SS-19	1	4.11	39.15	56.74	10.01	72.95	4.96

Table 5.1. continued.

Sample	N (Wt%)	S (Wt%)	HHV (MJ/kg)	Cl (Wt%)	O (Wt%)	Rank	H:C	O:C
GAT-034	1.47	1.09	29.18	0.10	7.35	mv bit	0.08	0.77
GAT-035	1.48	0.96	29.94	0.09	7.27	mv bit	0.07	0.74
RLL-012	1.57	0.83	29.35	0.15	6.58	mv bit	0.07	0.75
RLL-014	1.64	0.92	31.07	0.16	6.87	hvA bit	0.07	0.76
PCT-010	1.49	1.19	30.61	0.10	7.68	hvA bit	0.08	0.73
JIG-014	1.74	0.82	31.73	0.02	7.21	hvA bit	0.07	0.70
JIG-017	1.76	1.23	30.71	0.02	7.39	mv bit	0.07	0.71
CJR-012	1.72	1.20	31.64	0.01	6.91	hvA bit	0.07	0.76
GBJ-010	1.66	0.98	31.87	0.19	7.07	hvA bit	0.07	0.67
GLJ-005	1.65	0.89	31.27	0.16	6.70	hvA bit	0.07	0.78
HGB-011	1.48	1.21	28.92	0.06	9.42	hvB bit	0.10	0.73
HNA-015	1.70	1.36	30.69	0.02	8.17	hvA bit	0.08	0.77
RBL-014	1.57	1.12	31.18	0.18	6.21	hvA bit	0.06	0.75
PCT-012	1.47	0.90	29.95	0.10	7.16	mv bit	0.07	0.76
GPB-062	1.44	0.94	28.22	0.04	8.47	hvB bit	0.09	0.76
SS-1	1.46	1.55	28.04	0.01	6.22	mv bit	0.07	0.74
SS-2	1.67	0.52	33.07	0.01	2.45	Semianth	0.02	0.61
SS-3	1.44	1.65	29.02	0.02	6.61	hvB bit	0.07	0.75
SS-4	1.70	0.68	31.35	0.02	3.41	lv bit	0.03	0.67
SS-5	1.63	1.40	30.21	0.03	5.51	lv bit	0.06	0.72
SS-6	1.68	0.64	32.26	0.07	5.22	mv bit	0.05	0.73
SS-7	1.61	1.75	30.27	0.02	5.77	mv bit	0.06	0.78
SS-8	1.53	0.81	30.88	0.02	3.90	lv bit	0.04	0.67
SS-9	1.35	0.87	31.31	0.01	2.66	hvA bit	0.03	0.62
SS-10	1.53	0.64	30.98	0.02	3.36	mv bit	0.03	0.61
SS-11	0.96	1.11	28.44	<0.01	16.01	subbit B	0.17	0.84
SS-12	1.00	0.32	27.79	<0.01	17.51	subbit C	0.19	0.75
SS-13	0.83	0.30	27.99	<0.01	18.28	subbit C	0.20	0.73
SS-14	0.88	0.25	28.06	0.01	18.83	subbit C	0.20	0.76
SS-15	0.84	0.37	24.75	<0.01	19.68	lignite A	0.22	0.76
SS-16	1.42	0.62	30.88	<0.01	12.53	hvB bit	0.12	0.81
SS-17	1.71	1.14	31.72	0.47	7.93	hvB bit	0.08	0.75
SS-18	1.63	0.43	30.89	0.02	9.60	hvA bit	0.10	0.82
SS-19	1.67	0.58	30.14	0.01	9.82	hvB bit	0.10	0.81

Table 5.2. Standard inorganic fuel characterization for each sample.

Sample	Ash Elementals (based on 750 °C ash)									
	SiO_2	Al_2O_3	TiO_2	Fe_2O_3	CaO	MgO	Na_2O	K_2O	P_2O_5	SO_3
GAT-034	56.77	28.30	1.32	6.93	1.19	1.04	0.24	2.62	0.23	1.38
GAT-035	58.53	27.68	1.56	5.55	1.23	0.83	0.24	2.19	0.38	1.51
RLL-012	58.08	26.94	1.11	7.31	1.04	1.32	0.37	3.66	0.16	1.24
RLL-014	57.17	27.90	1.29	7.20	1.11	0.93	0.61	2.41	0.12	1.28
PCT-010	56.35	27.19	1.32	9.29	1.52	0.90	0.27	2.26	0.32	1.65
JIG-014	51.30	30.24	1.40	7.89	2.24	1.19	0.39	3.06	1.42	1.52
JIG-017	49.35	27.95	1.45	12.24	2.17	1.20	0.34	2.83	1.14	1.80
CJR-012	54.14	26.05	1.39	9.61	1.30	0.96	0.67	2.40	0.18	1.46
GBJ-010	52.70	28.92	1.46	8.77	1.44	0.79	0.50	1.99	0.19	1.32
GLJ-005	55.01	27.01	1.24	8.52	1.34	1.05	0.42	2.59	0.27	1.48
HGB-011	56.30	28.41	1.44	6.72	0.93	0.82	0.20	2.28	0.51	1.20
HNA-015	44.72	25.79	1.16	18.90	1.86	1.11	0.30	2.46	1.13	1.99
RBL-014	53.21	28.95	1.43	10.03	1.46	0.80	0.41	2.12	0.26	1.44
PCT-012	57.26	28.52	1.50	5.19	1.35	0.84	0.23	2.18	0.34	1.39
GPB-062	59.32	28.24	1.55	4.41	0.76	0.74	0.18	2.20	0.32	0.88
SS-1	48.12	27.24	1.31	10.01	2.85	1.20	0.41	2.85	0.76	3.15
SS-2	50.50	33.79	1.58	5.28	3.73	1.01	0.40	1.93	1.16	2.44
SS-3	50.95	27.67	1.20	12.32	1.03	1.10	0.29	2.59	0.56	1.20
SS-4	49.97	27.82	1.33	7.16	3.54	1.55	0.98	2.34	0.87	2.42
SS-5	50.32	25.87	1.18	12.81	1.80	1.21	0.47	2.63	0.50	2.28
SS-6	54.65	33.23	1.62	3.50	0.84	0.74	0.31	2.47	0.86	0.51
SS-7	42.52	26.71	1.19	14.36	4.93	1.36	0.64	2.48	0.87	3.67
SS-8	50.18	26.43	1.34	9.37	3.08	1.47	0.70	2.61	0.80	2.14
SS-9	48.08	29.63	1.38	7.96	3.68	1.34	0.39	2.62	0.96	2.37
SS-10	50.12	28.54	1.36	6.90	4.05	1.33	0.64	2.42	0.69	2.02
SS-11	26.21	14.94	0.85	8.34	19.88	3.29	1.12	0.35	0.78	22.06
SS-12	38.77	16.61	0.91	5.24	17.83	4.84	1.17	0.65	1.83	9.49
SS-13	28.91	13.77	1.29	5.90	26.50	6.09	2.14	0.22	1.31	11.91
SS-14	30.63	15.89	1.31	5.49	24.75	5.67	1.98	0.32	1.27	12.24
SS-15	37.57	15.48	1.14	5.87	21.00	4.27	1.27	0.50	0.86	12.02
SS-16	56.81	23.74	0.91	7.55	2.48	1.15	0.68	1.33	0.24	3.32
SS-17	53.54	23.88	1.23	11.44	2.41	1.08	1.16	2.74	0.65	2.35
SS-18	54.86	26.58	0.98	6.42	3.69	1.15	1.33	1.96	0.64	2.09
SS-19	56.28	26.81	0.93	5.13	3.67	1.50	2.04	1.00	0.64	1.64

Table 5.3. Standard ash fusion temperatures for each sample.

Sample	Ash Fusion (°C)							
	Reducing				Oxidizing			
	INITIAL	H=W	H=1/2W	FLUID	INITIAL	H=W	H=1/2W	FLUID
GAT-034	1477	1519	1553	1586	1551	1578	1592	1599
GAT-035	1504	1538	1566	1596	1571	1591	1604	1616
RLL-012	1449	1479	1503	1535	1513	1539	1554	1567
RLL-014	1504	1529	1541	1565	1553	1576	1592	1600
PCT-010	1439	1469	1489	1518	1524	1542	1549	1565
JIG-014	1437	1469	1503	1532	1526	1539	1554	1566
JIG-017	1391	1416	1432	1459	1472	1499	1518	1531
CJR-012	1438	1460	1493	1513	1506	1529	1550	1575
GBJ-010	1524	1537	1548	1574	1550	1573	1583	1594
GLJ-005	1486	1516	1526	1551	1524	1551	1566	1577
HGB-011	1492	1516	1549	1566	1571	1592	1596	1611
HNA-015	1169	1261	1335	1371	1392	1423	1454	1462
RBL-014	1477	1499	1508	1530	1532	1553	1566	1574
PCT-012	1591	1602	1609	1624	1587	1606	1613	1621
GPB-062	1609	1628	1633	1646	1611	1624	1649	1649
SS-1	1424	1444	1463	1477	1476	1498	1514	1527
SS-2	1571	1593	1598	1618	1576	1600	1612	1622
SS-3	1437	1454	1469	1504	1458	1519	1539	1551
SS-4	1401	1461	1477	1498	1462	1487	1516	1526
SS-5	1368	1392	1402	1437	1441	1465	1492	1501
SS-6	1649	1649	1649	1649	1649	1649	1649	1649
SS-7	1220	1248	1277	1354	1345	1383	1405	1421
SS-8	1361	1396	1416	1429	1418	1456	1477	1492
SS-9	1420	1465	1488	1524	1482	1509	1534	1581
SS-10	1419	1454	1477	1511	1463	1497	1516	1533
SS-11	1138	1158	1166	1190	1177	1196	1211	1244
SS-12	1174	1191	1212	1239	1199	1221	1254	1276
SS-13	1208	1221	1227	1241	1227	1217	1338	1242
SS-14	1156	1173	1178	1202	1157	1180	1193	1216
SS-15	1140	1151	1163	1192	1182	1202	1218	1242
SS-16	1343	1427	1459	1499	1467	1497	1516	1531
SS-17	1306	1345	1358	1405	1376	1403	1435	1454
SS-18	1358	1417	1443	1474	1420	1470	1488	1513
SS-19	1337	1423	1405	1484	1400	1464	1489	1518

ToF-SIMS spectra, and especially ToF-SIMS spectra from complicated materials, often contain hundreds or even thousands of peaks. For example, in just one region (between 0 and 100 amu) of a representative ToF-SIMS spectrum of a coal sample analyzed in this work (one of the SS-1 spectra – see Table 5.1), there are at least 244 distinct peaks. This wealth of information may create a problem for the analyst, especially when a series of complicated spectra from different materials must be compared. In the last few years, chemometrics methods,[6-8] which are advanced statistical tools, have been increasingly applied to ToF-SIMS data sets to better extract and identify the chemical information they contain.[9-13] Three of the best known chemometrics methods are principal components analysis (PCA), cluster analysis, and partial least squares (PLS). There are a number of good references for these methods.[6, 14-20]

Here, I report a ToF-SIMS study of 34 different coal samples. In many cases, the inorganic ions dominate the spectra, eclipsing the organic peaks. A score plot of PC1 vs. PC2 effectively separates the coal spectra into a triangular pattern, where the different vertices of this pattern come from different types of coal samples. Loadings plots of PC1 and PC2 confirm these observations. Cluster analysis reveals a dendrogram that correlates extremely well with the clustering of the data points found in the plot of PC1 vs. PC2. The separation of the spectra in the cluster analysis and the PC1 vs. PC2 score plots appear to be related to some of the other measured properties of the coal samples. PLS confirms this relationship for a number of these properties. Thus, ToF-SIMS appears to be a promising technique for coal analysis.

To the best of my knowledge, this paper is the first ToF-SIMS study of multiple, different coal samples that shows the effectiveness of chemometrics methods for both categorization of the spectra and regression. However, SIMS has also been effectively used to study coal samples

in the past. For example, Sakamoto and coworkers used ToF-SIMS with focused-ion-beam cross sectioning to analyze coal fly ash particles, which were shown to contain Al and Si as major constituents and Na, Mg, K, Ti and Fe as minor constituents.[21] Pigram and coworkers used ToF-SIMS to analyze silica particles in a bituminous coal sample, and also showed ion imaging of coal cross sections.[22] Domazetis and coworkers studied "mono- and polynuclear iron hydroxy complexes in brown coal,"[23] a lower rank coal, and they have also published a scanning electron microscopy (SEM), X-ray photoelectron spectroscopy (XPS), and ToF-SIMS study of a series of brown coals that included traditional characterization of the samples.[24]

Electrospray ionization mass spectrometry (ESI-MS) has also been used on coal and crude oil samples. For example, Fenn and coworkers carried out exploratory experiments on crude oil, jet fuel, gasoline, and coal samples.[25] Marshall and coworkers first used electrospray ionization Fourier transform ion cyclotron resonance mass spectrometry (ESI-FTICR-MS) to analyze coal extract samples.[26-27] They also applied ESI-FTICR-MS with ultrahigh resolution to crude oil.[28] Roussis and coworkers quantitatively analyzed polar and ionic compounds in petroleum fractions by ESI-MS and atmospheric pressure chemical ionization (APCI) mass spectrometry.[29] Mayer and coworkers analyzed polar resin fractions of crude oil, fuel oil, and diesel by ESI-MS.[30] Eide and coworkers used ESI-MS on oil and petroleum products and they also applied chemometrics methods to the spectra of the oil samples.[31]

5.3 Experimental

5.3.1 Materials

Commercially significant coal samples obtained from coal mining and power plant companies form the basis of this analysis. These samples include all commercially significant coal ranks for power generation (bituminous and subbituminous coals and lignites), although the low-rank samples (lignites and subbituminous coals) comprise a small fraction of the database.

5.3.2 ToF-SIMS

ToF-SIMS was performed with monoisotopic $^{69}Ga^{+}$ from an ION-TOF (Münster, Germany) TOF-SIMS IV instrument. The primary ion (target) current was typically 3 pA, with a pulse width of 20 ns before bunching.

5.3.3 Sample Preparation

Coal samples were ground with a mortar and pestle and immediately mounted on double sticky tape. Regions of 500 μm x 500 μm were then analyzed by ToF-SIMS, where 106 positive ion spectra were taken of 36 different coal samples. In general, three spectra were taken of each coal sample. After an initial PCA analysis, three of the spectra, which come from JIG014, RLL012 and PCT012 in Table 5.3, were found to be significant outliers and were removed for the PCA analysis shown herein. For the PLS analysis, only 99 of the spectra were considered because properties were not available for two of the coal samples (ILL#6 and Blackthunder samples, each of which has only two spectra), which could, therefore, not be considered in PLS.

5.3.4 Chemometrics

PCA, cluster analysis, PLS (using PLS1), interval PLS (iPLS), and a genetic algorithm were performed using the PLS_Toolbox 4.0 from Eigenvector Research (Wenatchee, WA). The

PLS_Toolbox is a MATLAB toolbox that was run under MATLAB 7.2. The spectra which range from 0 to 350 amu were binned to half unit mass resolution, e.g., from 1.5 – 2.0 amu, from 2.0 – 2.5 amu, from 2.5 – 3.0 amu, etc., using the ToF-SIMS instrument software. These binned spectra were then exported to Microsoft Excel where they were normalized using the "1-Norm", which is the division of each spectral region by the sum of the areas in that spectrum. The data were then mean centered for PCA and cluster analysis. The data matrices used for chemometrics contained one spectrum per row and one variable per column, for a total of 700 variables (columns). Two preprocessing methods used for the PLS analysis were considered. In the first, the ToF-SIMS data were normalized and square root transformed, where it has been shown that square root scaling is often advantageous for (ToF-SIMS) data that is Poisson distributed.[32] Both the spectra and the properties data were then mean centered. The second method employs the same preprocessing for the spectral data, but the log 10 of the properties data was taken before it was mean centered. Taking the log of data may linearize it, which is advantageous for PLS because it is a linear technique.

Because this work was an exploratory study, I opted to analyze my data in the most simple and straightforward manner possible: I first binned, and then mean centered the data. Mean centering is the most common preprocessing method for scaling mass spectrometric data,[31] and it has been shown to be more effective than other preprocessing methods in handling ToF-SIMS data that have been binned.[10] That is, if autoscaling, i.e., scaling to unit variance, had been applied to the binned data, the results would have been, at best, questionable because a large number of regions that contain mostly noise would have been put on par with those that contain signal. Indeed, I did perform PCA on the autoscaled data, and the loadings plots show a significant number of large, high mass peaks that are meaningless (it can be shown that they are

only due to noise in the original spectra). Of course, prior to autoscaling, I could have applied a threshold to the data below, which no peaks would be accepted. However, there is always some subjectivity in such choices, and this approach would make the analysis more complex. Again, I wanted to focus on the most direct method possible for data analysis.

The coal data set for PLS analysis was organized so that all of the replicates from a given sample were generally left out in any iteration of the cross validation analysis when that sample's properties were being predicted.[33] Using the contiguous block method for cross validation, the data set was divided into 9 equal size segments. A model was built on all but one of the segments. The model was then used to predict the properties of samples in the omitted segment.[34-35] The minimum value in the RMSECV (root mean square error cross validation) plot from this cross validation analysis was used to determine the number of latent variables to keep. While in a few cases, this method suggests a rather large number of latent variables, it has the advantage of eliminating user bias in variable selection and is, therefore, suitable for this initial study. The genetic algorithm used PLS as the regression choice in the software and also used the same conditions for preprocessing and cross validation that were employed in other analyses performed herein. For the GA analysis, a random subset of variables was first selected, where each set of variables was considered to be an "individual." PLS and cross validation were then performed on the subset of variables that represent each of these individuals. The worst half of the individuals, which have higher RMSECV values than the median value, were discarded. The remaining individuals (variable sets) were used for breeding the next generation with double cross-over and mutation methods. Using this approach iteratively, the individual that gives the lowest RMSECV value, can be found.

The K-means clustering method,[6, 14, 17] a type of hierarchical clustering analysis, is conceptually based on the Euclidean distances between all data points. In principle, the two closest points are clustered and replaced by the mean of these two points. Through this approach, all the data points can be clustered into a dendrogram.

5.4 Results and Discussion

Time-of-flight secondary ion mass spectrometry (ToF-SIMS) was performed on a series of coal samples with different ranks and origins. As expected, the spectra are generally quite complicated and contain significant organic and inorganic character. Figure 5.1a shows the average of all of the spectra that were taken, and Figure 5.1b shows a superposition of all of the spectra together. It is clear that the inorganic ions from these samples, e.g., Na^+, Al^+, and K^+, often dominate the coal spectra, and that the majority of the signal occurs below 100 amu. In contrast to ESI-MS that usually produces high molecular mass ions from analytes,[25-31] the SIMS process usually results in significant fragmentation of analytes, which leads to a large number of low mass peaks.

Because of the complexity of many SIMS spectra, principal components analysis (PCA) and other chemometrics methods such as cluster analysis are increasingly employed to analyze ToF-SIMS data. A number of recent references describe and/or explain the chemometrics methods that will be used herein.[6, 9-11, 36-38] Accordingly, the data shown in Figure 5.1b were analyzed by PCA. Cross validation and plot of variance captured vs. principal component number in the PCA analysis suggest that this complicated data set of 106 spectra is well described by just two principal components, which together account for more than 90% of the total variance in the data.

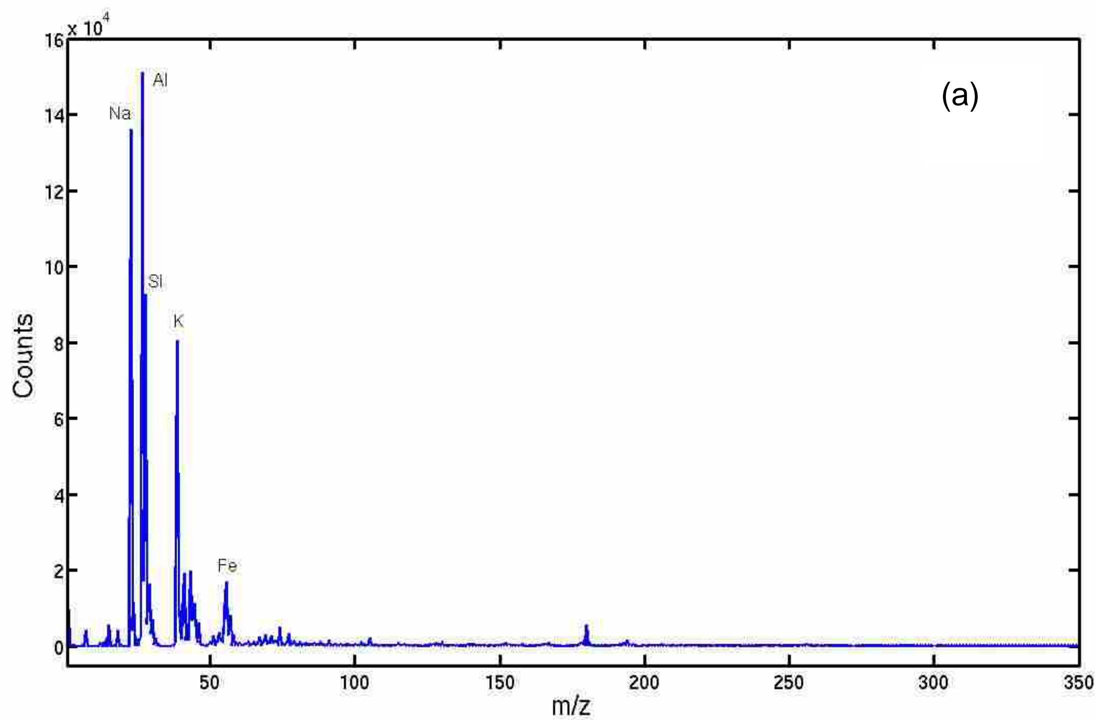

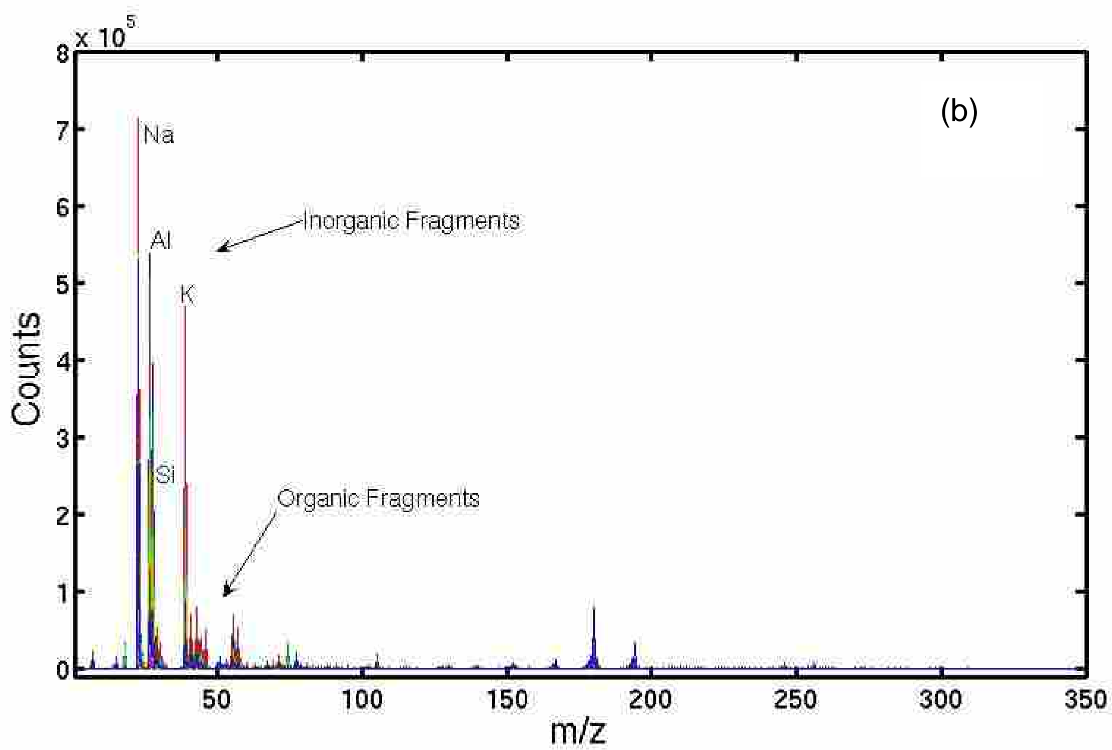

Figure 5.1. (a) Average of all of the ToF-SIMS spectra of the coal samples, and (b) superimposition of all of the ToF-SIMS spectra of the coal samples.

Scores plots, which are a graphical representation of PCA results, are often effective in revealing relationships between spectra. Figure 5.2 shows a plot of the scores on PC1 vs. PC2 for the ToF-SIMS coal data. The data fall into a triangular pattern. It was of interest to understand which chemical features in the ToF-SIMS spectra are responsible for the separation between the spectra found in Figure 5.2. The spectra corresponding to the five points that are nearest each vertex of the triangle in Figure 5.2 were averaged. It is clear from these spectra (see Figure 5.3) that the points in the upper left vertex contain a strong inorganic signature of Al^+, Si^+, K^+, and Fe^+. Those points in the vertex at the far right are dominated by Na^+, with smaller Al^+ and K^+ signals. The spectra in the lower left vertex are organic, that is, they are dominated by organic, not inorganic ions. These results are consistent with the ash content of these samples that was determined by traditional laboratory means. The average ash content of the samples with the inorganic signatures are 12.6% (upper left vertex) and 11.1% (far right vertex), while the ash content is much lower for the samples in the lower left vertex (6.1%).

Although no traditional analysis data contribute to this separation, the results correspond to a very high degree to fuel classifications by type. Specifically, the fuels at the lower-left vertex are low-rank fuels: subbituminous coals and lignites. They have relatively high moisture, high oxygen contents, low heating values, low overall inorganic fractions with high fractions of calcium in the inorganic fraction, and low sulfur contents. They are located principally in the western US and are relatively young (30 million years old). They are generally surface (open-pit) as opposed to deep-mined. These fuels have, in the last 20 years, become a primary contributor to emissions compliance from power plants. These fuels have highly characteristic combustion behaviors, commonly exhibiting much lower strength during pulverization, and significantly

higher oxidation rates. They form highly reflective (of thermal radiation), calcium-rich fouling deposits from their inorganic residues.

The other two vertices correspond to finer gradations among bituminous coals. The highest rank coals correspond to the far right vertex and characteristically have high heating values, low volatile yields, and low H:C and O:C ratios. These are among the oldest and most mature coals (40-60 million years). They find commercial application in both power generation and as coking fuels. They commonly come from the Appalachian region of the United States. Upon combustion, these fuels are characteristically less reactive and less porous. The inorganic residue has far more slagging and far less fouling character compared to the previous fuels, although they are reasonably similar to the next group in this regard. These fuels have very little volatile inorganic material but high illite (potassium aluminosilicate material characteristic of many soils) content.

The fuels in the upper vertex are high-volatile, high-rank fuels that, until the last 20 years, dominated the power generation industry and still find substantial, although not dominant, use in these markets. These fuels have reasonably high heating values and volatile contents, making them ideal for power generation. They are intermediate in age compared to the subbituminous and low-volatile bituminous fuels. They have high H:C ratios compared to the highest rank fuels (but low or comparable values compared to subbituminous fuels). They are generally deep mined and commonly come from the Midwest (Illinois, Ohio, etc.). Upon combustion, they produce chars of intermediate reactivity compared to the previous two fuels and with inorganic residue similar in many ways to the low-volatile bituminous group.

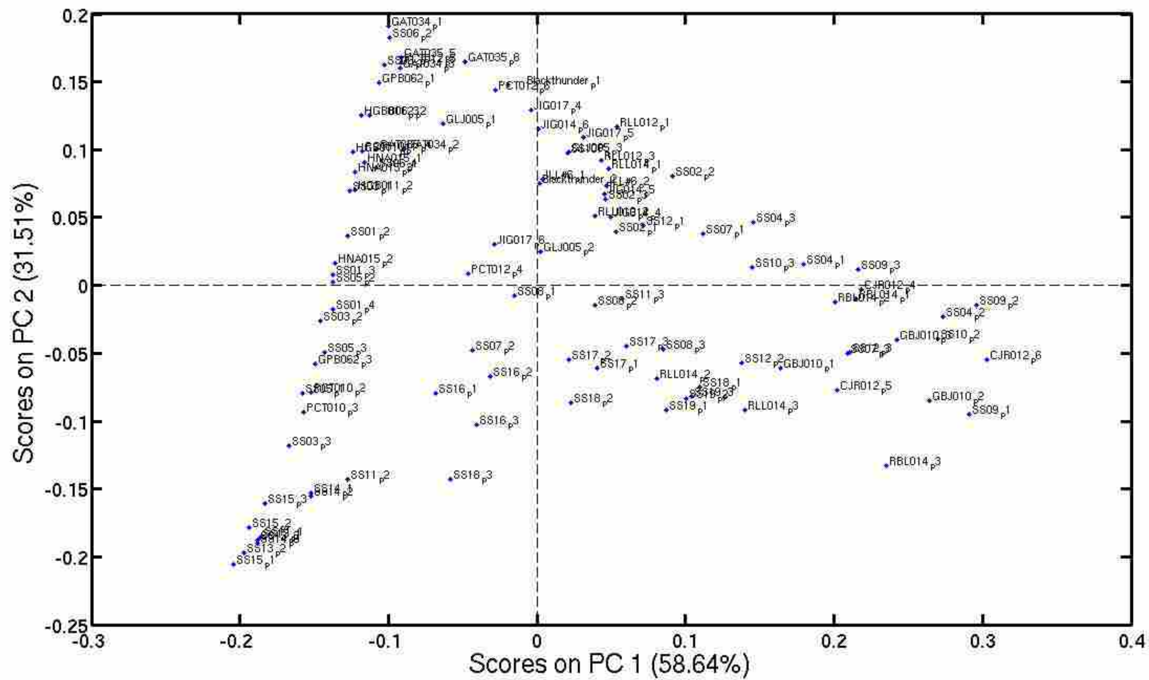

Figure 5.2. Plot of the scores of the coal spectra on the first and second principal components from a principal components analysis (PCA).

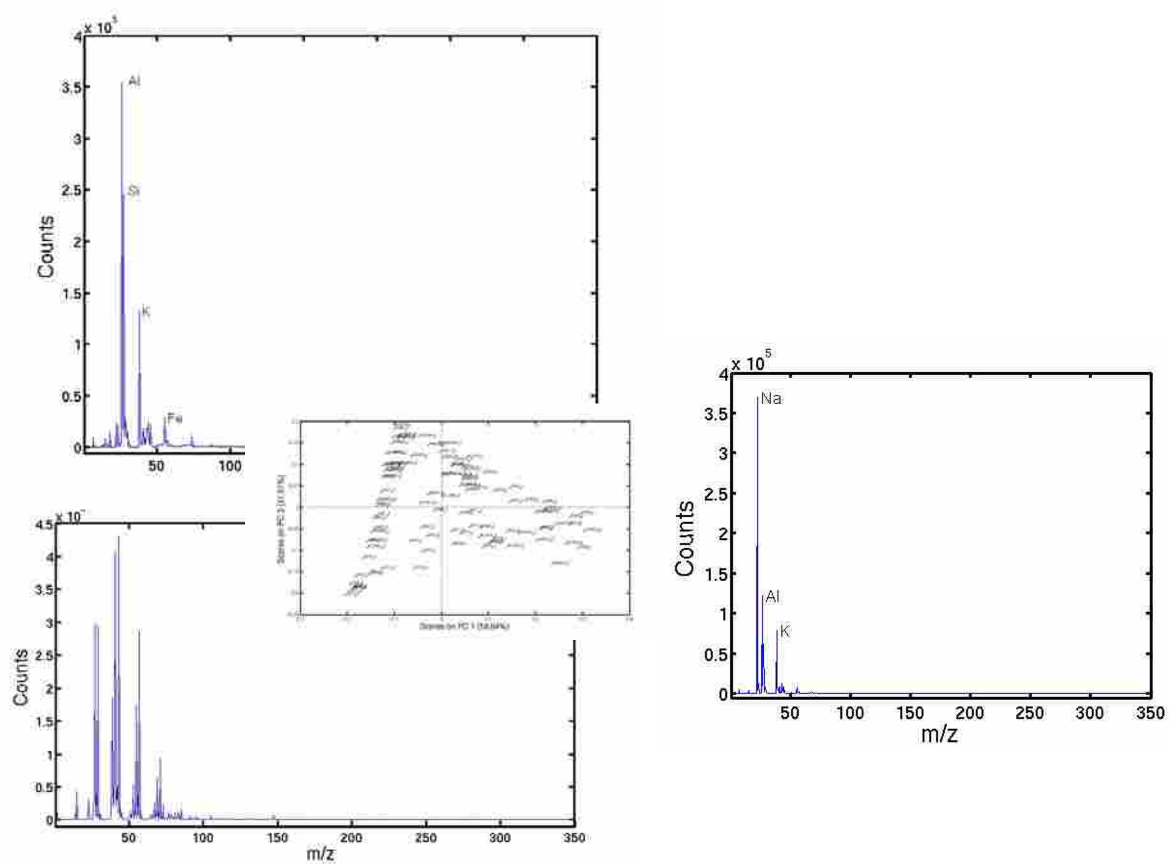

Figure 5.3. Average spectra of the spectra represented by the five points at the three vertices of the PC1 vs. PC2 plot.

The fact that the PCA is able to separate these coals into these classical categories with no reliance on traditional analyses indicates that the ToF-SIMS data and PCA may provide meaningful and technically useful insight into their structures and properties. Coals, of course, span a wide range of properties with the descriptions above representing characteristics of the three extremes.

The chemical differences between spectra suggested in Figure 5.3 are confirmed by the loadings on PC1 and PC2. The dominant feature in the loadings plot for PC1 (Figure 5.4) is a strong positive signal that corresponds to Na^+. This is consistent with the fact that the spectra at the far right (the positive side) of the scores plot (Figure 5.2) have strong Na^+ signals. The negative peaks in the loadings plot for PC1 appear to be mostly organic. The loadings on PC2 show a similar trend (see Figure 5.5). The large positive peaks are inorganic (Al^+, Si^+, and K^+), while the negative peaks are organic. These results are again consistent with the scores plot in Figure 5.2, where the points (spectra) with positive scores on PC2 are dominated by Al^+, Si^+, and K^+, while those with negative scores on PC2, especially those around the lower left vertex of the points, contain a strong organic signature.

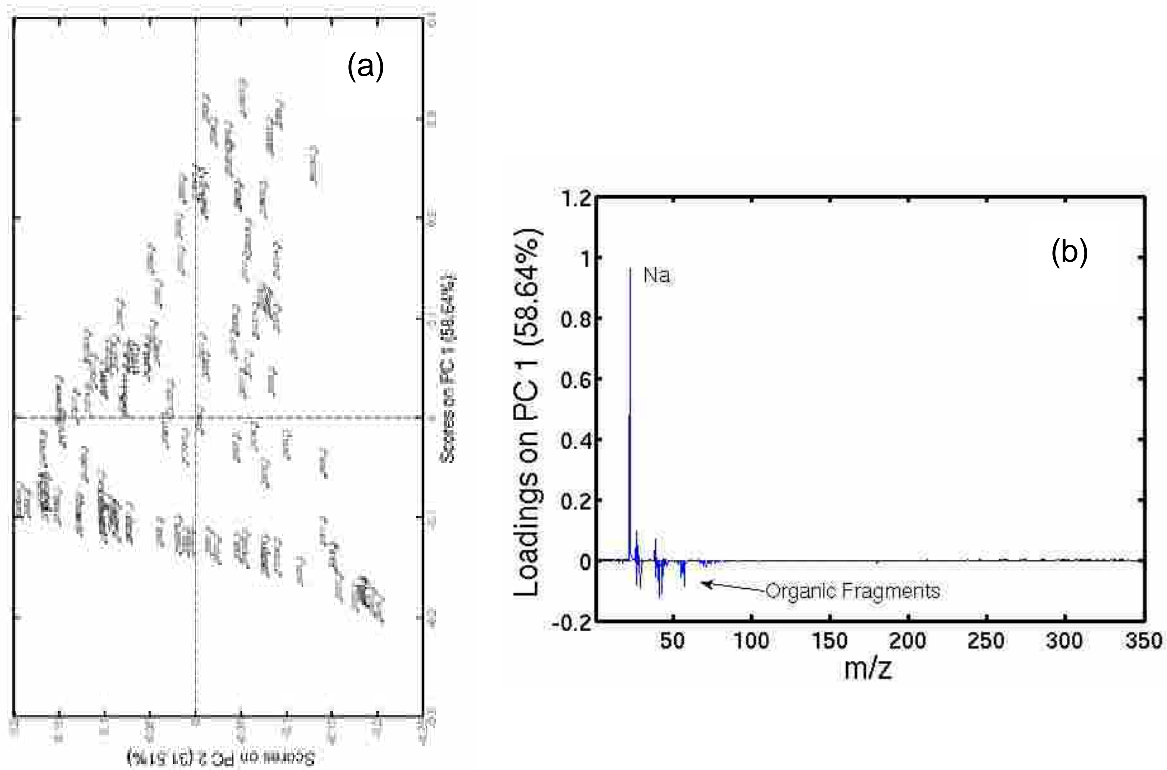

Figure 5.4. (a) Rotated plot of PC1 vs. PC2 that shows the variation in PC1 along the vertical direction that corresponds to the variation in the loadings plot shown in (b).

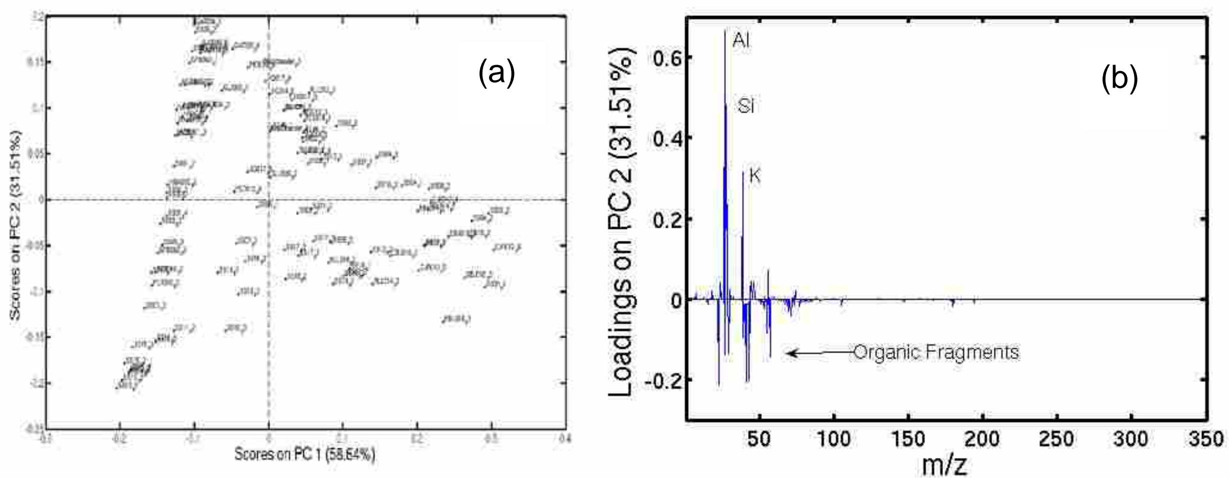

Figure 5.5. (a) Plot of PC1 vs. PC2 that shows the variation in PC2 along the vertical direction that corresponds to the variation in the loadings plot shown in (b).

A disadvantage of PCA and some other chemometrics methods is that they introduce some degree of abstraction into data analysis, which may be particularly troublesome for those who are inexperienced with these methods. This abstraction may also make it difficult to have full confidence in the validity of a PCA analysis. To increase one's certainty that an analysis has been performed properly, a second categorization method, such as cluster analysis, may be applied to the data. Cluster analysis has the advantage that its output, a dendrogram, is based on all of the variance in the data, while most scores plots from PCA are only based on a fraction of the variance in the data. Figure 5.6 shows a dendrogram from a K-means cluster analysis that groups the spectra into different clusters. To demonstrate the consistency of the PCA and cluster analyses, Figure 5.6a shows the results from the cluster analysis for one cluster plotted on the PCA scores plot (this first part of the plot is a trivial result). Figure 5.6b then shows the division of the data into two clusters in the dendrogram, one of which is at the right vertex of the PC1 vs. PC2 plot. Continuing, Figure 5.6c shows the division of the data into three clusters in the dendrogram, again showing the positions of these clustered spectra on the PC1 vs. PC2 plot. It is gratifying to see clustering around the vertices (extrema) of the PC1 vs. PC2 plot. These trends continue in Figures 5.6d – g. It is of great significance that spectra in clusters in the cluster analysis are adjacent to each other in the PC1 vs. PC2 plot. It is also significant that replica spectra from a given coal sample generally appear in the same cluster or in adjacent clusters (see Table 5.1). The fact that the clustering is not tighter for the replicates is attributable to coal's heterogeneous nature.

(a)

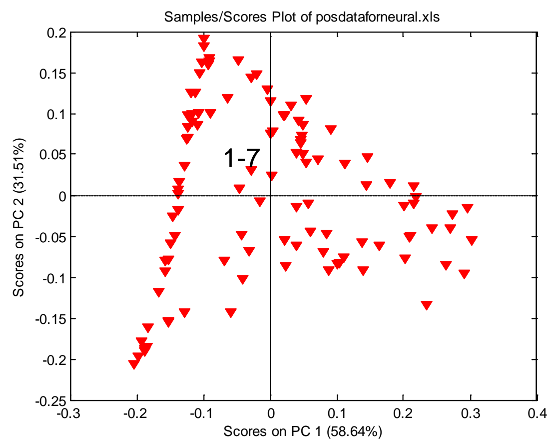

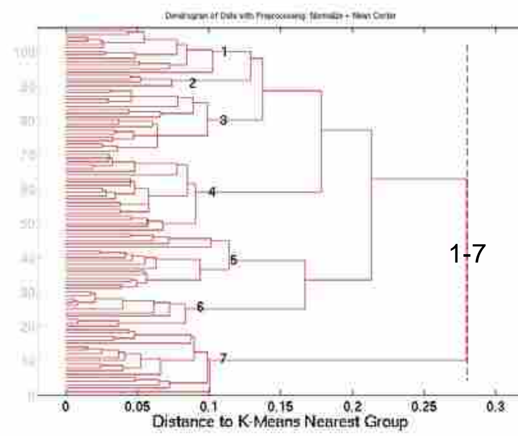

(b)

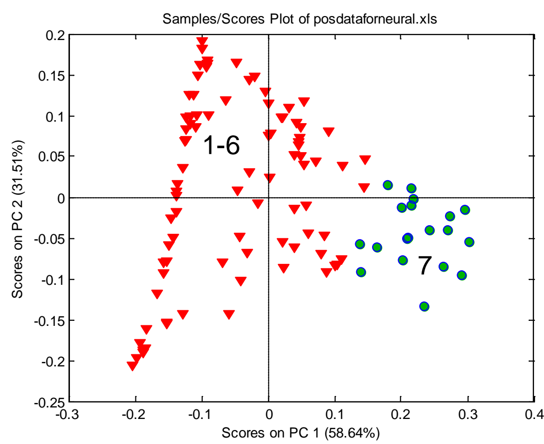

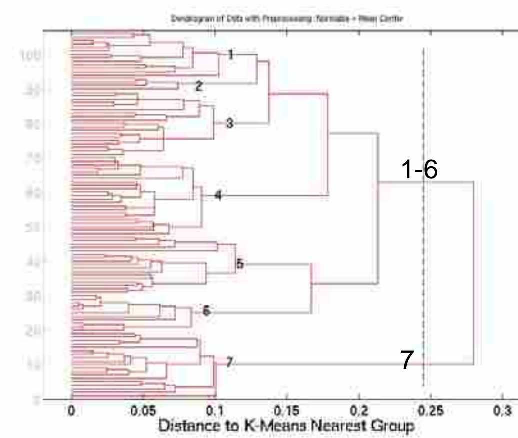

Figure 5.6. a-b.

(c)

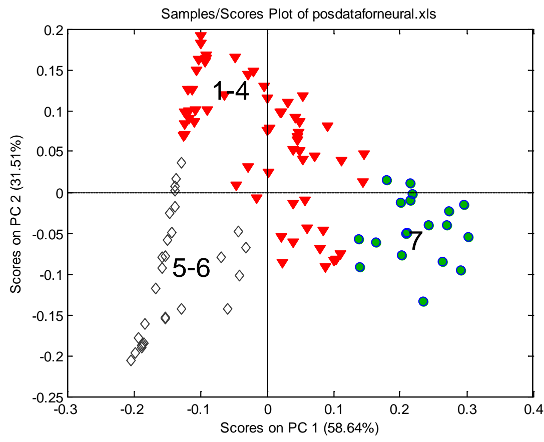

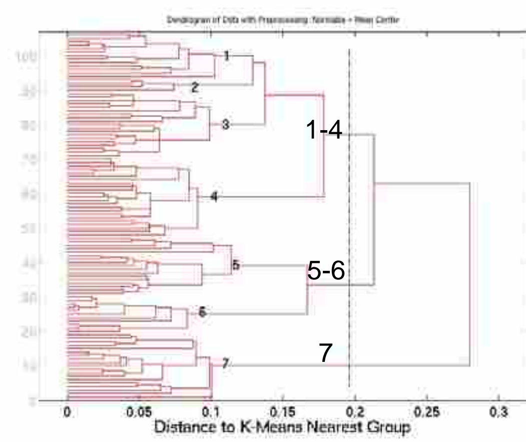

(d)

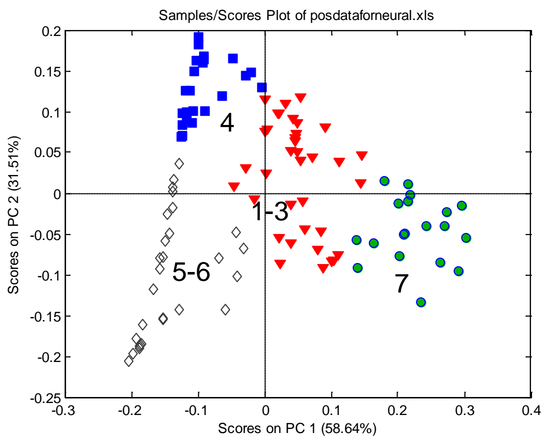

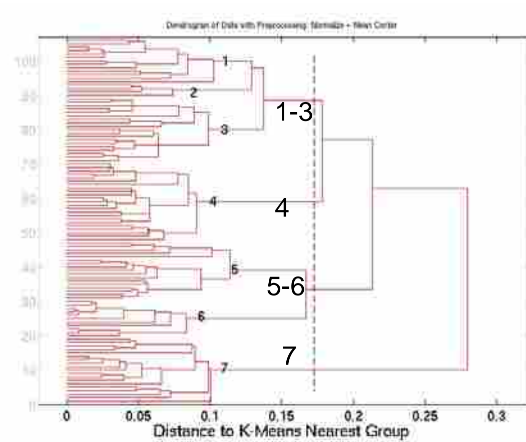

(e)

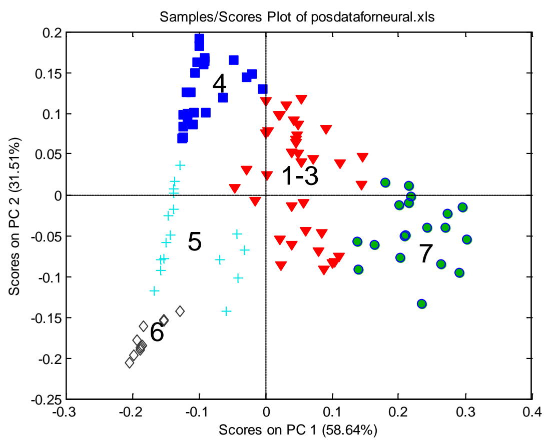

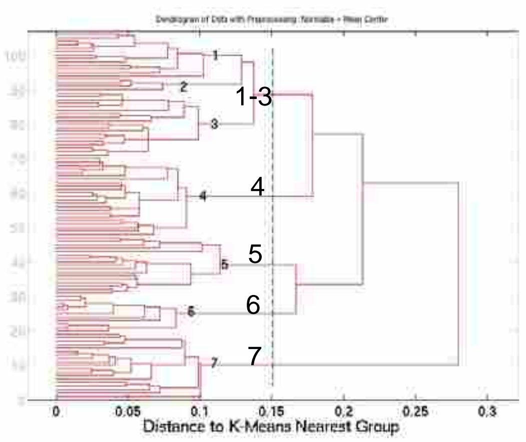

Figure 5.6. c-e.

(f)

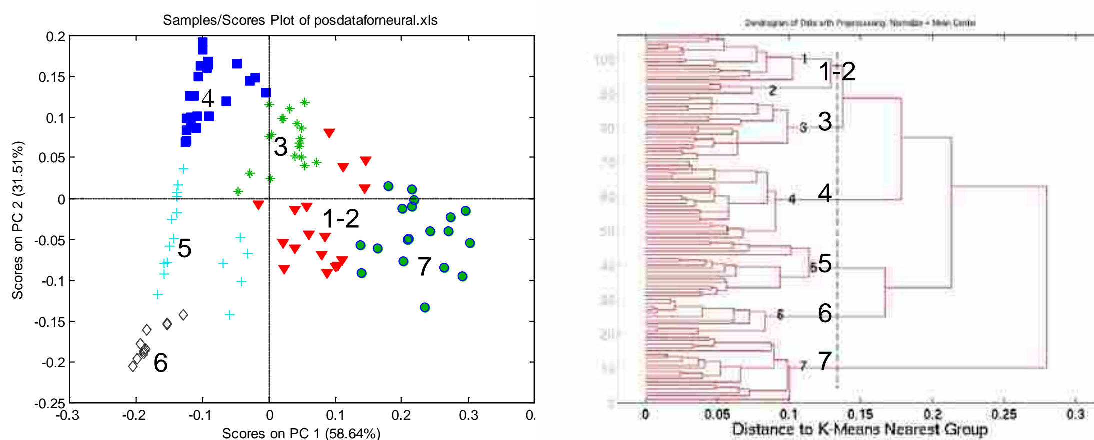

(g)

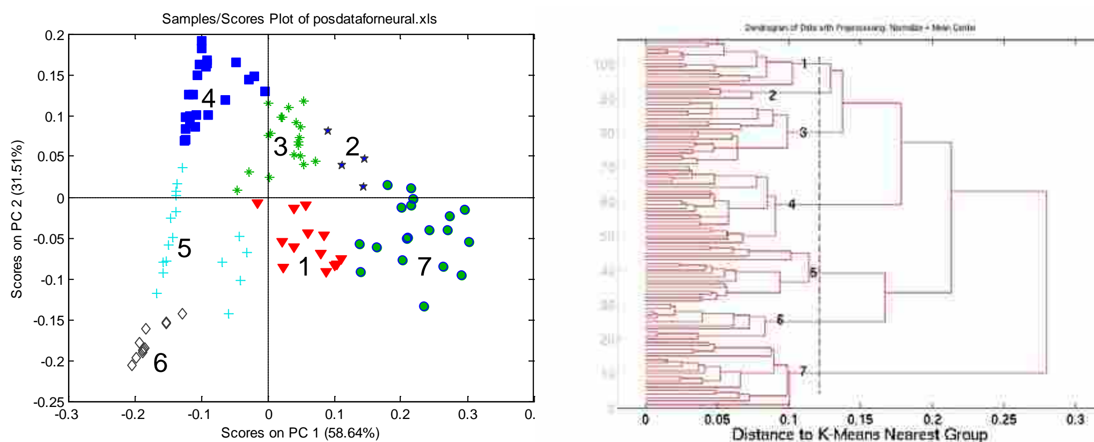

Figure 5.6. PC1 vs. PC2 score plots (left) that show the locations (numbering based on the vertical dashed line) on this PCA plot of the spectra in the seven clusters of the dendrogram from the cluster analysis (right).

While it is important that the two different chemometrics methods (PCA and cluster analysis) separate and group the spectra in a similar fashion, an important issue has not yet been addressed, which is the relationship between the ToF-SIMS spectra and the other properties of the coal samples measured by more traditional methods. Table 5.4 shows the average value for each measured property from a traditional fuel analysis in each of the seven clusters in the cluster analysis. The correspondence between the qualitative descriptions of the three vertices provided earlier and the quantitative averages of the clusters at these vertices is clear. For example, cluster 6 has the highest moisture content and the lowest heating value of all the fuels, which is consistent with its designation as the low-rank vertex. Clusters 7 and the neighboring Cluster 2 have the lowest H:C ratio, the lowest volatile yield, and the highest heating values and carbon contents of all clusters, consistent with its designation as the high-rank vertex. The high-volatile and high-rank fuels are consistent with the properties of Cluster 4. However, Cluster 4 also has a low iron, calcium, and sodium content with a high silica content. These properties do not generally correlate with rank among high-rank coals but do lead to a very important commercial property of high ash fusion temperature. As is seen, Cluster 4 and its neighbor, Cluster 3, generally have the highest fusion temperatures among all clusters. This shows that this advanced analysis has promise of providing correlations to physical behavior that are difficult to derive from rank or similar traditional analyses.

Cluster	Moisture	Volatile Matter	Ash	Carbon	Hydrogen
1	4.6±5.0	35.5±6.7	9.7±2.6	74.7±2.3	4.79±0.32
2	0.91±0.49	24.6±6.9	12.3±2.2	77.1±3.7	4.30±0.37
3	3.7±5.1	33.3±6.8	10.3±2.3	75.6±3.8	4.53±0.25
4	3.2±1.4	34.3±1.4	12.1±2.3	73.2±3.0	4.59±0.19
5	2.8±1.5	34.1±4.2	12.1±4.3	72.7±2.5	4.62±0.31
6	20.49±0.34	47.18±0.87	6.49±0.99	69.3±1.1	4.47±0.20
7	3.4±5.7	31.9±7.7	10.7±2.2	75.6±2.5	4.46±0.31

Cluster	Nitrogen	Sulfur	Heating Value	Chlorine	Oxygen
1	1.58±0.20	0.81±0.27	$1.32 \pm 0.04 \times 10^4$	0.13±0.20	8.2±3.3
2	1.63±0.08	0.90±0.57	$1.35 \pm 0.05 \times 10^4$	0.02±0.01	3.8±1.4
3	1.62±0.21	0.82±0.27	$1.33 \pm 0.07 \times 10^4$	0.07±0.07	7.1±3.7
4	1.54±0.11	1.05±0.25	$1.29 \pm 0.05 \times 10^4$	0.07±0.04	7.4±1.2
5	1.52±0.10	1.23±0.42	$1.28 \pm 0.05 \times 10^4$	0.03±0.03	7.9±2.5
6	0.87±0.05	0.45±0.33	$1.17 \pm 0.07 \times 10^4$	0.00±0.00	18.4±1.3
7	1.53±0.22	0.94±0.33	$1.33 \pm 0.05 \times 10^4$	0.07±0.08	6.7±4.2

Cluster	H:C	O:C	SiO_2	Al_2O_3	TiO_2
1	0.08±0.04	0.76±0.06	51.8±8.1	25.2±3.3	1.12±0.19
2	0.04±0.02	0.67±0.08	48.3±3.8	29.2±3.1	1.37±0.16
3	0.07±0.04	0.72±0.06	52.0±5.3	28.0±4.4	1.31±0.20
4	0.08±0.01	0.75±0.02	55.1±4.2	28.5±2.1	1.43±0.15
5	0.08±0.02	0.76±0.03	51.9±4.8	26.3±1.4	1.18±0.17
6	0.20±0.02	0.77±0.04	31.3±4.3	15.03±0.87	1.17±0.18
7	0.07±0.05	0.70±0.06	50.1±5.1	27.0±3.9	1.33±0.16

Cluster	Fe_2O_3	CaO	MgO	Na_2O	K_2O
1	8.2±2.4	4.3±4.7	1.44±0.60	1.24±0.52	1.98±0.85
2	8.4±4.0	4.06±0.62	1.31±0.22	0.67±0.24	2.29±0.25
3	7.9±2.3	3.3±4.7	1.4±1.1	0.47±0.23	2.60±0.83
4	7.6±4.4	1.21±0.38	0.91±0.15	0.26±0.06	2.39±0.19
5	10.5±3.5	2.2±1.1	1.12±0.15	0.49±0.27	2.31±0.53
6	6.2±1.1	23.3±2.8	5.0±1.1	1.67±0.45	0.35±0.11
7	8.6±2.0	4.0±5.0	1.5±1.2	0.64±0.26	2.14±0.57

Cluster	P_2O_5	SO_3	Reducing Initial	Reducing H=W	Reducing H=1/2W
1	0.65±0.17	3.5±5.6	$2.45\pm0.18\times10^3$	$2.54\pm0.18\times10^3$	$2.55\pm0.18\times10^3$
2	0.90±0.19	2.64±0.72	$2.56\pm0.26\times10^3$	$2.62\pm0.26\times10^3$	$2.66\pm0.24\times10^3$
3	0.85±0.61	2.3±2.3	$2.73\pm0.21\times10^3$	$2.77\pm0.21\times10^3$	$2.79\pm0.20\times10^3$
4	0.54±0.31	1.29±0.42	$2.64\pm0.22\times10^3$	$2.70\pm0.18\times10^3$	$2.74\pm0.15\times10^3$
5	0.54±0.25	2.39±0.88	$2.54\pm0.12\times10^3$	$2.61\pm0.11\times10^3$	$2.65\pm0.11\times10^3$
6	1.08±0.24	13.9±4.1	$2.12\pm0.05\times10^3$	$2.15\pm0.05\times10^3$	$2.16\pm0.05\times10^3$
7	0.62±0.54	2.7±2.5	$2.59\pm0.21\times10^3$	$2.65\pm0.21\times10^3$	$2.69\pm0.21\times10^3$

Cluster	Reducing Fluid	Oxidizing Initial	Oxidizing H=W	Oxidizing H=1/2W	Oxidizing Fluid
1	$2.63\pm0.18\times10^3$	$2.55\pm0.16\times10^3$	$2.63\pm0.16\times10^3$	$2.67\pm0.16\times10^3$	$2.71\pm0.16\times10^3$
2	$2.72\pm0.19\times10^3$	$2.66\pm0.17\times10^3$	$2.72\pm0.16\times10^3$	$2.75\pm0.15\times10^3$	$2.78\pm0.15\times10^3$
3	$2.83\pm0.19\times10^3$	$2.78\pm0.19\times10^3$	$2.82\pm0.19\times10^3$	$2.84\pm0.18\times10^3$	$2.86\pm0.18\times10^3$
4	$2.79\pm0.14\times10^3$	$2.78\pm0.13\times10^3$	$2.82\pm0.11\times10^3$	$2.84\pm0.10\times10^3$	$2.86\pm0.09\times10^3$
5	$2.71\pm0.09\times10^3$	$2.68\pm0.10\times10^3$	$2.73\pm0.09\times10^3$	$2.77\pm0.08\times10^3$	$2.79\pm0.08\times10^3$
6	$2.21\pm0.04\times10^3$	$2.17\pm0.05\times10^3$	$2.19\pm0.03\times10^3$	$2.27\pm0.11\times10^3$	$2.26\pm0.02\times10^3$
7	$2.74\pm0.20\times10^3$	$2.69\pm0.20\times10^3$	$2.73\pm0.20\times10^3$	$2.78\pm0.19\times10^3$	$2.80\pm0.19\times10^3$

Cluster	Difference Initial	Difference H=W	Difference H=1/2W	Difference Fluid	Iron Content
1	$1.02\pm0.33\times10^2$	$0.85\pm0.31\times10^2$	$1.13\pm0.38\times10^2$	$0.79\pm0.30\times10^2$	8.2±2.4
2	$1.06\pm0.90\times10^2$	$1.0\pm1.0\times10^2$	$0.99\pm0.91\times10^2$	$0.54\pm0.47\times10^2$	8.4±4.0
3	$0.49\pm0.56\times10^2$	$0.51\pm0.46\times10^2$	$0.55\pm0.36\times10^2$	$0.34\pm0.33\times10^2$	7.9±2.3
4	$1.3\pm1.0\times10^2$	$1.18\pm0.72\times10^2$	$0.98\pm0.57\times10^2$	$0.75\pm0.49\times10^2$	7.6±4.4
5	$1.36\pm0.59\times10^2$	$1.27\pm0.32\times10^2$	$1.18\pm0.41\times10^2$	$0.87\pm0.22\times10^2$	10.5±3.5
6	$0.43\pm0.31\times10^2$	$0.39\pm0.43\times10^2$	$1.04\pm0.68\times10^2$	$0.49\pm0.43\times10^2$	6.2±1.1
7	$1.00\pm0.45\times10^2$	$0.85\pm0.47\times10^2$	$0.87\pm0.39\times10^2$	$0.63\pm0.31\times10^2$	8.6±2.0

Table 5.4. Average properties of the coal samples, as measured by conventional means, for the spectra in each of the seven clusters in the dendrogram. The errors in this table (and in Figure 5.8) are standard deviations.

In addition to the chemometrics analysis of the ToF-SIMS spectra, a multivariate analysis can be performed for each coal sample using the properties that were measured for it. Unlike the ToF-SIMS spectra, which were mean centered prior to analysis, the measured properties for each sample, many of which had different units, were autoscaled prior to the chemometrics, where autoscaling is an appropriate approach for this type of data. Figure 5.7 shows some of the results from the cluster and PCA analyses of this data set. The cluster analysis in Figure 5.7a clearly shows a cluster at the bottom of the dendrogram from coal samples that are distinct from the others. These are the coal samples in Cluster 6 of the PC1 vs. PC2 plot of the ToF-SIMS data in Figure 5.6. Similarly, the PCA analysis of the measured properties in Figure 5.7b shows that a subset of the samples are distinct from the others on PC1, which PC accounts for more than 50% of the variance in the data. This subset of coal samples again corresponds to those in Cluster 6 of the PC1 vs. PC2 plot of the ToF-SIMS data.

To illustrate the correlations previously discussed between the ToF-SIMS spectra and the measured properties of the samples, Figures 5.8a and 5.8b show the PC1 vs. PC2 plot of the ToF-SIMS spectra with two of the measured properties from Table 5.4 written on the clusters. It is clear from Figure 5.8a that the heating value of the samples increases from a minimum at Cluster 6, which is in the lower left corner, and increases as one moves up and to the right in this plot. Similarly, Figure 5.8b shows that upon moving from Cluster 6 to Cluster 7, and upon moving from Cluster 6 to Cluster 4, the Al_2O_3 content of the samples increases.

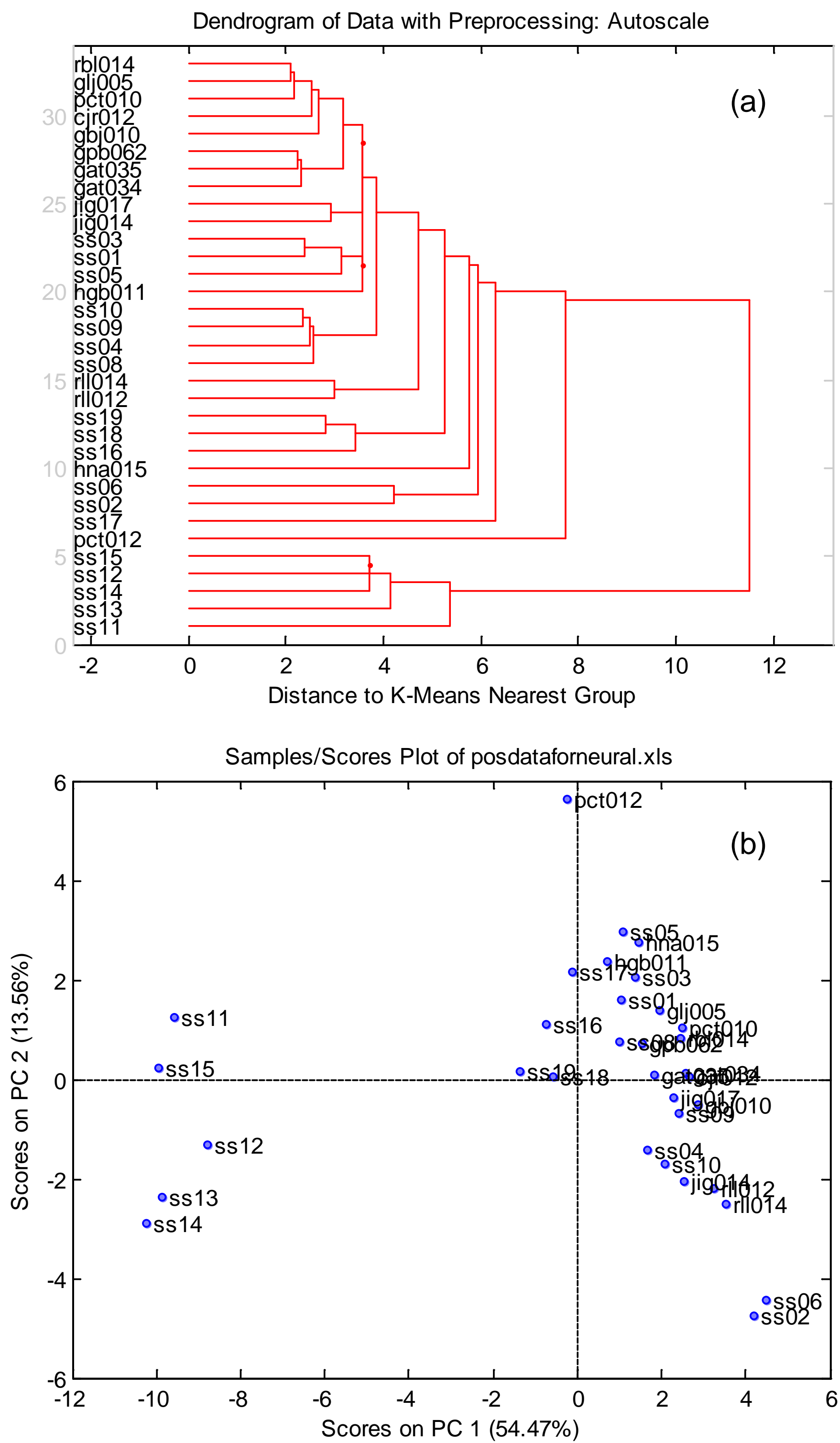

Figure 5.7. (a) Cluster analysis and (b) PCA of the properties of the coal samples, as measured by conventional methods.

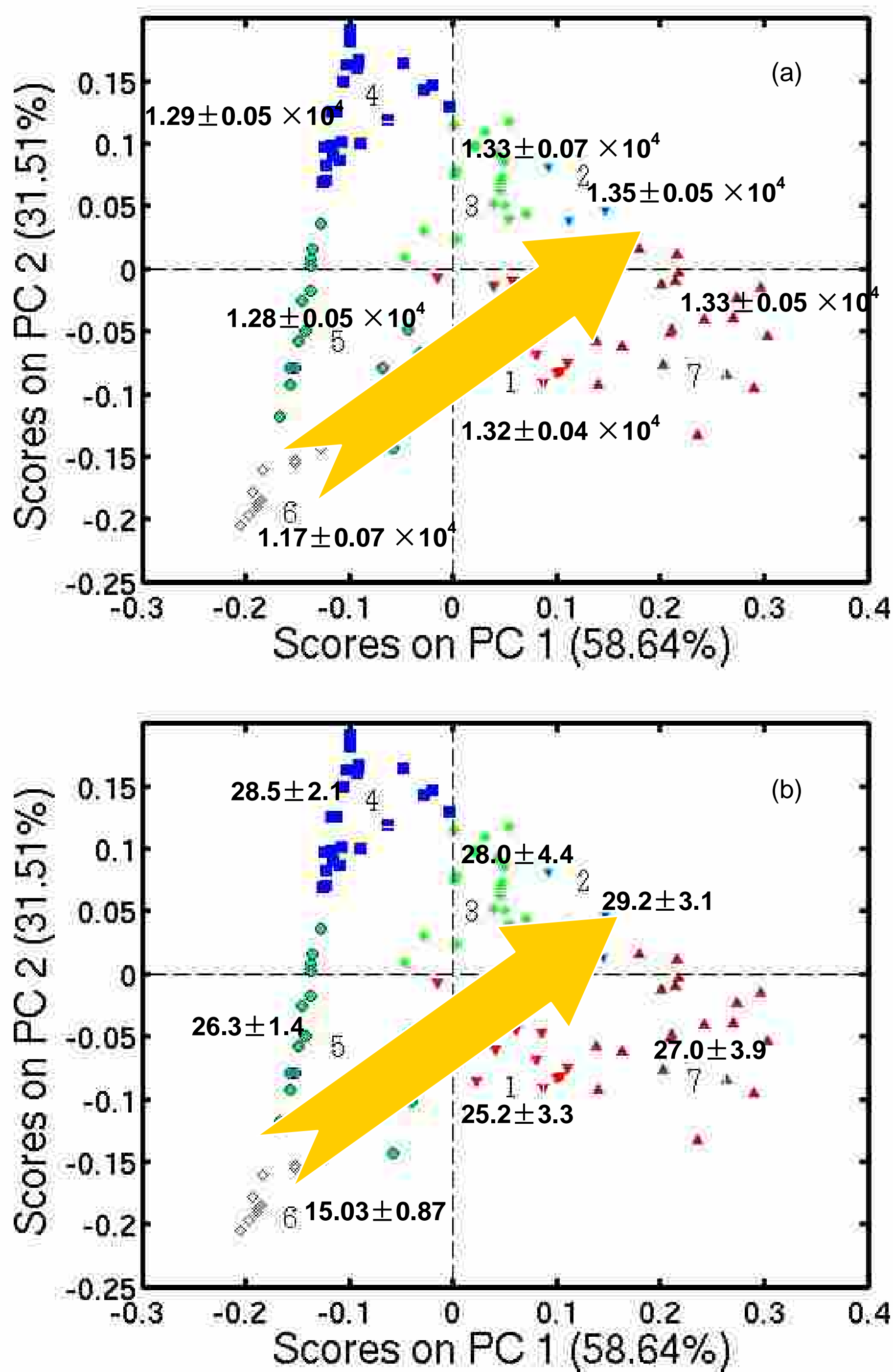

Figure 5.8. (a) PC1 vs. PC2 plot showing the average heating value of the samples found in each of the seven clusters in the dendrogram, and (b) PC1 vs. PC2 plot showing the average percent Al_2O_3 composition of the samples found in each of the seven clusters in the dendrogram. The yellow arrows are guides to the eye.

Partial least squares (PLS) regression analysis[16] was performed to better understand the relationship between the spectra and the properties of the coal samples measured by conventional means. Two preprocessing methods were considered: (1) normalization and square root transformation (appropriate for Poisson distributed data), followed by mean centering of the spectra and the properties, and (2) the same preprocessing of the spectral data, but log 10 scaling of the properties prior to mean centering. When the number of latent variables for both preprocessing methods is the same, the first method usually provides slightly better R^2 values.

The R^2 values presented in Table 5.5 were obtained using all of the spectra in the matrix, including those whose properties were to be predicted in the regression analysis. While these numbers are useful, a better measure of the success of PLS would be the R^2 value from a plot of the measured property vs. the CV (cross-validation) predicted property, where the CV predicted property is the value that is predicted in a model that excludes the data that is being predicted. When this more stringent constraint is placed on the analysis, the R^2 values decrease substantially. For example, for the volatile matter and oxygen, the R^2 values decreased from 0.92 and 0.95 to 0.63 and 0.65, respectively. That is, PLS still shows that a correlation exists between the spectra and these properties, but the correlations are not as tight as initially suggested.

Because a number of the ToF-SIMS spectral regions contain mostly noise, it was thought that a variable reduction scheme might further improve these correlations to some degree. Interval PLS (iPLS)[39] was then performed on the data, which suggested that the higher mass ions had less impact on the PLS model than the lower mass ions. For example, by excluding the last 50 variables from the PLS analysis, it was found that the R^2 values (for the CV predicted property) for the volatile matter and oxygen content of the samples could be modestly improved to 0.64 and 0.69, respectively (keeping the same number of latent variables as before.)

Further improvement in the R^2 values was still possible. Based on my intuition that most of the information would be in the low mass ions, and also the results from the iPLS analysis, it seemed reasonable to focus on the lower mass regions. Therefore, the variables from 0.5 to 150 m/z were used in a genetic algorithm that would perform variable selection.[40-41] Using the same conditions for PLS analysis (preprocessing by mean centering, cross validation performed with 9 splits of contiguous blocks),[42] I found that after 200 generations, the number of variables was reduced and the best model with the best fitness could be saved for PLS analysis. For example, for the volatile matter property, the variables were reduced from 300 to 50, and R^2 of the CV predicted property was 0.91, while for the oxygen percentage, the variables were reduced to 70 and R^2 was 0.90. These results (see Figure 5.9) suggest that with appropriate variable selection, the R^2 values given in Table 5.5 for the PLS analysis (without cross validation or use of the genetic algorithm) would be approximately equal to those for the CV predicted property. Indeed, this supposition was confirmed for all of the properties (see Table 5.5).

This analysis further suggests that there may be a number of sample properties that will correlate well with the ToF-SIMS spectra. That is, one could take a few ToF-SIMS spectra from a material and estimate a number of sample properties using robust models. The lack of high correlation coefficients in some cases in Table 5.5 may result primarily from a lack of simple linear correlation between the PCA results and the traditional analyses and not a lack of correlation of any type. Uncovering quantitative and especially mechanistic relationships between fuel behavior and these types of spectral results will require substantial additional analysis, but the qualitative correlations indicated here show promise of providing correlations with traditional analyses and, much more importantly, providing analytical capabilities beyond those of traditional analyses.

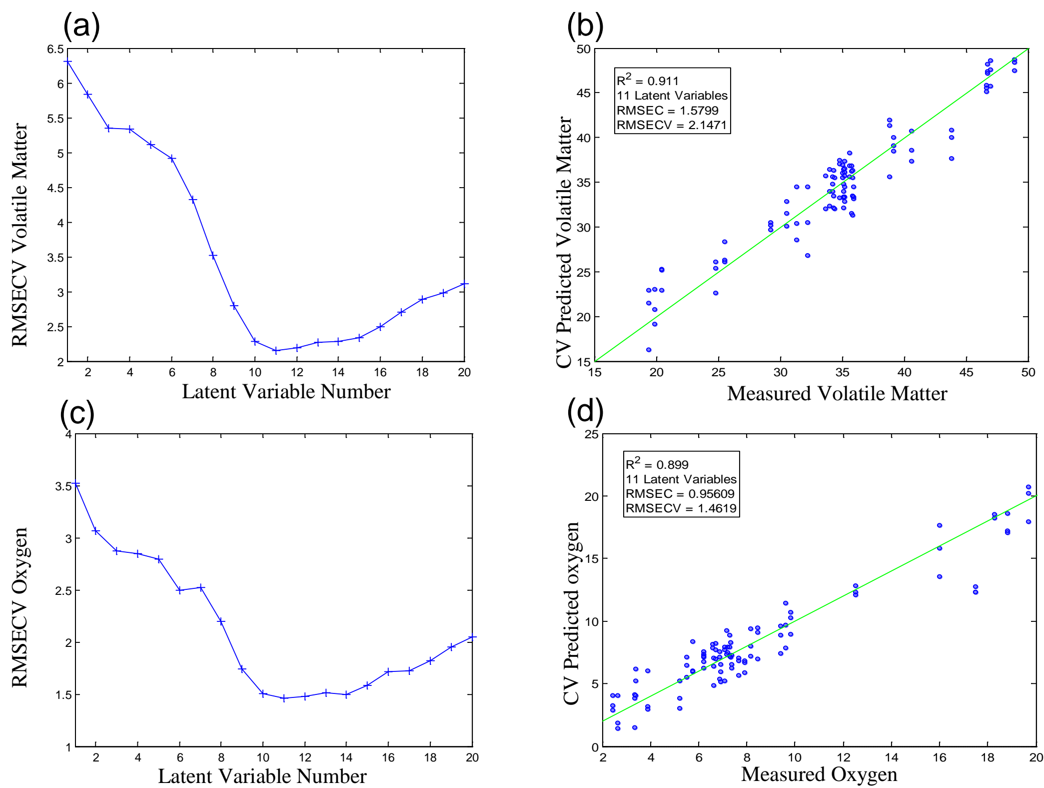

Figure 5.9: PLS results for volatile matter and oxygen. (a) and (c) show the RMSECV plots that were used to determine the number of latent variables, and (b) and (d) show the CV predicted vs. measured properties.

Table 5.5. Conventional properties that were measured for each coal sample along with PLS results.

Property	Preprocessing method 1 CorrCoef $R^{2\,a}$	CV predicted CorrCoef $R^{2\,b}$	After GA, CV predicted CorrCoef $R^{2\,c}$
Moisture	0.70 (3)	0.53 (3)	0.73 (3)
Volatile Matter	0.92 (11)	0.63 (11)	0.91 (11)
Ash	0.30 (1)	0.08 (1)	0.38 (1)
Carbon	0.68 (5)	0.38 (5)	0.62 (5)
Hydrogen	0.56 (5)	0.26 (5)	0.48 (4)
Nitrogen	0.76 (4)	0.54 (4)	0.67 (4)
Sulfur	0.58 (5)	0.30 (5)	0.52 (4)
Heating Value	0.63 (3)	0.44 (3)	0.62 (4)
Chlorine	0.09 (1)	0.00 (1)	0.04 (1)
Oxygen	0.95 (12)	0.65 (12)	0.90 (11)
H:C	0.96 (12)	0.65 (12)	0.93 (11)
O:C	0.65 (5)	0.42 (5)	0.61 (5)
SiO_2	0.59 (3)	0.32 (3)	0.58 (3)
Al_2O_3	0.71 (3)	0.53 (3)	0.74 (3)
TiO_2	0.60 (5)	0.41 (5)	0.53 (5)
Fe_2O_3	0.51 (6)	0.19 (6)	0.35 (4)
CaO	0.81 (4)	0.62 (4)	0.79 (2)
MgO	0.76 (4)	0.54 (4)	0.74 (3)
Na_2O	0.75 (4)	0.59 (4)	0.72 (4)
K_2O	0.92 (12)	0.64 (12)	0.85 (10)
P_2O_5	0.09 (1)	0.00 (1)	0.06 (1)
SO_3	0.62 (3)	0.40 (3)	0.63 (2)
Reducing Initial	0.65 (5)	0.41 (5)	0.68 (12)
Reducing H=W	0.63 (4)	0.42 (4)	0.65 (9)
Reducing H=1/2W	0.74 (6)	0.48 (6)	0.77 (10)
Reducing Fluid	0.77 (6)	0.50 (6)	0.78 (6)
Oxidizing Initial	0.80 (6)	0.55 (6)	0.76 (11)
Oxidizing H=W	0.99 (20)	0.58 (20)	0.97 (20)
Oxidizing H=1/2W	0.64 (3)	0.49 (3)	0.64 (3)
Oxidizing Fluid	0.99 (20)	0.59 (20)	0.97 (20)
Difference Initial	0.05 (1)	0.01 (1)	0.03 (1)
Difference H=W	0.13 (2)	0.01 (2)	0.14 (2)
Difference H=1/2W	0.06 (1)	0.00 (1)	0.05 (1)
Difference Fluid	0.19 (3)	0.01 (3)	0.21 (3)
Iron Content	0.51 (6)	0.19 (6)	0.35 (4)

[a]shows the R^2 values for a PLS analysis, [b]shows the R^2 values for PLS with cross validation, and [c]shows the R^2 values for a PLS analysis with cross validation after variable selection using a genetic algorithm. The number of latent variables in each PLS analysis is given in brackets. In the first preprocessing method the spectra were normalized, square root transformed, and mean centered, while the properties were mean centered. In the second preprocessing method the spectra were normalized, square root transformed, and mean centered, while the log 10 of the properties were taken before they were mean centered. In a few cases for the second preprocessing method, one or more of the values of a property was zero in which case the log 10 could not be taken, i.e., PLS under these conditions was not possible.

Table 5.5. continued.

Property	Preprocessing method 2 CorrCoef R^2	CV predicted CorrCoef R^2	After GA, CV predicted CorrCoef R^2
Moisture	0.92 (9)	0.33 (9)	0.68 (12)
Volatile Matter	0.91 (11)	0.57 (11)	0.90 (12)
Ash	0.26 (1)	0.09 (1)	0.35 (1)
Carbon	0.68 (5)	0.38 (5)	0.60 (5)
Hydrogen	0.55 (5)	0.24 (5)	0.37 (3)
Nitrogen	0.74 (4)	0.56 (4)	0.69 (3)
Sulfur	0.58 (5)	0.32 (5)	0.51 (5)
Heating Value	0.63 (3)	0.44 (3)	0.62 (3)
Chlorine	0.90 (19)	0.08 (19)	0.39 (19)
Oxygen	0.93 (11)	0.60 (11)	0.84 (12)
H:C	0.93 (11)	0.60 (11)	0.83 (11)
O:C	0.64 (5)	0.41 (5)	0.60 (5)
SiO_2	0.57 (3)	0.30 (3)	0.57 (3)
Al_2O_3	0.69 (3)	0.52 (3)	0.76 (3)
TiO_2	0.58 (5)	0.41 (5)	0.52 (5)
Fe_2O_3	0.50 (7)	0.20 (7)	0.32 (5)
CaO	0.99 (18)	0.47 (18)	0.85 (20)
MgO	0.77 (4)	0.54 (4)	0.74 (4)
Na_2O	0.78 (3)	0.61 (3)	0.66 (3)
K_2O	0.86 (12)	0.66 (12)	0.81 (10)
P_2O_5	0.20 (4)	0.02 (4)	0.13 (3)
SO_3	0.57 (3)	0.44 (3)	0.64 (9)
Reducing Initial	0.68 (6)	0.42 (6)	0.72 (8)
Reducing H=W	0.56 (3)	0.41 (3)	0.61 (3)
Reducing H=1/2W	0.60 (3)	0.46 (3)	0.65 (3)
Reducing Fluid	0.69 (4)	0.50 (4)	0.74 (7)
Oxidizing Initial	0.98 (18)	0.57 (18)	0.96 (18)
Oxidizing H=W	0.99 (20)	0.58 (20)	0.96 (20)
Oxidizing H=1/2W	0.63 (3)	0.49 (3)	0.66 (4)
Oxidizing Fluid	0.99 (18)	0.60 (18)	0.74 (7)
Difference Initial	--	--	--
Difference H=W	--	--	--
Difference H=1/2W	--	--	--
Difference Fluid	--	--	--
Iron Content	0.50 (7)	0.204 (7)	0.32 (5)

5.5 Conclusions

A large data set of multiple coal samples spanning a wide range of coal properties has been analyzed by ToF-SIMS. The inorganic components often overshadow the organic components of these spectra. A chemometrics analysis of the resulting spectra was performed. PCA and cluster analysis consistently separate the spectra into clusters that correspond with characteristic combustion behaviors of different coal ranks. The success of the PCA analysis to separate the samples into classical fuel properties indicates that the ToF-SIMS data include quantitative indications of commercially significant fuel properties. This paper documents qualitative and in some cases quantitative correspondence between these properties. However, the most important conclusion is that the advanced techniques illustrated here may provide chemical (as opposed to elemental) information that corresponds to important combustion behaviors. Many of these combustion behaviors typically are not well correlated with traditional analyses. The results of this paper suggest this technique could provide analytical results that will advance predictive capabilities for combustion and gasification of coals.

Future work should include the analysis a series of coal samples using some of the latest cluster ion sources. I believe that this newer SIMS technology will produce more highly characteristic organic ions, which will give even better regression results.

5.6 Acknowledgment

I gratefully acknowledge Alliant Power Systems, Southern Company, and Tennessee Valley Authority for supplying fuel samples. Financial support for this work comes from a variety of industrial sponsors of LLB research.

5.7 References

1. *ToF-SIMS. Surface Analysis by Mass Spectrometry*. IM Publications: Huddersfield, UK, 2001.

2. Mowat, I. A.; Lindley, P. M.; Reich, F., Polymer surface analysis using time-of-flight secondary ion mass spectrometry (TOF-SIMS). *Abstr. Pap. Am. Chem. Soc.* **1998,** *215*, U298-U298.

3. Peterson, R. E.; Tyler, B. J., Analysis of organic and inorganic species on the surface of atmospheric aerosol using time-of-flight secondary ion mass spectrometry (TOF-SIMS). *Atmos. Environ.* **2002,** *36* (39-40), 6041-6049.

4. Pei, L.; Jiang, G. L.; Davis, R. C.; Shaver, J. M.; Smentkowski, V. S.; Asplund, M. C.; Linford, M. R., Laser activation-modification of semiconductor surfaces (LAMSS) of 1-alkenes on silicon: A ToF-SIMS, chemometrics, and AFM analysis. *Appl. Surf. Sci.* **2007,** *253* (12), 5375-5386.

5. Yang, L.; Shirahata, N.; Saini, G.; Zhang, F.; Pei, L.; Asplund, M. C.; Kurth, D. G.; Ariga, K.; Sautter, K.; Nakanishi, T.; Smentkowski, V.; Linford, M. R., Effect of Surface Free Energy on PDMS Transfer in Microcontact Printing and Its Application to ToF-SIMS to Probe Surface Energies. *Langmuir* **2009,** *25* (10), 5674-5683.

6. Brereton, R. G., *Chemometrics. Data Analysis for the Laboratory and Chemical Plant.* John Wiley & Sons, Ltd.: Chichester, 2003.

7. Kramer, R., *Chemometric Techniques for Quantitative Analysis*. Marcel Dekker: New York, 1998.

8. Massart, D. L., *Chemometrics: a textbook*. Elsevier: Amsterdam; Oxford, 1988.

9. Wagner, M. S.; Graham, D. J.; Ratner, B. D.; Castner, D. G., Maximizing information obtained from secondary ion mass spectra of organic thin films using multivariate analysis. *Surf. Sci.* **2004,** *570*, 78-97.

10. Yang, L.; Lua, Y.-Y.; Jiang, G.; Tyler, B. J.; Linford, M. R., A Multivariate Analysis of ToF-SIMS Spectra of Monolayers on Scribed Silicon. *Anal. Chem.* **2005,** *77* (14), 4654-4661.

11. Graham, D. J.; Ratner, B. D., Multivariate Analysis of TOF-SIMS Spectra from Dodecanethiol SAM Assembly on Gold: Spectral Interpretation and TOF-SIMS Fragmentation Processes. *Langmuir* **2002,** *18*, 5861-5868.

12. Wang, H.; Castner, D. G.; Ratner, B. D.; Jiang, S., Probing the Orientation of Surface-Immobilized Immunoglobulin G by Time-of-Flight Secondary Ion Mass Spectrometry. *Langmuir* **2004,** *20*, 1877-1887.

13. Wagner, M. S.; Pasche, S.; Castner, D. G.; Textor, M., Characterization of poly(L-lysine)-graft-poly(ethylene glycol) assembled monolayers on niobium pentoxide substrates using time-of-flight secondary ion mass spectrometry and multivariate analysis. *Anal. Chem.* **2004,** *76* (5), 1483-1492.

14. Beebe, K. R.; Pell, R. J.; Seasholtz, M. B., *Chemometrics: A Practical Guide*. John Wiley & Sons: New York, NY, 1998.

15. Jackson, J. E., *A User's Guide to Principal Components*. Wiley-Interscience: 2003.

16. Wold, S.; Ruhe, A.; Wold, H.; Dunn, W. J., The Collinearity Problem in Linear-Regression - the Partial Least-Squares (Pls) Approach to Generalized Inverses. *SIAM J. Sci. Stat. Comp.* **1984,** *5* (3), 735-743.

17. Otto, M., *Chemometrics: Statistics and Computer Application in Analytical Chemistry*. Wiley-VCH: Weiheim, 1999.

18. Jolliffe, I. T., *Principal component analysis*. Springer-Verlag: New York, 1986.

19. Aldenderfer, M. S.; Blashfield, R. K., *Cluster analysis*. Sage Publications: Beverly Hills, 1984.

20. Esposito Vinzi, V., *Handbook of partial least squares: concepts, methods and applications*. Springer: Berlin; London, 2010.

21. Sakamoto, T.; Shibata, K.; Takanashi, K.; Owari, M.; Nihei, Y., Structural Analysis of Coal Fly Ash Particles by means of Focused-Ion-Beam Time-of-Flight Mass Spectrometry. *e-J. Surf. Sci. Nanotech.* **2004,** *2*, 45-51.

22. Gong, B.; Pigram, P. J.; Lamb, R. N., Surface Composition of Silica Particles Embedded in an Australian Bituminous Coal. *Appl. Occup. Environ. Hyg.* **1999,** *14*, 481-489.

23. Domazetis, G.; Raoarun, M.; James, B. D.; Liesegang, J., Studies of Mono- and Polynuclear Iron Hydroxy Complexes in Brown Coal. *Energ. Fuel* **2005,** *19*, 1047-1055.

24. Domazetis, G.; Raoarun, M.; James, B. D.; Liesegang, J.; Pigram, P. J.; Brack, N.; Glaisher, R., Analytical and Characterization Studies of Organic and Inorganic Species in Brown Coal. *Energ. Fuel* **2006,** *20*, 1556-1564.

25. Zhan, D. L.; Fenn, J. B., Electrospray mass spectrometry of fossil fuels. *Int. J. Mass Spectrom.***2000,** *194* (2-3), 197-208.

26. Wu, Z. G.; Jernstrom, S.; Hughey, C. A.; Rodgers, R. P.; Marshall, A. G., Resolution of 10,000 compositionally distinct components in polar coal extracts by negative-ion electrospray ionization Fourier transform ion cyclotron resonance mass spectrometry. *Energ. Fuel* **2003,** *17* (4), 946-953.

27. Wu, Z. G.; Rodgers, R. P.; Marshall, A. G., Compositional determination of acidic species in Illinois no. 6 coal extracts by electrospray ionization Fourier transform ion cyclotron resonance mass spectrometry. *Energ. Fuel* **2004,** *18* (5), 1424-1428.

28. Marshall, A. G.; Rodgers, R. P., Petroleomics: The next grand challenge for chemical analysis. *Acc. Chem. Res.* **2004,** *37* (1), 53-59.

29. Roussis, S. G.; Fedora, J. W., Quantitative determination of polar and ionic compounds in petroleum fractions by atmospheric pressure chemical ionization and electrospray ionization mass spectrometry. *Rapid Commun. Mass Spectrom.* **2002,** *16* (13), 1295-1303.

30. Porter, D. J.; Mayer, P. M.; Fingas, M., Analysis of petroleum resins using electrospray ionization tandem mass spectrometry. *Energ. Fuel* **2004,** *18* (4), 987-994.

31. Eide, I.; Zahlsen, K., A Novel Method for Chemical Fingerprinting of Oil and Petroleum Products Based on Electrospray Mass Spectrometry and Chemometrics *Energ. Fuel* **2005,** *19* (3), 964-967.

32. Tyler, B.J. unpublished results

33. Wold, S., Cross-Validatory Estimation of Number of Components in Factor and Principal Components Models. *Technometrics* **1978,** *20* (4), 397-405.

34. Wise, B. M.; Gallagher, N. B.; Bro, R.; Shaver, J. M.; Windig, W.; Koch, R. S., PLS_Toolbox 4.0 for use with MATLAB. *PLS_Toolbox 4.0 for use with MATLAB*.

35. Wise, B. M.; Ricker, N. L., Recent Advances in Multivariate Statistical Process Control: Improving Robustness and Sensitivity. *IFAC Symposium on Advanced Control of Chemical Processes* **1991**, 125-130.

36. Wagner, M. S.; Pasche, S.; Castner, D. G.; Textor, M., Characterization of Poly(L-lysine)-graft-Poly(ethylene glycol) Assembled Monolayers on Niobium Pentoxide Substrates

Using Time-of-Flight Secondary Ion Mass Spectrometry and Multivariate Analysis. *Anal Chem.* **2004,** *76*, 1483-1492.

37. Pei, L.; Jiang, G.; Davis, R. C.; Shaver, J. M.; Smentkowski, V. S.; Asplund, M. C.; Linford, M. R., Laser activation-modification of semiconductor surfaces (LAMSS) of 1-alkenes on silicon: A ToF-SIMS, chemometrics, and AFM analysis. *Appl. Surf. Sci.* **2007**.

38. Smentkowski, V. S.; Keenan, M. R.; Ohlhausen, J. A.; Kotula, P. G., Multivariate Statistical Analysis of Concatenated Time-of-Flight Secondary Ion Mass Spectrometry Spectral Images. Complete Description of the Sample with One Analysis. *Anal. Chem.* **2005,** *77* (5), 1530-1536.

39. Nørgaard, L.; Saudland, A.; Wagner, J.; Nielsen, J. P.; Munck, L.; Engelsen, S. B., Interval Partial Least-Squares Regression (iPLS): A Comparative Chemometric Study with an Example from Near-Infrared Spectroscopy. *Appl. Spectrosc.* **2000,** *54* (3), 413-419.

40. Leardi, R., Application of a genetic algorithm to feature selection under full validation conditions and to outlier detection. *J. Chemometr.* **1994,** *8* (1), 65-79.

41. Leardi, R.; Boggia, R.; Terrile, M., Genetic algorithms as a strategy for feature selection. *J. Chemometr.* **1992,** *6* (5), 267-281.

42. Note that the spectral dataset for this analysis was the same as that used in the previous PLS analyses, except that it underwent some reorganization to insure that spectra from similar coal samples were not entirely removed from a given contiguous block during cross validation.

Chapter 6 Carbon Nanotube Functionalization with Peroxides

6.1 Abstract

Carbon nanotubes (CNTs) have little or no solubility in most solvents, and even dispersion of CNTs can be challenging. However, the solubility/dispersability of CNTs can often be substantially improved by functionalizing them. Here I investigate the chemical modification of carbon nanotubes with peroxides. Single-walled nanotubes (SWNT) were purified, dispersed, and reacted with two types of peroxides: succinic acid acyl peroxide and di-*tert*-amyl peroxide. The functionalized carbon nanotubes were filtrated into a bucky paper form, and finally analyzed by X-ray photoelectron spectroscopy (XPS) and water contact angle measurements.

6.2 Introduction

Carbon nanotubes (CNTs), discovered by Iijima in the early 1990's,[1] have played a very important role in nanotechnology. Carbon nanotubes have cylindrical, graphitic structures, which are based on a hexagonal, sp^2, arrangement of carbon atoms.[2] Due to their unique structures, carbon nanotubes have many remarkable mechanical and electrical properties. There are two main classes of carbon nanotubes: single-walled nanotubes (SWNTs) and multi-walled nanotubes (MWNTs), where this classification is based on the number of outside graphitic layers they contain. Normally, a SWNT is several micrometers in length and a few nanometers in diameter, which gives it a large surface area with a very high length to diameter ratio.[3]

Carbon nanotubes are one of the strongest of all materials because their skeleton is formed of conjugated sp^2 carbon bonds.[2] Their mechanical properties are usually described by their tensile strength and Young's modulus. The tensile strength is the maximum amount of tensile stress that a material can be subjected to before it breaks. The Young's modulus, which is

defined as the ratio of tensile stress to tensile strain, measures the tendency of a material to elastically deform along an axis where opposing forces are applied.[4] SWNTs have about 100 GPa tensile strength and 1 TPa Young's modulus, which is fifty and five times higher than steel, respectively.[3, 5] SWNTs are excellent thermal conductors, having a thermal conductivity along the tube ca. 15 times greater than copper.[6] Based on their structure, carbon nanotubes can be either metallic or semiconducting. Metallic carbon nanotubes can support a very high electrical current density.[7] CNTs also have other properties such as low weight, chemical inertness, and good stability in vacuum, air, and at high temperature that should make them valuable in many applications.

A number of difficulties are associated with manipulation of CNTs. The low solubility of CNTs in almost all organic and aqueous solvents has been noted, where this challenge extends to pristine CNTs. Carbon nanotubes tend to entangle and form bundles that are hexagonally packed due to van der Waals interactions.[12] Moreover, it is usually difficult to detect and control individual CNTs and CNT bundles by analytical instruments because CNTs exist at such a small scale. In order to better study these materials, nanotube sheets or "bucky papers"[13] which contain large numbers of SWNTs can be made by vacuum filtration; surface characterization can be easily performed on these bucky papers.

CNT purification is important for removing impurities that are almost invariably introduced during synthesis. SWNTs can be produced by several techniques including arc discharge,[1] laser ablation,[8] chemical vapor deposition (CVD) from hydrocarbon precursors,[9] and high pressure CO disproportionation (HiPco),[10] Metal nanoparticles made of Fe, Ni, or Co are used as catalysts in most of these processes and often end up trapped within SWNT bundles. In general, the tubes are also contaminated with several other types of carbonaceous materials

including graphite nanoparticles, amorphous carbon, and fullerenes. It is clear that for many applications, raw CNTs require some sort of purification.

Since carbon nanotubes are insoluble in water and organic solvents, sonication is used to disperse them and also break up nanotube bundles to obtain homogenous and stable suspensions of (mostly) individual carbon nanotubes.[11] A few solvents have been used for this purpose. For pristine CNTs, the solvent can be water with a surfactant such as sodium dodecyl sulfate (SDS) or Triton X ($C_{14}H_{22}O(C_2H_4O)_n$), dichlorobenzene, 1,2-dichloroethane, dimethylformamide (DMF), *N*-methyl-2-pyrrolidone (NMP), etc. For carboxyl terminated CNTs (CNT-COOH), water, with or without a surfactant, has primarily been used. For CNT/polymer composite solutions, CNTs have been added directly to the polymer and then dispersed; polymer solutions have included PVA in water, polystyrene in dichlorobenzene, and polyimide in NMP. Polymer molecules may act as surfactants in their dispersion of CNT molecules. After sonication, CNT solutions are usually centrifuged to precipitate non-dispersed CNTs and obtain more homogenous CNT-solvent supernatants.

Although carbon nanotubes exhibit good chemical inertness, a variety of carbon nanotube functionalization methods have been demonstrated.[14-22] For example, the reactions of SWNTs with alkyl or aryl peroxides have been shown.[23-29] Upon heating, these peroxides decompose and the resulting radicals add in a nondestructive fashion to SWNT side walls. These types of reactions are advantageous for several reasons. First, side-wall reactions introduce chemical moieties along the tubes, which is advantageous because this can substantially modify their solubility. Second, these reactions do not open the caps of nanotubes or break the tubes. Third, these reactions can take place in a single step. Fourth, these experiments are generally easy to set up and perform.

In my work, I have focused on functionalization of CNTs with two types of peroxides: succinic acid acyl peroxide and di-*tert*-amyl peroxide. There are a number of reports in the literature related to this approach,[23-29] Indeed, the reaction of succinic acid acyl peroxide with SWNTs has been reported.[23] In my work, I repeated this earlier study and provided additional characterization by XPS and water contact angle measurements. Functionalization of CNTs with di-*tert*-amyl peroxide had not yet been reported. This study involved CNT purification, CNT functionalization, and CNT bucky paper formation for material characterization.

6.3 Experimental

6.3.1 CNT purification

The raw SWNTs used in my work were commercially obtained from Carbon Nanotechnologies. These SWNTs were produced by the HiPco process in high purity (>90%). The impurities, including the metal catalyst, can be removed as illustrated in the following procedure: raw SWNTs (20 mg) were placed into a round bottom flask with 50 mL deionized (Millipore) water. The solution was sonicated for 5 min to disperse the SWNTs. Concentrated HCl (37%, 50 mL) was added to this black solution. The solution was then refluxed under continuous magnetic stirring for 12 h and cooled to room temperature. SWNTs were filtered on a 1 µm polytetrafluoroethylene (PTFE) filter, rinsed with large amounts of DI (Millipore) water and dried in an oven at 80°C for 1 h.

6.3.2 CNT functionalization

First, the succinic acid acyl peroxide was prepared. Succinic anhydride (10 g) was ground into a fine powder, added to 20 mL of ice cold 8% hydrogen peroxide, stirred for 30 min, filtered onto PTFE filter paper, rinsed with a small amount of DI water, and air-dried for 10 min. The

white peroxide was then collected in a glass vial and vacuum dried at room temperature for 24 h. It was then ready for use.

The reaction between this compound and the nanotubes was then performed. Purified SWNTs (50 mg) were added to 50 mL of dry *o*-dichlorobenzene in a 250 mL flask and sonicated for 30 min. The dark solution was heated at 90°C with stirring for 10 days. Succinic acid acyl peroxide (0.5 g) was added to the solution each day. After 10 days, the solution was cooled to room temperature. A large amount of tetrahydrofuran (THF) was added, and the solution was sonicated for 15 min. The resulting solution was filtered on PTFE filter paper and rinsed with ethanol to wash off the unreacted peroxides and other byproducts. Finally, the functionalized SWNTs were vacuum-dried at 80°C overnight and peeled off the filter paper.

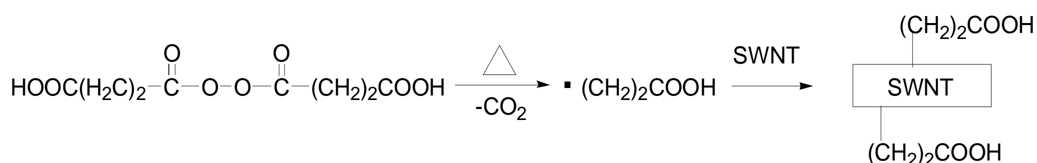

To further investigate the reaction of SWNTs with peroxides, a shorter reaction time with less solution preparation would be advantageous. Di-*tert*-amyl peroxide (97%), which is commercially available from Aldrich, was allowed to react with SWNTs for 24 h. Di-*tert*-amyl peroxide, $C_2H_5C(CH_3)_2OOC(CH_3)_2C_2H_5$, is a colorless liquid with a half life at 123.3°C of 10 h and at 143.1°C of 1 h. For the reaction, 5 mg purified SWNTs were dispersed in 10 mL *N,N*-dimethylformamide (DMF) in a 100 mL three neck flask with 5 min of sonication. Di-*tert*-amyl peroxide (10 mL) was added. The solution was bubbled with nitrogen gas for 30 min to remove oxygen, and it was then heated to about 140°C with stirring and refluxing under nitrogen. During the reaction, the bond between the oxygen atoms of the peroxide breaks and two reactive oxygen radicals are produced that can attack the side walls of the SWNTs. After 12 h, the peroxide

should be mostly reacted, and 10 mL di-*tert*-amyl peroxide was added into the solution for another 12 h. When the reaction was completed, the solution was cooled, filtered on a PTFE filter, and rinsed with a large amount of chloroform. The resulting bucky paper was dried at 80°C in an oven before analysis. Two control samples were prepared under the same reaction conditions, but without peroxide.

6.3.3 X-ray photoelectron spectroscopy (XPS) analysis

XPS (Surface Science SSX-100) analyses were performed on CNT bucky papers prepared as purified samples, functionalized samples, and control samples.

6.4 Results and Discussion

6.4.1 CNT bucky paper formation

CNT bucky papers were produced multiple times after CNT purification and functionalization. Figure 6.1 shows photos of thick and thin bucky papers and SEM images of these samples at horizontal and vertical views. From these images, we observed that nanotube sheets are quite porous, which may provide a very large adsorptive capacity for analytes, and that they can be handled with tweezers and cut with scissors or laser beams. The thicknesses of nanotube sheets are controllable; based on the amount of CNT material introduced, bucky papers can be made as ca. 50 nm transparent films[30] to about 40 µm free-standing layers (a paper). These bucky papers alone can lead to many different applications, e.g., the project described in Chapter 3. For this project they are mainly used for surface analyses due to their flatness and ease of manipulation.

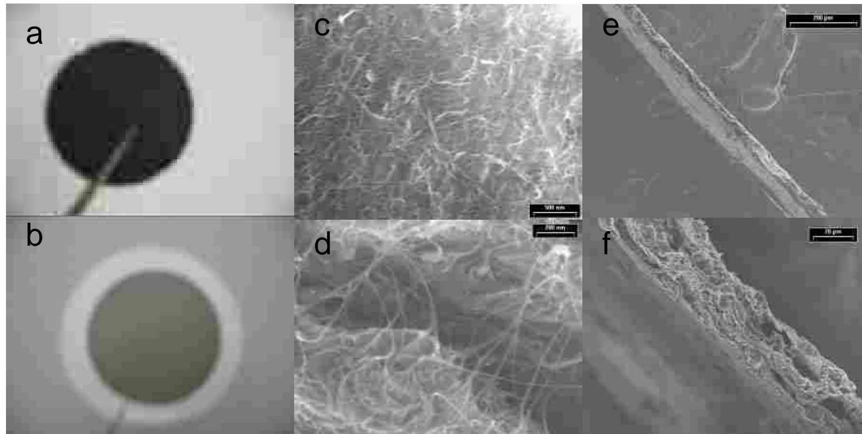

Figure 6.1. (Left) photos of bucky paper, (a) free standing, thick bucky paper, and (b) transparent, thin bucky paper on filter paper; (middle) SEM images of thick bucky paper viewed horizontally, (c) with 500 mm scale bar, and (d) with 200 nm scale bar at high resolution; (right) SEM images of thick bucky paper viewed vertically, (e) with 200 µm scale bar, and (f) with 20 µm scale bar at high resolution.

6.4.2 CNT purification

During the filtration of purified CNTs into bucky paper, the color of the filtrate was brown, which suggests that the large iron particles that were initially present were mostly removed. Although some impurities may still remain as nanoparticles within the CNT bundles, we can obtain reproducible XPS results of this material (see Figure 6.2). The survey spectra show that there are three major components: carbon (C1s) at 285 eV, oxygen (O1s) at 531 eV and iron (Fe2p) at 707 eV, with area percentages of ca. 94%, 5% and 1%, respectively. The amount of iron is significantly lower than that claimed for raw CNTs (ca. 10%). However, note that compared to other purification methods like high temperature annealing,[31-32] this particular procedure does not tend to remove other types of carbon. Nevertheless, we do not believe that their removal is critical for our applications because these other forms of carbon, such as amorphous carbon, can also be functionalized and act as bridges in the cross-linking process. Some oxidization can also be used to further remove the metal particles, but we do not favor this approach because it can also open the caps of SWNTs and attack defective sites that they may have.

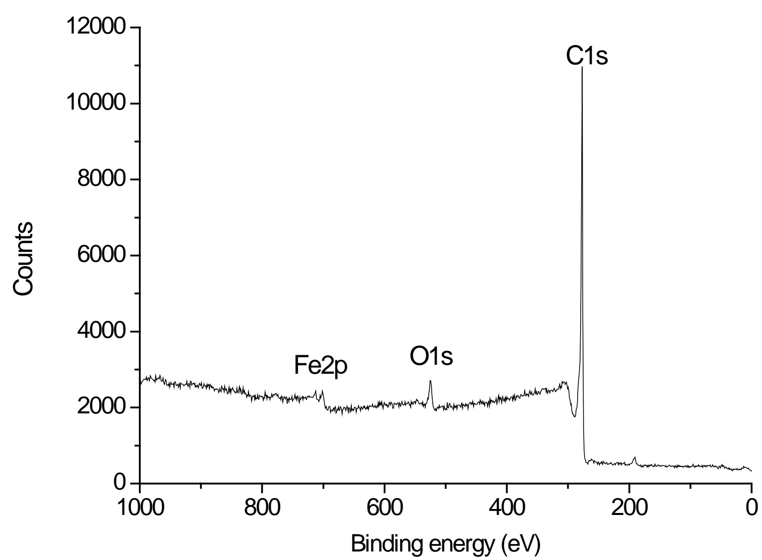

Figure 6.2. XPS survey spectrum of purified single-walled carbon nanotubes produced by the HiPco process.

6.4.3 CNT functionalization

Although the reaction of succinic acid acyl peroxide with SWNTs has previously been reported,[23] we are not aware of any XPS characterization of the resulting material. Accordingly, the bucky paper prepared from succinic acid aryl peroxide functionalized SWNTs (s-SWNTs) was analyzed by XPS. Figure 6.3a shows that the oxygen peak is significantly increased compared to the untreated SWNT control sample, which suggests that a reaction has occurred. The narrow scan of the C1s peak in Figure 6.3b shows two major components: one at ca. 284.5 eV corresponding to C-C and C-O bonds, and another at 289 eV from -C(O)O (not observed in the control sample), which is shifted ca. 4.5 eV from the C-C component. Moreover, when a small droplet of water was placed on the surface of the control sample, the contact angle between the droplet and untreated nanotubes was approximately 70°, and the water droplet can be easily blown off from this hydrophobic surface. However, the contact angle between the droplet and the s-SWNTs was reduced to 25-30° after the reaction with the peroxide, i.e., water nearly wets the surface and is hard to remove. All of these results point to a successful reaction.

Figure 6.4 shows the XPS results of the di-*tert*-amyl peroxide functionalized SWNTs (t-SWNTs). The survey scans show that the O1s peak area of t-SWNTs is increased (approximately doubled) compared to the control (see Table 6.1). According to basic XPS theory of carbon-containing materials, carbon atoms bonded to oxygen will have a ca. 1.2 eV shift towards higher binding energy from the main C1s peak. By fixing the difference between two components as 1.2 eV, the large C1s peak can be curve fitted to two components: C-O and C-C. Table 6.1 gives the areas for these peaks and shows that the C-O component has increased after the reaction. All of these results suggest that di-*tert*-amyl peroxide has reacted with carbon nanotubes. We also note

that an N1s signal appears in the XPS spectra of t-SWNTs, which suggests that DMF (the solvent) may be involved to some degree in the reaction.

6.5 Conclusions

We have modified SWNTs with succinic acid aryl peroxide or di-*tert*-amyl peroxide. The XPS survey scans on both of these peroxide functionalized SWNTs show increased oxygen signals compared to their untreated SWNT controls. Moreover, XPS C1s narrow scans on succinic acid aryl peroxide functionalized SWNTs show an additional carboxyl component. XPS C1s narrow scans of di-*tert*-amyl peroxide functionalized SWNTs also show an increased percentage of the C-O component. All of these results suggest that both of the reactions were successful.

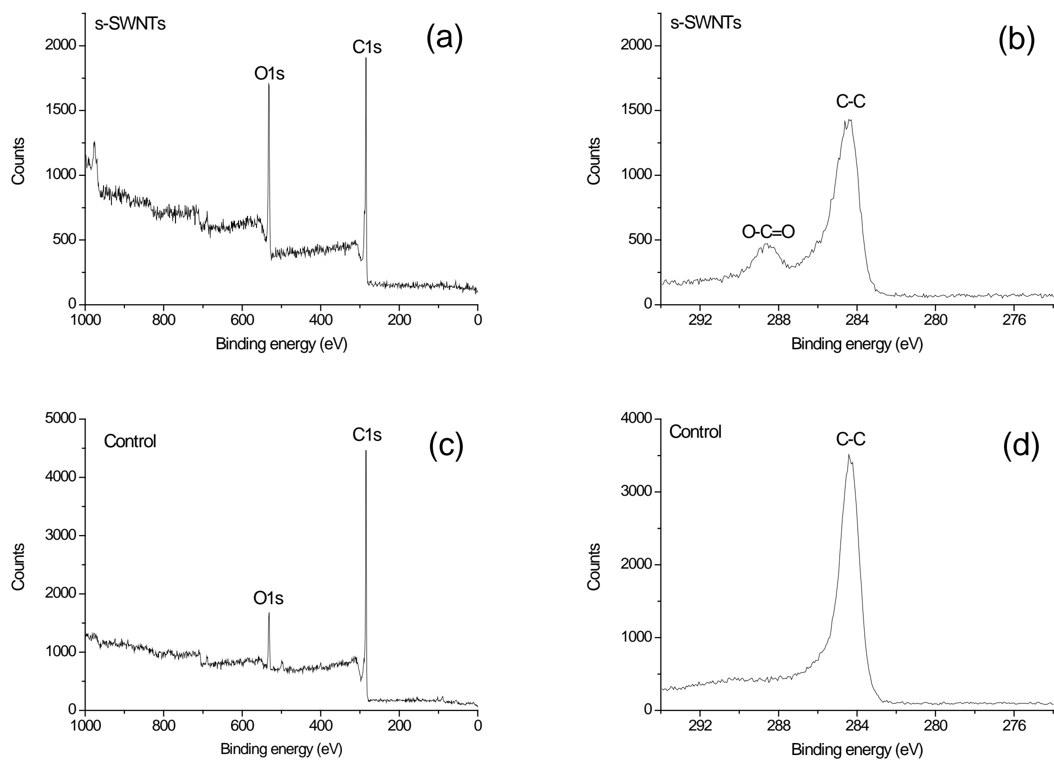

Figure 6.3. XPS survey and carbon 1s narrow scans for an s-SWNTs sample (a and b), and a control sample (c and d). For the control, all reaction conditions were identical to the sample run, with the exception that no peroxide was added.

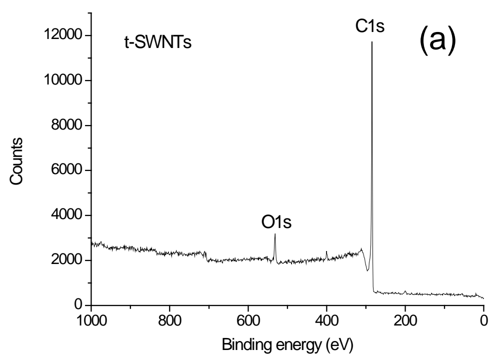

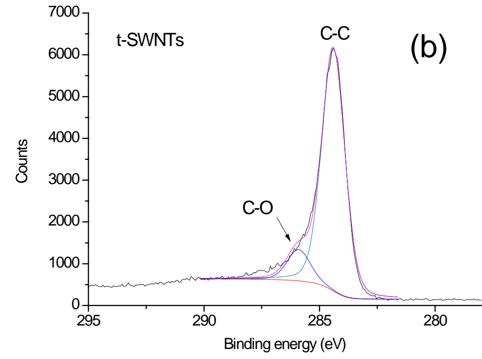

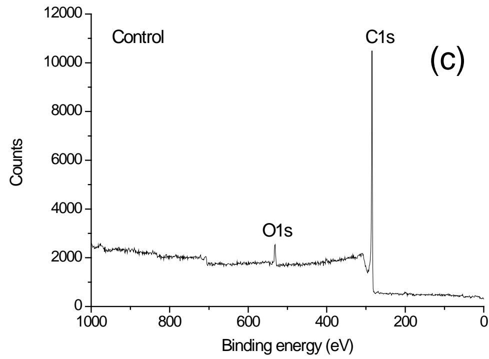

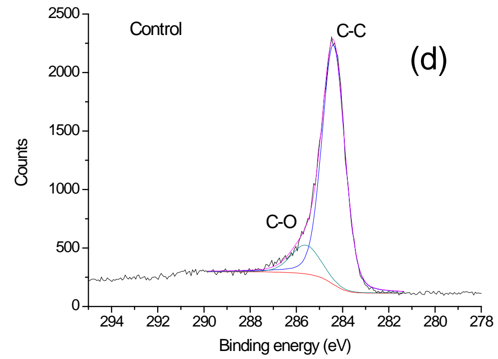

Figure 6.4. XPS survey and carbon 1s narrow scans for a t-SWNTs sample (a and b), and a control sample (c and d).

Table 6.1. Percentages of C, O, and N, and C1s peak components in XPS spectra of t-SWNTs, and control samples.

Area percentage	C1s	O1s	N1s
Di-tert-amyl peroxide/DMF-SWNTs	86.3±1.4%	11.0±0.9%	2.7±0.7%
Control/DMF	93.9±0.3%	5.0±0.1%	1.0±0.3%
Peak Components	**C-C**	**C-O**	
Di-tert-amyl peroxide/DMF-SWNTs	78.4±1.7%	21.6±1.7%	
Control/DMF	85.9±0.5%	14.1±0.5%	

6.6 References

1. Iijima, S., Helical Microtubules of Graphitic Carbon. *Nature* **1991,** *354* (6348), 56-58.

2. Saito, R.; Dresselhaus, G.; Dresselhaus, M. S., *Physical properties of carbon nanotubes*. Imperial College Press: London, 1998.

3. Treacy, M. M. J.; Ebbesen, T. W.; Gibson, J. M., Exceptionally high Young's modulus observed for individual carbon nanotubes. *Nature* **1996,** *381* (6584), 678-680.

4. Liu, C. P. D., *Foundations of MEMS*. Prentice Hall: Upper Saddle River, N.J. ; London, 2006.

5. Qian, D.; Wagner, G. J.; Liu, W. K.; Yu, M.-F.; Ruoff, R. S., Mechanics of carbon nanotubes. *Appl. Mech. Rev.* **2002,** *55* (6), 495-533.

6. Berber, S.; Kwon, Y. K.; Tomanek, D., Unusually high thermal conductivity of carbon nanotubes. *Phys. Rev. Lett.* **2000,** *84* (20), 4613-4616.

7. Collins, P. G.; Avouris, P., Nanotubes for electronics. *Sci Am* **2000,** *283* (6), 62.

8. Guo, T.; Nikolaev, P.; Thess, A.; Colbert, D. T.; Smalley, R. E., Catalytic growth of single-walled manotubes by laser vaporization. *Chem. Phys. Lett.* **1995,** *243* (1-2), 49-54.

9. Joseyacaman, M.; Mikiyoshida, M.; Rendon, L.; Santiesteban, J. G., Catalytic Growth of Carbon Microtubules with Fullerene Structure. *Appl. Phys. Lett.* **1993,** *62* (2), 202-204.

10. Bronikowski, M. J.; Willis, P. A.; Colbert, D. T.; Smith, K. A.; Smalley, R. E., Gas-phase production of carbon single-walled nanotubes from carbon monoxide via the HiPco process: A parametric study. *J. Vac. Sci. Technol. A* **2001,** *19* (4), 1800-1805.

11. Hilding, J.; Grulke, E. A.; Zhang, Z. G.; Lockwood, F., Dispersion of carbon nanotubes in liquids. *J. Dispersion Sci. Technol.* **2003,** *24* (1), 1-41.

12. Astrom, J. A.; Krasheninnikov, A. V.; Nordlund, K., Carbon nanotube mats and fibers with irradiation-improved mechanical characteristics: A theoretical model. *Phys. Rev. Lett.* **2004,** *93* (21), 215503.

13. Berhan, L.; Yi, Y. B.; Sastry, A. M.; Munoz, E.; Selvidge, M.; Baughman, R., Mechanical properties of nanotube sheets: Alterations in joint morphology and achievable moduli in manufacturable materials. *J. Appl. Phys.* **2004,** *95* (8), 4335-4345.

14. Thostenson, E. T.; Ren, Z. F.; Chou, T. W., Advances in the science and technology of carbon nanotubes and their composites: a review. *Compos. Sci. Technol.* **2001,** *61* (13), 1899-1912.

15. Dai, L. M.; Mau, A. W. H., Controlled synthesis and modification of carbon nanotubes and C-60: Carbon nanostructures for advanced polymer composite materials. *Adv. Mater. (Weinheim, Ger.)* **2001,** *13* (12-13), 899.

16. Wunderlich, D.; Hauke, F.; Hirsch, A., Preferred functionalization of metallic and small-diameter single walled carbon nanotubes via reductive alkylation. *J. Mater. Chem.* **2008,** *18* (13), 1493-1497.

17. Lauffer, P.; Jung, A.; Graupner, R.; Hirsch, A.; Ley, L., Functionalization of single-walled carbon nanotubes by aromatic molecules studied by scanning tunneling microscopy. *Phys. Status Solidi B* **2006,** *243* (13), 3213-3216.

18. Holzinger, M.; Abraha, J.; Whelan, P.; Graupner, R.; Ley, L.; Hennrich, F.; Kappes, M.; Hirsch, A., Functionalization of single-walled carbon nanotubes with (R-)oxycarbonyl nitrenes. *J. Am. Chem. Soc.* **2003,** *125* (28), 8566-8580.

19. Hirsch, A., Functionalization of single-walled carbon nanotubes. *Angew. Chem. Int. Edit.* **2002,** *41* (11), 1853-1859.

20. de la Torre, G.; Blau, W.; Torres, T., A survey on the functionalization of single-walled nanotubes. The chemical attachment of phthalocyanine moieties. *Nanotechnology* **2003,** *14* (7), 765-771.

21. Strano, M. S.; Dyke, C. A.; Usrey, M. L.; Barone, P. W.; Allen, M. J.; Shan, H. W.; Kittrell, C.; Hauge, R. H.; Tour, J. M.; Smalley, R. E., Electronic structure control of single-walled carbon nanotube functionalization. *Science* **2003,** *301* (5639), 1519-1522.

22. Dyke, C. A.; Tour, J. M., Unbundled and highly functionalized carbon nanotubes from aqueous reactions. *Nano Lett.* **2003,** *3* (9), 1215-1218.

23. Peng, H. Q.; Alemany, L. B.; Margrave, J. L.; Khabashesku, V. N., Sidewall carboxylic acid functionalization of single-walled carbon nanotubes. *J. Am. Chem. Soc.* **2003,** *125* (49), 15174-15182.

24. Tasis, D.; Tagmatarchis, N.; Bianco, A.; Prato, M., Chemistry of carbon nanotubes. *Chem. Rev. (Washington, DC, U. S.)* **2006,** *106* (3), 1105-1136.

25. Lobach, A. S.; Gasanov, R. G.; Obraztsova, E. D.; Shchegolikhin, A. N.; Sokolov, V. I., Sidewall functionalization of single-walled carbon nanotubes by organometallic chromium-centered free radicals. *Fuller. Nanotub. Car. N.* **2005,** *13* (4), 287-297.

26. Ying, Y. M.; Saini, R. K.; Liang, F.; Sadana, A. K.; Billups, W. E., Functionalization of carbon nanotubes by free radicals. *Org. Lett.* **2003,** *5* (9), 1471-1473.

27. Umek, P.; Seo, J. W.; Hernadi, K.; Mrzel, A.; Pechy, P.; Mihailovic, D. D.; Forro, L., Addition of carbon radicals generated from organic peroxides to single wall carbon nanotubes. *Chem. Mater.* **2003,** *15* (25), 4751-4755.

28. Peng, H. P.; Reverdy, P.; Khabashesku, V. N.; Margrave, J. L., Sidewall functionalization of single-walled carbon nanotubes with organic peroxides. *Chem. Commun. (Cambridge, U. K.)* **2003,** (3), 362-363.

29. Nakamura, T.; Ishihara, M.; Ohana, T.; Tanaka, A.; Koga, Y., Sidewall modification of single-walled carbon nanotubes using photolysis of perfluoroazooctane. *Chem. Commun. (Cambridge, U. K.)* **2004,** (11), 1336-1337.

30. Wu, Z. C.; Chen, Z. H.; Du, X.; Logan, J. M.; Sippel, J.; Nikolou, M.; Kamaras, K.; Reynolds, J. R.; Tanner, D. B.; Hebard, A. F.; Rinzler, A. G., Transparent, conductive carbon nanotube films. *Science* **2004,** *305* (5688), 1273-1276.

31. Borowiak-Palen, E.; Pichler, T.; Liu, X.; Knupfer, M.; Graff, A.; Jost, O.; Pompe, W.; Kalenczuk, R. J.; Fink, J., Reduced diameter distribution of single-wall carbon nanotubes by selective oxidation. *Chem. Phys. Lett.* **2002,** *363* (5-6), 567-572.

32. Chiang, I. W.; Brinson, B. E.; Huang, A. Y.; Willis, P. A.; Bronikowski, M. J.; Margrave, J. L.; Smalley, R. E.; Hauge, R. H., Purification and characterization of single-wall carbon nanotubes (SWNTs) obtained from the gas-phase decomposition of CO (HiPco process). *J. Phys. Chem. B* **2001,** *105* (35), 8297-8301.

Chapter 7 Future work

The work represented in Chapters 2 - 6 of this dissertation has led to promising results obtained through surface modification, fabrication, and characterization. While a variety of future opportunities should stem from these initial studies, more work should be done to improve the processes and materials that were studied; the following is a description of possible future research for each of the projects undertaken in this dissertation.

7.1 Polymer Molded Templates for Nanostructured Amorphous Silicon Photovoltaics

More study is needed to better understand the effects of the diffraction of light with subwavelength gratings so that the pitches and thicknesses of the polymer nanostructures can be optimized to further increase light absorption. Essentially no work was done along these lines in this initial project, and the devices that were made must be considered to be unoptimized. If this project were completed, I would estimate that we could probably gain up to 20% in the efficiency of the devices.

On the materials side, PDMS, which is the current building material for the template, outgasses under vacuum during amorphous silicon deposition, which may degrade the photovoltaic device and reduce the module efficiency. To solve this problem, PDMS must be modified or replaced. Possible ways of improving this material might include removal of unpolymerized oligomers, surface oxidization (most likely with an oxygen plasma), or deposition of a layer over the PDMS template. Alternatively, a different material could be sought as a replacement for PDMS that would have greater vacuum compatibility. One possibility along these lines is a transparent polyimide.

In the fabrication of the devices, the silicon deep etching profile should be further investigated to produce less vertical (tapered) nanostructures on the silicon master. By so doing,

the defects on the embossed polymer would be reduced during the demolding process. In addition, e-beam lithography is a time consuming technique for making large patterns, i.e., it can often be used with great effectiveness to make prototypes, but it is usually not economically viable as a processing tool. Other patterning techniques, such as interference lithography, should be investigated for quick and inexpensive pattern generation.

Ideally, all of these directions would be investigated and integrated into the solar cell device project to achieve devices with higher efficiency and greater economic viability. Indeed, there may be a synergy between these possibilities. That is, the gains from completing two or more of these directions might be greater than the sum of the individual gains for these new directions.

7.2 Processing of Thin, Composite Carbon Nanotube-Polyimide Composite Membranes

Although a successful process was developed, the uniformity of the resulting carbon nanotube films could still be improved. Indeed, at this current stage, the nanotube films are still rough because the manual rolling force appears to be uneven and leads to tearing in the films. Thus, the rolling process should be modified using mechanically controllable machines or alternative thin film deposition methods. Moreover, the fabrication process should be further investigated with various thicknesses of polymer layers by adjusting polymer spin rates, carbon nanotube film thicknesses, and other parameters (nanotube growth conditions, rolling, spin times, etc.), so that the final membrane thickness can be easily tuned for desired applications. Finally, a mechanical test measurement should be designed and then performed on these reinforced composite membranes.

7.3 Time-of-Flight Secondary Ion Mass Spectrometry of a Range of Coal Samples: A Chemometrics (PCA, Cluster, and PLS) Analysis

The ToF-SIMS analysis of coal samples[1] focused mostly on the inorganic species present in the materials as well as a variety of small organic fragments created by the primary ion beam. The surface compositions of these coal samples could be further studied by ToF-SIMS analysis with other primary ion beam sources and energies. For example, polyatomic primary ion beams may generate a higher proportion of highly characteristic high mass fragments. Moreover, the G-SIMS[2-3] technique might be used to obtain more fragmentation information as it uses several spectra taken of the sample under different primary ion beam conditions to extrapolate back to the original species present at a surface. The possible speciation of the material that could be generated in this way might be very important.

7.4 Laser Activation-Modification of Semiconductor Surfaces (LAMSS) of 1-Alkenes on Silicon: A ToF-SIMS, Chemometrics, and AFM Analysis

For the laser activation-modification of semiconductor surfaces (LAMSS),[4-5] the theory of the laser activation process is little understood, especially in the context of a reactive liquid over the surface of a material and the resulting chemistry that is driven by the laser. This process might be simulated to generate ablation profiles and to predict chemical functionalization. Also, a further exploration of the possibility of LAMSS as a quick, convenient, and green chemistry for synthesizing organically functionalized silicon nanocrystals via a one-step reaction should be studied, with a possible eye towards scaling up the process for mass production[6].

References

1. Pei, L.; Jiang, G.; Tyler, B. J.; Baxter, L. L.; Linford, M. R., Time-of-flight secondary ion mass spectrometry of a range of coal samples: A chemometrics (PCA, cluster, and PLS) analysis. *Energ. Fuels* **2008,** *22* (2), 1059-1072.

2. Gilmore, I. S.; Seah, M. P., Static SIMS: towards unfragmented mass spectra - the G-SIMS procedure. *Appl. Surf. Sci.* **2000,** *161* (3-4), 465-480.

3. Gilmore, I. S.; Seah, M. P., G-SIMS of crystallisable organics. *Appl. Surf. Sci.* **2003,** *203*, 551-555.

4. Pei, L.; Jiang, G. L.; Davis, R. C.; Shaver, J. M.; Smentkowski, V. S.; Asplund, M. C.; Linford, M. R., Laser activation-modification of semiconductor surfaces (LAMSS) of 1-alkenes on silicon: A ToF-SIMS, chemometrics, and AFM analysis. *Appl. Surf. Sci.* **2007,** *253* (12), 5375-5386.

5. Zhang, F.; Pei, L.; Bennion, E.; Jiang, G. L.; Connley, D.; Yang, L.; Lee, M. V.; Davis, R. C.; Smentkowski, V. S.; Strossman, G.; Linford, M. R.; Asplund, M. C., Laser activation modification of semiconductor surfaces (LAMSS). *Langmuir* **2006,** *22* (26), 10859-10863.

6. Shirahata, N.; Linford, M. R.; Furumi, S.; Pei, L.; Sakka, Y.; Gates, R. J.; Asplund, M. C., Laser-derived one-pot synthesis of silicon nanocrystals terminated with organic monolayers. *Chem. Commun. (Cambridge, U. K.)* **2009,** (31), 4684-4686.

Appendix 1 Angled Thermal Evaporation

In my research, several materials, including Fe, Al, LiF, and NaCl, were deposited by thermal evaporation. In the case of aluminum deposition on a nano-patterned substrate, an angled thermal evaporation setup was designed to prevent aluminum from covering the entire surface. Accordingly, the sample was mounted on a holder with a rotor as shown in Figure A1.1. Since the deposition angle was around 70°, most of the aluminum only deposited on top of the surface, and not in the nano-trenches. Rotation during deposition was used to ensure the uniformity of the film. In this way, a 30 nm aluminum film was deposited on our patterned substrate.

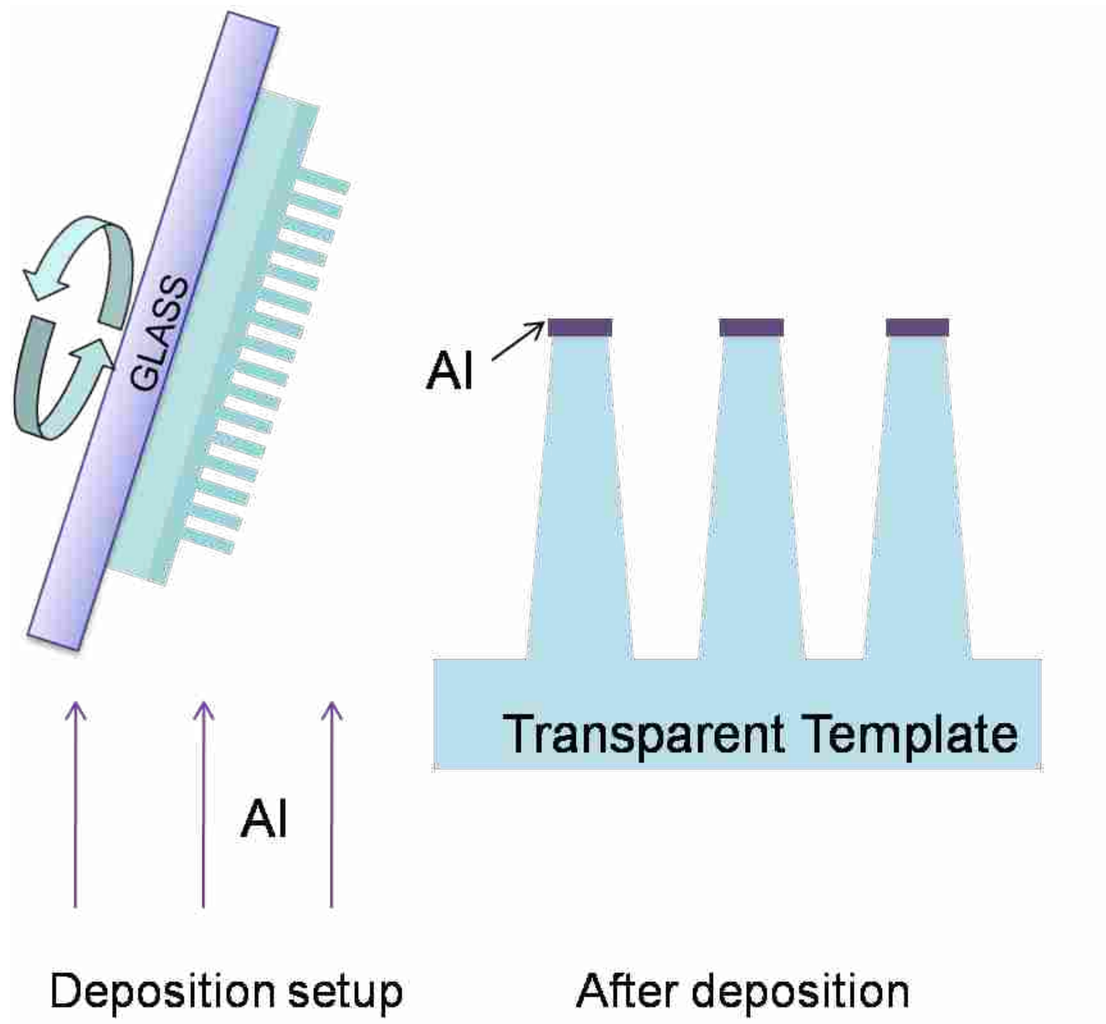

Figure A1.1. Angled thermal evaporation setup for aluminum deposition on a patterned substrate.

Appendix 2 NIL Processes on PI, PEN, and PDMS

In my research, NIL was used to pattern a polymer layer using a pre-fabricated silicon master as a hard mold. After embossing, the polymer layer became a template for solar cell fabrication. However, there are several requirements for the polymer material as a solar cell template. These are (1) low cost; (2) optical transparence; (3) thermal stablility up to 200 - 250 ˚C, which is required in the silicon *p-i-n* layer deposition; and (4) vacuum compatibility. I tested several polymer materials for our nanoimprint lithography process, including polyimide (PI), polyethylene naphthalate (PEN), and polydimethylsiloxane (PDMS).

The advantages of polyimide as the template building material are that PI is quite thermally stable even up to 400°C, vacuum compatible, and inexpensive. Thus, PI was used in the initial tests of the NIL process. In an early step of this procedure, the patterned master was coated by CVD with a layer of a perfluorosilane as an anti-adhesion film. The advancing water contact angle of the master then increased to 105°. The target silicon substrate was also coated by CVD with a silane: 3-aminopropyltriethoxysilane (APTES) as an adhesion promotion layer. (Note that glass, and not silicon, would be used in production.) The substrate was then spin coated with a layer of polyimide (PI 2545) at 1000 rpm for 1.5 min and soft baked at 100 °C for 5 min and 120 °C for 1 min. In this way, the polyimide layer can chemically bond with the amine groups on the substrate, but not stick to the master wafer. The assembly (a master wafer, polyimide film and a target substrate) were placed together in a CARVER hydraulic press. Glass slides and filter paper sheets were used as a buffer to stabilize the substrate and distribute the applied forces. A pressure of approximately 800 psi was applied and the temperature was raised to 200°C, which was held for 2 min, after which the sandwich structure was cooled to room temperature. The substrate was finally separated from the master with a razor blade. The

imprinted pattern profile is shown in Figure A2.1 I note that there are some issues regarding PI in the NIL process: (1) PI is colored, so a PI template absorbs some light energy before it reaches the photovoltaic (PV) layer, which reduces the solar cell efficiency; and (2) PI requires a high temperature cure, which may cause pattern defects or deformation and silicon master breakage due to thermal expansion mismatch effects.

A different material, polyethylene naphthalate (PEN), was also tested for the solar cell template, as PEN is optically transparent, vacuum compatible, and free-standing – it does not require a flat supporting substrate. Furthermore, an amorphous silicon *p*-*i*-*n* layer deposition process on flat PEN film has been developed. Since PEN was obtained as a thermoplastic sheet, thermal NIL (hot embossing) was applied to pattern the PEN material in the following way. A silicon master was pressed into a PEN film while PEN was heated above its glass transition temperature of 170 ˚C. The heated PEN material then became viscous and flowed around the features of the silicon master under the high pressure. The PEN was then cooled, and the master was removed to leave the reversed pattern in the PEN film. However, owing to the difference in thermal expansion coefficients of PEN and silicon, it was a challenge to obtain a smooth, clean PEN surface with high aspect ratio nanostructures after the embossing process. Typically, the top edges of the nanostructures were distorted during the demolding process and yielded undesirable (bumpy) defects, as shown in Figure A2.2.

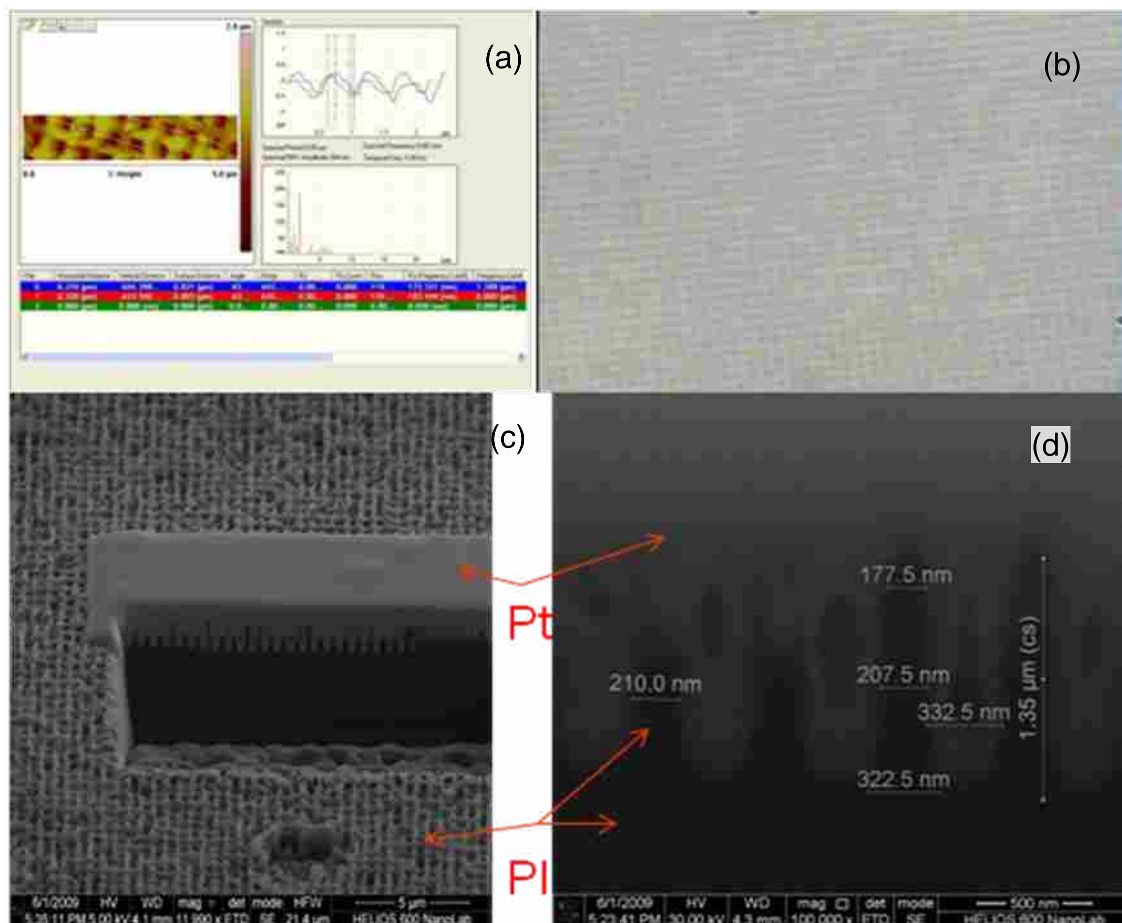

Figure A2.1. (a) AFM image of a polyimide film patterned via NIL, (b) optical image of the NIL patterned polyimide film, and (c and d) SEM cross-sectional images of an NIL patterned polyimide film. The cross-sectional feature was milled by FIB and had a Pt coating.

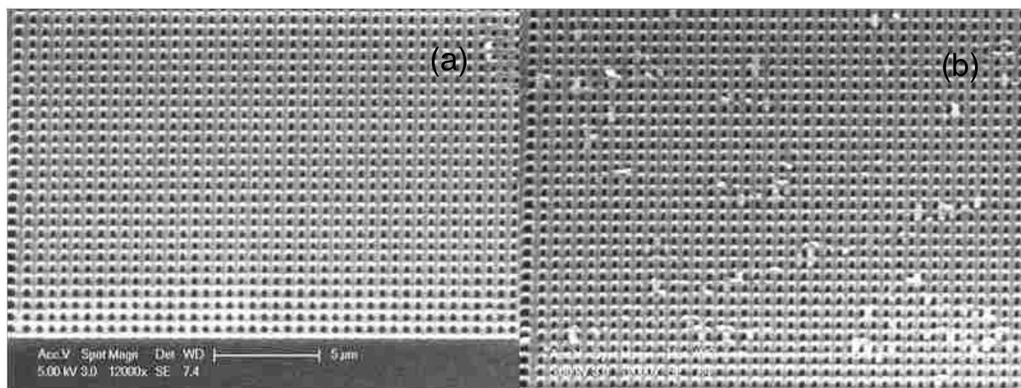

Figure A2.2. SEM image of a PEN template embossed with nanostructures. Note that a small bump appears on the top edge of each nanohole (a), and undesired contamination appears on the surface (b).

PDMS has also been used to build solar cell templates, since PDMS is optically transparent, inexpensive, established as a material for nanoimprinting, and subject to less thermal expansion stress due to its curing process at low temperature. A commercially available material PDMS Sylgard 184, was used for an initial study. Thus, to do the nanoimprinting, non-crosslinked PDMS was mixed with a crosslinking agent and degassed for 30 minutes in a desiccator. The mixture was then poured or spin cast onto a silicon master. The assembly was degassed again to remove the air bubbles inside the high aspect ratio nanopatterns, covered with a glass slide and weight to reduce the thickness of the PDMS layer, and cured at room temperature for 12 hours, and then at 80 ˚C for 1 hour. However, this initial test on the Sylgard 184 PDMS was not successful. The patterned polymer recessed and lost its sharp features, due to its low material strength. We then used the approach of Whitesides and coworkers'[1], and employed hard PDMS (h-PDMS) in our NIL, where the modulus of h-PDMS is 4.5 times higher than that of Sylgard 184. In this way, a clean, transparent polymer template was finally fabricated with well patterned, high aspect ratio nanostructures.

Appendix 3 Plasma Etching

After e-beam lithography is used to pattern a resist, samples were developed to dissolve the exposed resist. However, even after thorough rinsing with water, there were still residues of resist left on exposed areas. PE2 oxygen plasma treatment was applied to remove this residual material (100 W for 1 min); this is called a descum process. Otherwise, any residual material would partially protect the underlying silicon as an unwanted mask layer during deep silicon etching processes (until the residues were fully etched away by reactive ions). This will result in different effective starting times for the silicon etch, yielding a rough surface.

Although the silicon deep etching process etches both silicon and unexposed polymer resists, the etching rate of the resist is lower than the etching rate of silicon. After silicon deep etching, a thick resist layer still remains on the surface. The PE2 plasma was used to remove most of this resist layer (at 200 W for 2 min). The sample was then treated in piranha solution for an additional thorough clean, which also added hydroxyl groups to the silicon surface.

A plasma was also used for surface modification to improve adhesion. To deposit an electrode of a solar cell device, a 30 nm thick aluminum layer was thermally deposited on a PDMS template, and also on a glass slide as a control. However, while electrical sheet resistance measurements showed that the aluminum coated glass slide had the expected high conductivity, the aluminum-coated PDMS template was not conductive. This difference (and SEM imaging) suggested that the aluminum atoms did not wet the PDMS surface and formed an incomplete layer. This may be because the PDMS is non-polar (it has a water contact angle of 85°). To increase the PDMS surface energy, the PDMS template was treated with an air plasma in the Harrick plasma instrument for 2 min, which oxidized the PDMS surface and introduced

hydroxyl and Si-O-Si groups onto the surface.[2] This treatment reduced the water contact angle of the surface to less than 10°. With improved adhesion, the resulting aluminum coated PDMS surface was as conductive as the aluminum coated glass control. However, the PDMS polymer also has mobile oligomers present in it. These short chain oligomers, which only have a few monomer units, may migrate towards the surface and make the material hydrophobic again. Because of this effect, aluminum should be deposited within an hour after the air plasma treatment.

References

1. Odom, T. W.; Love, J. C.; Wolfe, D. B.; Paul, K. E.; Whitesides, G. M., Improved pattern transfer in soft lithography using composite stamps. *Langmuir* **2002,** *18* (13), 5314-5320.

2. Yang, L.; Shirahata, N.; Saini, G.; Zhang, F.; Pei, L.; Asplund, M. C.; Kurth, D. G.; Ariga, K.; Sautter, K.; Nakanishi, T.; Smentkowski, V.; Linford, M. R., Effect of Surface Free Energy on PDMS Transfer in Microcontact Printing and Its Application to ToF-SIMS to Probe Surface Energies. *Langmuir* **2009,** *25* (10), 5674-5683.